UNIVERSITÀ POLITECNICA DELLE MARCHE

Scuola di Dottorato di Ricerca della Facoltà di Medicina e Chirurgia

Curriculum "Human Health"
XXXVI ciclo

NEW INSIGHTS ON MESENCHYMAL STEM CELLS DYSFUNCTIONS IN COMPLICATIONS OF CUSHING SYNDROME

Relatore Chiar.mo

Prof.ssa Monia Orciani

Tesi di dottorato di:

Dott.ssa Mariangela Di Vincenzo

Correlatore Chiar.mo

Prof. Giorgio Arnaldi

Coordinatore Chiar.mo

Prof. Mario Guerrieri

Anno Accademico 2022/2023

ABSTRACT

Chronic glucocorticoids (GCs) excess and disrupted circadian rhythm lead to Cushing's Syndrome (CS), a severe clinical condition delineated by insulin resistance (IR), dyslipidaemia, cardiovascular disease, osteoporosis and impaired immune system. Mesenchymal stem cells (MSCs) are multipotent cells, able to differentiate into adipocytes, chondrocytes, and osteoblasts, and in recent years, it has been demonstrated their involvement in the onset and development of different pathologies. As undifferentiated progenitors of adipocytes and osteoblasts, MSCs may display the detrimental effects of GCs excess and they could be involved in IR and osteoporosis issues. In this line, the involvement of MSCs in CS was studied in three different and independent tasks, in which the mechanisms underlying these comorbidities were investigated. MSCs were isolated from the skin of healthy control subjects (C-MSCs) and of patients affected by Cushing Syndrome, both exogenous (EXO-MSCs) and endogenous (ENDO-MSCs) CS and used to evaluate their role in the onset of CS comorbidities.

In addition, MSCs were isolated from patients affected by exogenous CS but treated with steroid sparing (EXO-SS-MSCs).

The results showed that MSCs could be a prominent new model to study IR. In the TASK1, the exposure of C-MSCs to constantly high concentrations of GCs significantly decreased glucose uptake by blocking GLUT-4 translocation and improved lipolysis when the exposure to GCs was prolonged. Furthermore, in TASK3 mitochondrial dysfunctions were detected in MSCs isolated from Cushing patients. These data displayed that the excessive fragmented mitochondrial network destroyed the mitochondrial membrane potential, increased ROS levels and decreased ATP production, promoting the hypothesis that impaired mitochondrial metabolism could also contribute to the development of IR.

The outcomes of TASK2 demonstrated the involvement of MSCs in osteoporosis. MSCs isolated from Cushing patients showed a reduced capacity to differentiate into osteoblasts, with concomitant decreased ALP activity, poor matrix mineralization, and a tardive expression of genes related to osteoblastogenesis. Despite their poor differentiation capacity, the ratio RANK-L/OPG was higher in EXO-CS-MSCs, resulting in enhanced bone resorption by promoting differentiation and maturation of PBMCs into osteoclasts. On the contrary, the long-term effects of GCs in patients with endogenous CS resulted in depressed osteoclast activity.

Moreover, the results of TASK2 and 3 confirmed the ability of steroid sparing treatments in reducing the effects of GCs long-term therapy also at stem level: osteoblastogenesis and mitochondrial functions of EXO-SS-MSCs were closer to those observed in C-MSCs than EXO-MSCs.

In conclusion, this thesis highlights the impact of GCs excess on MSCs, that represent a new cellular model to study CS. The involvement of MSCs in IR, osteoporosis and potentially other related Cushing's comorbidities sets the stage for new studies aimed to understand the specific mechanisms that driving these issues, and it could be a new starting point for more specific and targeted therapy.

INDEX

1. INTRODUCTION

1.1. Mesenchymal stem cells (MSCs)

In recent years, stem cell research has gained the upper hand and numerous studies have described their classification, their behavior and their use in therapeutic approaches. Stem cells are unspecialized cells, able to differentiate into different cell lines and to self-renew[1]. Stem cells are located in both embryo and adult organisms with different steps of specializations:

- **Totipotent stem cells** have the highest differentiation potential and can divide and differentiate into cells of the whole organism. Zygote is one example of a totipotent cell.
- **Pluripotent stem cells** are able to differentiate into any of the three germ layers: ectoderm, mesoderm and endoderm. These cells can not give rise to an adult organism, because they do not have the potential to contribute to extra-embryonic tissues.
- **Multipotent stem cells** can differentiate into a limited number of cell lineages. An example of a multipotent stem cell is the hematopoietic cell which can develop into several types of blood cells.
- **Oligopotent stem cells** have the ability to differentiate into only certain types of cells, such as vascular stem cells that can give rise to either smooth muscle or endothelial cells.
- **Unipotent stem cells** differentiate into a single cell type. Hepatocytes, for example, are unipotent. The ability of the liver to regenerate from a minimum of 25% of its original mass is attributed to this property; other examples are given by unipotent cubic or cylindrical stem cells present at the level of the germinal layer of the epidermis.

Given the ethical problems associated with the use of embryonic stem cells, research has focused on the study of adult stem cells. These are multipotent

stem cells and allow the healing and the growth of the tissues. Among many types, mesenchymal stem cells (MSCs) are a great interest of study [2].

1.1.1. Classification of MSCs

"Mesenchymal stem cells" is a term coined by Arnold I. Caplan in 1991 to indicate cells derived from mesenchyme, an embryonic connective tissue [3]. Morphologically they are long and thin and present a small cell body with a large nucleus and an evident nucleolus [4]. The International Society for Cellular Therapy (ISCT) defines MSCs as a heterogeneous population of cells characterized by plastic adherence, fibroblast-like morphology, differentiation capability into mesodermal cell types, including osteoblasts (bone cells), chondrocytes (cartilage cells), and adipocytes (fat cells). Cultured MSCs also express on their surface CD73, CD90 and CD105, while they lack the expression of CD11b, CD14, CD19, CD34, CD45, CD79a and HLA-DR surface markers [5].

MSCs have been extensively studied over the past 30 years for their interesting cell biology and their clinical potential, including tissue repair, regenerative medicine, and cell-based therapies for various diseases [2].

1.1.2. Differentiation capability

MSCs were isolated for the first time from bone marrow as adherent cells able to differentiate into osteoblasts [6]. Today, MSCs can be isolated from different tissues such as adipose tissue, umbilical cord, peripheral blood, placental tissue, synovial fluid, skin and dental pulp. Their great differentiation potential and the ease collection get MSCs valuable sources for possible clinical applications in regenerative medicine [7]. In fact, their ability to differentiate into osteocytes and chondrocytes makes them promising candidates in bone regenerative therapy. Different studies sustain that exogenous MSCs can play a modulatory role in fracture healing by recruiting other cell types and increasing vascularization and modulating

immunological responses [8]. Furthermore, it has been reported that MSCs display the capacity of trans-differentiation. For example, they could be used in diabetic therapy as it has been proved their capacity to differentiate into endocrine pancreatic cells able to secrete glucagon and insulin [9]. Sasaki et al. also demonstrated that MSCs are involved in wound repair because of their ability to differentiate into skin cells [10]. Recent studies showed the ability of MSCs to differentiate into neuron-like cells [11,12], but doubts remain about their functionality [13]. The clinical use of MSCs is not merely dependent on their differentiation capacity, but the secretion of cytokines, chemokines and growth factors emphasize their therapeutic potential.

1.1.3. Immunomodulatory effects of MSCs

Over the past decade, attention has shifted towards the ability of MSCs to produce factors and cytokines that stimulate innate tissue repair, modulate inflammation and suppress tumour growth [14]. MSCs secrete many immunomodulatory factors, such as Interleukin-6 (IL-6), Nitric oxide (NO), Indoleamine 2,3-dioxygenase (IDO), Prostaglandin E2 (PGE2) [15,16]. Although the mechanisms must be still clarified, MSCs exert immunomodulatory functions through interaction with immune cells such as lymphocytes, macrophages, monocytes, dendritic cells (DCs) and neutrophils. The interaction can occur through either cell-cell contact or through the paracrine action of MSCs. To assist anti-inflammatory effects, MSCs can migrate to the site of injury and polarize macrophages in M2 phenotype by PGE2 activity [17]. PGE2 also inhibits the production of Tumor necrosis factor alpha (TNF-α) by mast cells and the cytotoxic activity of natural killer lymphocytes [18]. The secretion of IL-6 and IL-8 suppresses the apoptosis of neutrophils and inhibits the activity of DCs [19]. Furthermore, MSCs can reduce T and B cells proliferation trough the inhibition of cell cycle between G0 and G1 phases [20,21].

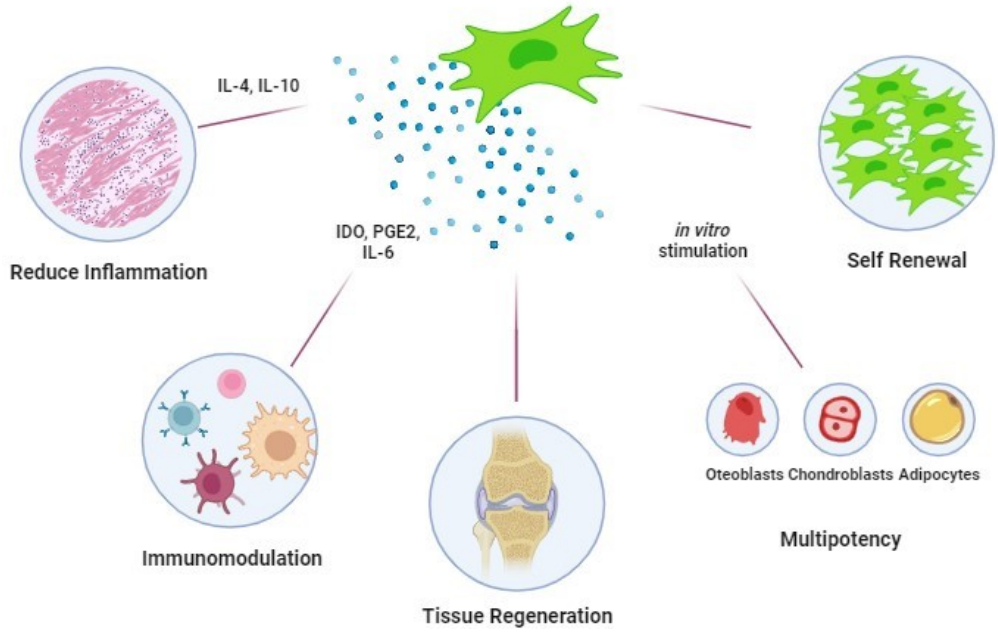

Figure 1. Immunomodulation and multipotency properties of MSCs. MSCs are able to modulate the immune systems and to reduce inflammation by secreting different factors. Further, MSCs can be used in regenerative medicine for tissue repair because of their capability to differentiate in bone, cartilage, and adipose cells.

1.1.4. MSCs & disease

Despite their role in immunomodulation, MSCs may also be involved in the onset of some pathologies. In the past years our research group demonstrated that MSCs display an altered immune profile in different diseases such as psoriasis, atopic dermatitis, leiomyoma, idiopathic pulmonary fibrosis (IPF), and Cushing's syndrome. In psoriasis and atopic dermatitis, MSCs isolated from skin biopsies of patients showed an imbalance of Type 2 vs Type 1/Type 17 T helper cells (Th2 vs Th1/Th17) profile related to the pathogenesis [22–24]. In lung disease, MSCs also present altered secretory and immunomodulatory properties that can contribute to the onset of the disease. Specifically, in IPF, different factors, such as TNF-α and Transforming growth factor β -1 proprotein (TGF-β1) promote the

differentiation of MSCs in myofibroblasts, that are responsible of fibrotic aspects of IPF [25,26]. MSCs may also support the chronic inflammation in leiomyoma. A profiling miRNAs analysis conducted on MSCs isolated from myometrium of patients with leiomyoma showed that out of more than 2000 miRNAs only 15 miRNAs were dysregulated, all involved in pathways related to uterine fibrosis [27]. To date, the study of MSCs in pathogenetic processes is still little known and requires numerous clarifications. At the same time, however, these data confirm that MSCs could be a much more efficient therapeutic target, as they themselves could primarily drive towards an inflamed and stressed microenvironment, compromising the differentiated cells functions.

1.2. Cushing's Syndrome

Cushing's syndrome (CS) is a complex disease caused by a prolonged exposure to glucocorticoids (GCs) as well as cortisol, a steroid hormone produced mainly by the *zona fasciculata* located into the adrenal gland cortex [28].

1.2.1. Cortisol

1.2.1.1. Biosynthesis

The secretion of cortisol is under the control of hypothalamus, a part of brain responsible for linking the nervous system to endocrine system via pituitary gland. The hypothalamus releases Corticotropin-releasing hormone (CRH), a peptide hormone, which stimulates pituitary gland to produce and secrete Adrenocorticotropic hormone (ACTH) into the blood. ACTH reaches adrenal glands and induces the synthesis of cortisol and other glucocorticoids as well as Mineralocorticoid aldosterone, and Dehydroepiandrosterone [28]. More precisely, ACTH increases the levels of cholesterol in the inner membrane of mitochondria and induces its conversion into pregnenolone, a precursor of cortisol [29]. Cortisol follows a circadian rhythm that is regulated by the

master circadian oscillator (pacemaker) in the suprachiasmatic nucleus (SCN), located in the hypothalamus. Generally, normal individuals present very low levels of cortisol in the evening (lower limit 30nmol/L), that build up overnight and peak in the morning (upper limit 500nmol/L), followed by a slowly decline throughout the day [30].

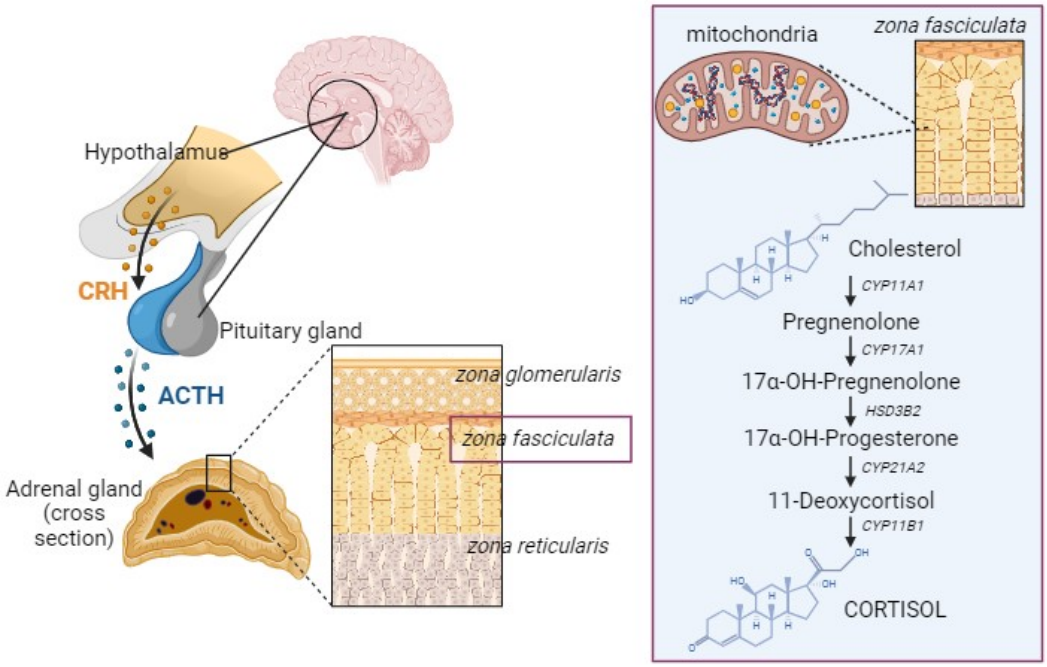

Figure 2. Cortisol biosynthesis. ACTH stimulates steroid cells of *zona fasciculata* of the adrenal glands to produce cortisol. In mitochondrial inner membrane of steroid cells, cholesterol is converted to cortisol via regulation of the steroidogenic regulatory proteins.

1.2.1.2. Immune response

GCs are involved in immune response as immunosuppressors. In stress conditions, immune cells secrete IL-1, IL-6 and TNF-α, which stimulate the hypothalamus to secrete CRH, that in turn promotes the production of cortisol by adrenal glands. Cortisol inhibits the production of IL-12, Interferon gamma (IFN-γ) and TNF-α by antigen-presenting cells (APCs) and T helper cells (Th1 cells). GCs also downregulate IL-2 receptor (IL-2R)

on the surface of T-cells, that is crucial to induce a Th1 cellular immune response. This inactivation improves a shift towards Th2 dominance and the secretion of IL-4, IL-10, and IL-13 by Th2 cells, resulting in a general immunosuppression and it favours a B-cell mediated antibody immune response [31]. Through this process cortisol regulates the immune response to prevent an over-activation of inflammation.

1.2.1.3. Metabolism

Cortisol is released in response to stress, but at the same time it plays a key role in the metabolism of glucose, proteins and lipids. Cortisol is also involved in bone formation and immune response [28,32]. GCs enter the cells and they are activated by the 11β-hydroxysteroid dehydrogenase type 1 (11β-HSD1) or deactivated by 11β-HSD2. Activated GCs bind the Glucocorticoid receptor (GR), that is located into the cytoplasm, and it is associated with Heat shock protein 90 (HSP90) chaperone complex. After binding to cortisol, GR dissociates from HSP90 and enters the nucleus, where the GR is recruited to specific genomic sequences, called glucocorticoid response elements (GREs). The GR:GRE association triggers a number of transcriptional factors able to modulate the transcription of genes involved in different process [33].

Glucose metabolism

GCs regulate different aspects of glucose homeostasis by promoting gluconeogenesis and glycogenesis in the liver, inhibits glyceroneogenesis in adipocytes, and reduce glucose uptake in skeletal muscle and white adipose tissue (WAT) resulting in an increase of glucose concentration into the blood [34–37]. On the other hand, insulin, a hormone secreted by pancreatic β cells, exerts opposite functions on these physiological processes by inhibiting gluconeogenesis and promoting glucose utilization in skeletal muscle and WAT.

Cortisol stimulates the production of glucose mainly through the transcription of genes involved in the gluconeogenesis pathway: Pyruvate carboxylase (PC), Phosphoenolpyruvate carboxykinase, cytosolic (PEPCK-C), Fructose-1,6-bisphosphatase 1 (FBP1), 6-phosphofructo-2-kinase/fructose-2,6-bisphosphatase 1 (PFKFB1), Glucose-6-phosphatase catalytic subunit 1 (G6PC) and G6P transporter.

On the other hand, cortisol inhibits the glucose uptake in skeletal muscle and WAT by counteracting the effects of insulin. GCs, in fact, inhibits the translocation of Solute carrier family 2, facilitated glucose transporter member 4 (GLUT-4) to the cell membrane. Cortisol also decreases the tyrosine 608 phosphorylation of Insulin receptor (IR) and the expression of insulin receptor substrate protein family (*IRS1*). At the same time, in the liver, GCs increase the gene expression of enzymes involved in ceramide synthesis, that interfere with insulin signalling [33].

In liver and muscle, cortisol also activates glycogen phosphorylase to divide glycogen into glucose-1-phosphate and glucose in glycogenolysis process [38].

As its role in these opposite processes, a physiological concentration of GCs is crucial for a correct glucose turnover.

Lipid metabolism

During fasting, the free fatty acids (FFA) obtained from the hydrolysis of triglycerides (TG) are released by adipocytes and carried to the liver, where they are reconverted into TG; therefore, returning to the adipocytes as FFA, by hydrolysis of a lipoprotein lipase (LPL), they can be converted back into TG and reaccumulated. This mechanism is known as triacylglycerol cycle, and it is crucial to maintain a constant concentration of FFA in the blood to have source of energy immediately usable in case of emergency. The triacylglycerol cycle is controlled by GCs by regulating PEPCK, that

converts oxaloacetate into phosphoenolpyruvate, a fundamental step into TG synthesis in the liver. On the other hand, GCs suppress TG synthesis in the adipose tissue, increasing FFA concentration in the blood [39]. It has been demonstrated that GCs stimulate the transcription of genes involved in lipolysis pathway such as Hormone-sensitive lipase (LIPE), (Lipoprotein lipase) LPL and Patatin-like phospholipase domain-containing protein 2 (PNPLA2, known also as ATGL), which divide TG into FA and glycerol [40]. At the same time, GCs are involved in the synthesis of fatty acids. In particular, GCs promote the transcription of Acetyl-CoA Carboxylase 1 and 2 (ACC-α and ACC-β), enzymes that regulate the FA synthesis [41].

Bone homeostasis

Bone homeostasis is the result of a cross-talk between osteoblasts, responsible for bone matrix deposition, and osteoclasts, assigned to bone resorption. GCs can regulate the bone homeostasis in a cell-type specific manner. In fact, different studies proved that GCs in osteoblasts are necessary to maintain the bone mass. The inactivation of GCs in osteoblasts and osteocytes reduces cortical and trabecular bone mass. Furthermore, a GR deficiency inhibits early osteoblasts progenitor markers (Runt-related transcription factor 2 (RUNX2) and Transcription factor Sp7, (OSX1)) and causes a decreased bone mass. In contrast, osteoclasts are not affected by GCs in physiological conditions [42].

1.2.2. Cushing's Syndrome: causes & comorbidities.

The most common causes of CS are related to the prolonged use of GCs in the treatments of other disease (exogenous CS), such as asthma and rheumatoid arthritis, to induce immunosuppression. Although more rarely, high cortisol levels may be due to its overproduction by the adrenal glands (endogenous CS), following the appearance of tumours in the pituitary or adrenal glands. Both exogenous and endogenous CS lead to a collection of

symptoms, as well as a round red face, abdominal obesity and thin arms and legs, high blood pressure, weak muscles, weak bones, acne, fragile skin that

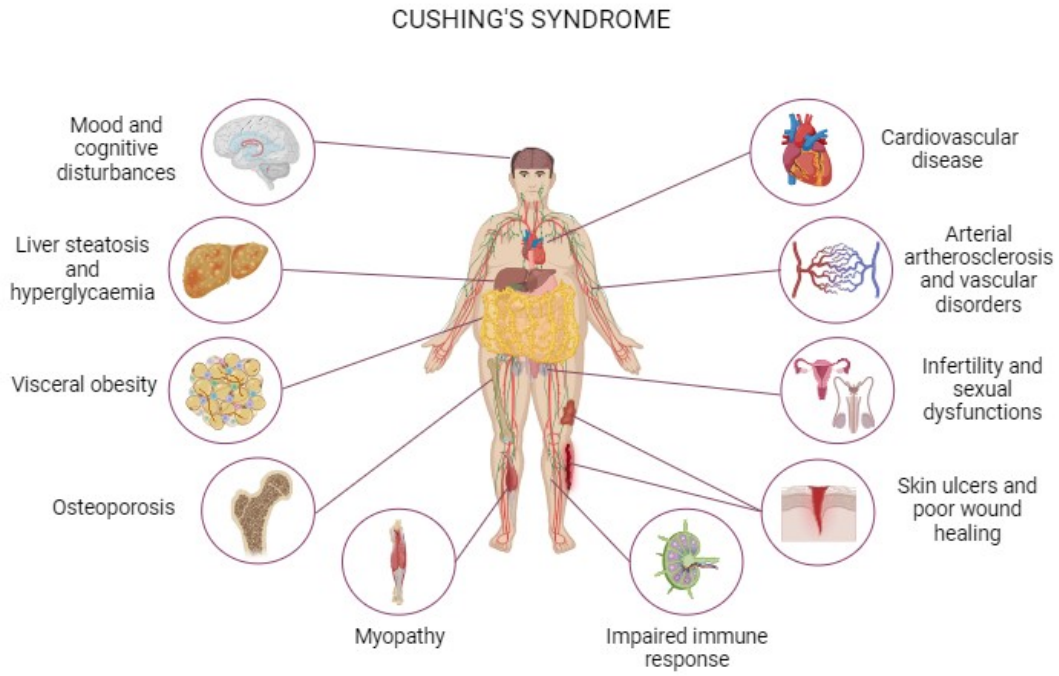

heals poorly, irregular menstruations and infertility, hirsutism, mood changes and headaches. CS's symptoms are related to metabolic syndromes: insulin resistance (IR), obesity, hypertension, elevated levels of triglycerides and osteoporosis [43].

Figure 3. Cushing's syndrome comorbidities. Chronically elevated concentrations of GCs lead to complications of the clinical picture of CS. Patients manifest cognitive impairment, hepatic steatosis, hyperglycaemia, cardiovascular disorders, osteoporosis, myopathy, infertility, altered immune response, and poor wound healing.

1.2.2.1. IR & lipolysis

In CS the metabolism of glucose is impaired, resulting in diabetes mellitus (Type 2) and cardiovascular disorders. Type 2 diabetes is linked to IR which can be supported by a reduced insulin secretion. The excess of GCs leads to the development of IR in the body, especially in skeletal muscle and WAT.

The development of IR in CS is related to multiple mechanisms of action of GCs in different tissues. These can be summed in:

- Reduced glucose uptake in WAT and skeletal muscle
- Increased gluconeogenesis
- Reduced insulin secretion by pancreatic β cells

Adipose tissue is specialized in the storage of fatty acids. The adipose tissue is involved in glucose homeostasis through lipogenesis, *de novo* fatty acid synthesis from glucose, allowing fat storage as TAG. Elevate concentrations of fats stored into WAT are observed in lipodystrophies, obesity, or IR and it leads to the ectopic accumulation of fat in other tissues such as skeletal muscle, liver and pancreas [44]. Long-term exposure to GCs causes a lipodystrophy characterized by an increase of visceral adipose tissue (VAT) and a decrease of the sub-cutaneous adipose tissue (SCAT) [45]. Elevated levels of GCs increase adipogenesis, through preadipocyte differentiation rather than adipocyte hypertrophy, inhibits TG synthesis in adipocytes and promotes lipolysis, with a consequent increase of elevated concentrations of FFA and glycerol in the blood [46–49]. Although the molecular mechanisms driving GC's effects are still poorly understood, different studies demonstrated that GCs increase 11b-HSD1 expression in the WAT amplifying the detrimental impact of long-term exposure to GCs [50–52]. In skeletal muscle and WAT, glucose enters cells through a specific glucose transporter GLUT-4. After insulin stimulation, GLUT-4 translocates from the cytosol to the membrane, leading to increased GLUT-4 density and glucose transport. GCs treatments reduce the insulin-induced glucose uptake with a downregulation of GLUT-1 expression and a decreased translocation of GLUT-4 to the plasma membrane. Additionally, it has been demonstrated that treatments with dexamethasone (DEX) decreased the expression and phosphorylation of

IRS-1, indicating a direct impact of GCs on insulin signalling [53]. Acute GCs treatments also induce the early expression and phosphorylation of CCAAT/enhancer-binding protein alpha (C/EBPα), a pro adipogenic transcription factor and increase the expression of Peroxisome proliferator-activated receptor gamma (PPAR-γ), involved in the differentiation of white preadipocytes [54–56]. GCs also impact the secretion of leptin and adiponectin by the adipose tissue [57], which in loop, modulates the GCs production by the Heparanase (HPA1) [58]. In addition, GCs promotes pro-inflammatory M1 and anti-inflammatory M2 macrophage recruitment in adipose tissue via the secretion of TNF-α, C-C motif chemokine 2 (MCP-1), and IL-6 [59].

At the same time, GR pathway is over-activated in liver, leading to IR with increased blood glucose levels and an associated lipogenesis. GCs enhance gluconeogenesis in liver by promoting the expression and the activity of PEPCK enzyme, which is involved in the neoformation of glucose. After the binding to GCs, GR acts in synergy with different factors, such as peroxisome proliferator-activated receptor γ-coactivator 1-α (PGC-1-α), [60]. PGC-1-α expression (*PGC1A*) is necessary to promote the activation of PEPCK. Furthermore, PGC-1-α regulates the expression of *IRS1/2* in hepatocytes, preparing the response to insulin during the fast-to-fed transition [61]. GCs treatments can also act on hepatic metabolism through the activation of other targets such as an increase in adenosine monophosphate-dependent kinase (AMPK) activity, involved into hepatic lipogenesis.

In the end, GCs exposure alters β cell function, with a decrease of glucose sensitivity and insulin secretion, resulting into β cell death. DEX treatments reduce response of β cell to glucose by decreasing GLUT-2 protein level [62], and the insulin release through the upregulation of Serine/threonine-protein

kinase (SGK1), which increases repolarizing activity of K^+ channels, reducing then $Ca2^+$ channels activity and insulin vesicles exocytosis [63].

1.2.2.2. Osteoporosis

Long-term GCs therapy is the most common cause of secondary osteoporosis, which leads to an increased risk of fractures [64,65]. Osteoporosis is a systemic skeletal disorder characterized by low bone mass and micro-architectural deterioration of bone tissue, due to an imbalance between bone resorption and bone formation [66,67]. In physiological conditions, bone is constantly undergoing remodelling. Bone homeostasis is based on two main types of cells: osteoblasts and osteoclasts, responsible for deposition and resorption of the bone matrix respectively. The balance between these two cell types is regulated by several hormones, including parathyroid hormone (PTH), vitamin D, growth hormone, steroids, and calcitonin, as well as several bone marrow-derived membrane and soluble cytokines and growth factors such as Macrophage colony-stimulating factor (M-CSF), Receptor activator of nuclear factor kappa-B ligand (RANK-L), Vascular endothelial growth factor (VEGF) and IL-6 family [68].

Calcium metabolism regulates bone turnover: deficiency of calcium and vitamin D leads to impaired bone deposition. At the same time parathyroid glands react secreting PTH, which increases bone resorption to ensure sufficient calcium in the blood. In contrast, thyroid releases calcitonin, antagonist of PTH, that allows the resorption of calcium and increases bone deposition [69].

Osteoclasts activation is regulated by RANK-L [66]. RANK-L is produced by osteoblasts and lymphocytes and binds RANK (Receptor activator of nuclear factor κB) located on monocytes surface, inducing osteoclastogenesis and bone resorption. Osteoblasts also produce Osteoprotegerin (OPG) that competes with RANK to bind RANK-L, inhibiting bone resorption.

Osteoporosis may be caused by:

- Reduction of bone matrix formation
- Excessive bone resorption

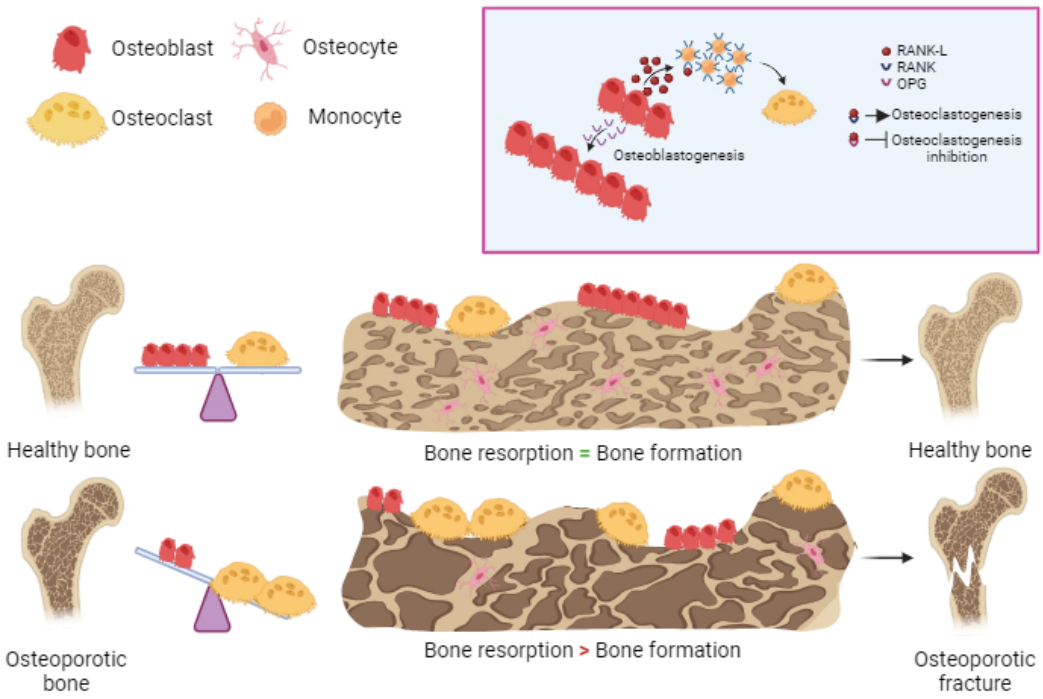

Figure 4. Bone remodelling in healthy conditions and osteoporosis. Bone formation and resorption are mainly regulated by the interplay between osteoblasts and osteoclasts. Osteoblasts secrete RANK-L and OPG that regulate osteoclasteogenesis and osteoblastogenesis processes. RANK-L binds RANK, located on monocytes surface, and induce osteoclasts formation. OPG enhances osteoblastogenesis by blocking RANK-L and monocyte fusion. Under osteoporosis conditions, the imbalance shifts toward greater osteoclasts formation and thus bone resorption overlays bone deposition, resulting in a higher frequency of fractures.

Different studies demonstrated that GCs inhibit osteogenesis [70,71]. In particular, MSCs isolated from bone marrow and treated with GCs showed impaired osteogenesis [72]. GCs also suppress proliferation and differentiation while induce apoptosis of osteoblasts and osteocytes, resulting in a low bone mass [73,74]. Moreover, GCs reduce the amount of RANK-L

secreted by osteoblasts and osteocytes. In turn, this increases the RANK-L/OPG ratio and enhances bone resorption by osteoclasts [75–77].

On the other hand, excessive GCs improve osteoclasteogenesis during the initial phases of the therapy. GCs promote osteoclasts differentiation and proliferation and increase bone resorption [78–81]. However, the long-term therapy with GCs shows contrasting effects. Some studies reported that long-term GCs treatments reduce osteoclasts activity due to disrupted cytoskeleton of the osteoclasts [81,82] or induce osteoclast apoptosis, while others reported that GCs do not affect osteoclast apoptosis at all [83,84].

1.2.2.3. Mitochondrial dysfunctions

Mitochondria play a key role in cellular metabolism. The main role of mitochondria is the production of Adenosine triphosphate (ATP), by oxidizing the major products of glucose: pyruvate and Nicotinamide adenine dinucleotide (NADH), which are produced in the cytosol [85]. Mitochondria functions are determined by their morphology and by the expression levels of enzymatic complexes involved in oxidative phosphorylation [86]. Mitochondria produce a small amount of superoxide anion radicals (O_2^-), but an imbalance between the production and the removal of the superoxide radicals cause mitochondrial damages [87,88]. Mitochondrial dysfunctions may lead to IR in pancreas, skeletal muscle, fat and liver [89–91]. In beta pancreatic cells for example, the overexpression of PGC-1-α induced by GCs stimulates mitochondrial biogenesis and respiratory activity, but at the same time increases oxidative stress and impairs insulin secretion in response to glucose [92]. It was observed that DEX-treated mice displayed alteration in hepatocytes mitochondrial DNA (mtDNA), which led to an increase of ROS production and a reduction of ATP synthesis [93]. Furthermore, another study showed that in SCAT of Cushing's patients the expression of

mitochondrial proteins NADH-ubiquinone oxidoreductase chain 5 (MT-ND5), NADH dehydrogenase [ubiquinone] 1 alpha subcomplex assembly factor 2 (NDUFA12), Succinate dehydrogenase [ubiquinone] flavoprotein subunit, mitochondrial (SDHA), Cytochrome c (CYC1), Cytochrome c oxidase subunit 4 isoform 1, mitochondrial (COX4I1), Dihydrolipoyllysine-residue acetyltransferase component of pyruvate dehydrogenase complex, mitochondrial (DLAT) and Citrate synthase (CS) was significantly decreased [94].

1.3. MSCs and Cushing's syndrome

The involvement of MSCs in Cushing's syndrome is still poorly understood. In our previous work we demonstrated that MSCs isolated from skin biopsies of Cushing's patient secreted decreased levels of cytokines and genes related to wound healing [95], backdating the onset of this pathology at stemness level.

Physiological levels of GCs are essentials for normal osteoblasts and adipocytes differentiation. However, long-term exposure to GCs compromises the differentiation capability of MSCs. *In vitro* studies demonstrated that mouse BM-MSCs treated with DEX differentiate more into adipocytes than osteoblasts [96]. Low concentrations of DEX promote the proliferation of BM-MSCs, whereas increased levels inhibit their proliferation [97]. GCs also attenuate the osteoblast cell cycle by the Tumor suppressor p53 activation [98]. On the other hand, GCs excess induces the expression of PPAR-γ and C/EBP members (C/EBPα, β, and δ), which promote adipogenic differentiation and decrease osteoblastogenesis in BM-MSCs [99,100]. Despite these studies clarify the shift between osteogenic and adipogenic differentiation, the role of MSCs in metabolism and bone dysfunctions has to be further studied.

2. AIM OF THE STUDY

Relevant comorbidities and clinical problems in CS represent a high risk for acute complications. Although there are therapeutic recommendations for most of these comorbidities, new prospective studies are necessary to optimise them. Since, among the others, bone and fat are compromised by CS's comorbidities and cells of both these tissues derive from MSCs, these mesenchymal cells represent a promising model to better understand the development of CS' comorbidities and a promising new therapeutic target. As matter of fact, this PhD work presents three main tasks in which the involvement of MSCs in CS was evaluated.

TASK1: Establish an *in vitro* mesenchymal stem cell model of chronic hypercortisolism

A regular circadian rhythm of cortisol levels is essential for a variety of physiological processes, such as metabolism, immune response, cardiovascular activity and brain function. In CS the circadian rhythm of GCs is compromised, and a constant high concentration of GCs is detected in serum and saliva of these patients. Given its longer half-life (36 hours), elevated concentrations of DEX are the most widely glucocorticoids used in *in vitro* studies of CS. However, none of these studies considers the circadian rhythm of GCs and the difference between physiological and pathological level variations during the day. Therefore, to mimic the circadian cortisol rhythm and chronic hypercortisolism, MSCs isolated form abdominal skin biopsies were isolated and treated *in vitro* with two different GCs systems; subsequently, glucose uptake, IR and FFA metabolism were evaluated.

TASK2: GCs effects on osteoblasts and osteoclasts differentiation in CS

Osteoporosis is one of the main comorbidities in CS. A functional crosstalk between osteoblasts and osteoclasts is crucial for the bone homeostasis. In osteoporosis this crosstalk is compromised, and it results in an imbalance of

osteoblasts/osteoclasts activity. To date, despite the effects of glucocorticoids on bone cells has received lots of attention, the mechanisms that inhibit osteoblastogenesis are not completely understood and few studies were conducted on human MSCs. To better understand the osteoblasts/osteoclasts imbalance in CS, MSCs and PBMCs were isolated from skin biopsies and blood of Cushing patients and differentiate into osteoblasts and osteoclasts, respectively. Differentiation capability and cellular activity were then evaluated in both cell types.

TASK3: Mitochondrial alterations in MSCs of Cushing's patients

The link between mitochondria and metabolic dysfunction is compelling, but far from completely understood. Mitochondria functions are determined by their morphology and their activity in oxidation-reduction processes. To assess mitochondrial efficacy in CS, some of mitochondrial parameters (related to morphology and function) were analyzed in MSCs isolated from skin biopsies of CS patients.

3. MATERIALS AND METHODS

3.1. Patients enrollment and ethical statement

These studies were conducted in collaboration with the Clinic of Endocrinology, Clinic of Dermatology and Clinic of Plastic and Reconstructive Surgery of Università Politecnica delle Marche.

For the TASK1, seven abdominal skin biopsies were collected from four healthy males and three healthy females (age matched 42.3 ± 3.4) undergoing abdominoplasty. The main demographical and clinical characteristics of enrolled patients are summarized in Table 1a.

Five heathy subjects and fifteen Cushing's patients were enrolled for the study 2 and 3 and skin biopsies from the back were collected. Cushing's patients were divided into three subgroups summarized in Table 1b.

(a)

Case	Age	Sex	Mean fasting glucose mmol/L	Mean glycosylated haemoglobin mmol/mol	Mean fasting insulin pmol/L	Mean total cholesterol mmol/L	Mean HDL cholesterol mmol/L	Mean triglycerides mmol/L
1	45	M	5.2	36	35.5	4.1	1.6	1.1
2	48	M	4.9	27	28.4	4.7	1.1	1.4
3	39	M	5.7	39	127.1	5	0.9	2
4	37	M	5.2	35	82.9	5.	1.3	2
5	47	F	5.6	33	115.6	5.1	1.6	1.9
6	36	F	5.2	31	30.8	5	1.9	1.3
7	44	F	4.9	37	32.4	4.7	1.7	1.7
Mean	42		5.3	34	64.7	4.8	1.4	1.6
SD	±4		±0.2	±3	±43.2	±0.3	±0.3	±0.3

(b)

Case	Age	Sex	Group	24h Urinary cortisol time xULN	Disease duration from diagnosis (months)
1	59	F	C-PBMCs/MSCs		
2	63	F	C-PBMCs/MSCs		
3	67	M	C-PBMCs/MSCs		
4	46	F	C-PBMCs/MSCs		
5	50	M	C-PBMCs/MSCs		
6	51	F	ENDO-PBMCs/MSCs	4.5	36
7	49	F	ENDO-PBMCs/MSCs	4	30
8	33	F	ENDO-PBMCs/MSCs	4	12
9	49	M	ENDO-PBMCs/MSCs	5	12
10	50	F	ENDO-PBMCs/MSCs	4.5	30
				Type, dose and duration of steroid treatment	
11	65	F	EXO-PBMCs/MSCs	Oral Prednisone 25 mg/daily – 24 weeks	
12	58	F	EXO-PBMCs/MSCs	Oral Prednisone 25 mg/daily – 24 weeks	
13	65	M	EXO-PBMCs/MSCs	Oral Methylprednisolone 16 mg/daily – 36 weeks	
14	57	M	EXO-PBMCs/MSCs	Oral Prednisone 25 mg/daily – 24 weeks	
15	54	F	EXO-PBMCs/MSCs	Oral Prednisone 25 mg/daily – 24 weeks	
				Type, dose and duration of steroid treatment	**Type, dose and duration of steroid sparing**
16	65	F	EXO SS-PBMCs/MSCs	Oral Prednisone 12,5 mg/daily – 24 weeks	Oral Azathioprine 100 mg/daily − 24 weeks
17	69	F	EXO SS-PBMCs/MSCs	Oral Prednisone 10 mg/daily – 24 weeks	Oral Azathioprine 150 mg/daily − 24 weeks
18	59	M	EXO SS-PBMCs/MSCs	Oral Methylprednisolone 8 mg/daily – 36 weeks	Oral Mycophenolate sodium1440 mg/daily – 36 weeks
19	74	M	EXO SS-PBMCs/MSCs	Oral Prednisone 12,5 mg/daily – 24 weeks	Oral Azathioprine 100 mg/daily − 24 weeks
20	54	F	EXO SS-PBMCs/MSCs	Oral Prednisone 10 mg/daily – 24 weeks	Oral Azathioprine 150 mg/daily − 24 weeks

Table 1. Demographical and functional characteristics of enrolled patients for TASK1 **(a)**, and TASK2 and 3 **(b)**.

All patients provided their written informed consent to participate in the study, which was approved by the institutional ethics committees (NR 2021-218) and conducted in accordance with the Declaration of Helsinki.

3.2. Isolation of MSCs and cell culture

Skin biopsies were mechanically fragmented in small pieces (2-3mm^3) and cultured with MSCGM bullet kit (Mesenchymal Stem Cell Growth Medium, Lonza, Verviers, Belgium) at 37°C and 5% of CO_2 [101–103]. MSCs morphology and growth were evaluated by phase-contrast microscopy (Leika DM IL, Leika® Microsystems GmbH, Germany) and medium was replaced 2 times/week. Once confluence was reached, cells were detached by using 1X Trypsin-EDTA (Lonza) and viability was assessed by an automated cell counter (Invitrogen, Thermo Fisher Scientific, Waltham, Massachusetts, USA). Cells were then cultured in DMEM/F-12 (Dulbecco's Modified Eagle's Medium/Hams F-12 50/50 Mix, Corning, New York, USA) with 10% of FBS (Fetal Bovine Serum, Corning), 1X of Penicillin/Streptomycin and 1X of Glutamine (Lonza).

3.3. Characterization of MSCs

After samples collection, cells isolated from skin biopsies were characterized by testing the minimal criteria identified by Dominici for mesenchymal definition: plastic adherence, fibroblastic morphology, immunophenotype and multipotency [5].

Immunophenotype

MSCs' immunophenotype was analyzed by flow cytometric analysis. $1x10^6$ cells for each sample was incubated with a primary antibody (mouse anti-human; $10\mu g/10^6$ cells) conjugated with FITC (fluorescein isothiocyanate) for 40min at room temperature and in the dark. The primary antibodies (Becton Dickinson, New Jersey, USA) against HLA-DR (Cat. No. 555560), CD14 (Cat. No. 555397), CD19 (Cat. No. 555412), CD34 (Cat. No. 555821), CD45 (Cat. No. 561865), CD73 (Cat. No. 561254), CD90 (Cat. No. 561969), CD105 (Cat. No. 561443) were used. Flow cytometric analyses were carried out with FACSCalibur Flow Cytometer: 3-Color (Becton Dickinson)

equipped with a 15mW laser. 10000 events were acquired per sample and cells were gated according to physical parameters and histograms developed by using FlowJo™ Software (available online at https://www.flowjo.com/) with the percentage of positive events. Furthermore, the expression of CD9 (Cat. No. 555371) was evaluated as distinguishing marker between fibroblasts and mesenchymal cells.

Multipotency

The osteogenic, chondrogenic and adipogenic differentiation of MSCs was induced by using the commercial STEMPRO® Osteogenesis (Cat. No. A1007201), Chondrogenesis (Cat. No. A1007101) and Adipogenesis (Cat. No. A1007001) Kits (GIBCO, Invitrogen) respectively. Cells cultured in DMEM/F-12 with 10% FBS were used as a negative control. All the images were captured using an optical microscope (Nikon Eclipse 600, Nikon, Milan, Italy).

Osteogenic differentiation

For osteogenic differentiation, 15000 cells/well were seeded on 24-well coverslips and cultured for 21 days.

Alkaline phosphatase (ALP) activity and Alizarin Red staining were assessed at 7 and 21 days of differentiation, respectively. For ALP, cells were incubated for 10min in 0.1M TBS pH 9.5 buffer solution (100 mM Tris–HCl pH 9.5, 100 mM NaCl and 10 mM MgCl2) and then with 0.02% 5-Bromo-4-chloro-3-indolyl phosphate disodium salt (BCIP), 0.03% Nitroblue tetrazolium chloride (NBT) and 50mM levamisol in 0.1MTBS, pH 9.5 (Sigma-Aldrich, St. Louis, Missouri, USA) at 37°C. For Alizarin Red staining, cells were previously fixed with 4% paraformaldehyde (PFA) at RT for 15min and then incubated with 2% Alizarin Red-S solution (Thermo Fisher Scientific) for 30-40min at RT and in the dark.

Chondrogenic differentiation

For chondrogenic differentiation, 1×10^6 cells/sample was centrifuged at 1200 rpm for 5min to obtain pellets which were cultured for 20 days in chondrogenic differentiation medium. At the end of the differentiation period, the pellets were fixed in 4% PFA for 24h. The samples were dehydrated, embedded in paraffin and cut with a microtome to obtain 5µm sections. The sections were rehydrated and exposed to a Safranin-O solution (0.1g in 100% EtOH, working dilution 1: 2 dH2O) for 5min.

Adipogenic differentiation

15000 cells/well were cultured in adipogenic differentiation medium for 14 days. Subsequently, cells were fixed with 4% PFA at RT for 30min and incubated with 60% isopropanol for 5min and then with 500µl of Oil Red work solution (6mL of Oil Red stock solution 0.5% w/v + 4mL H2O) for 30min at RT protected from light.

3.4. TASK1

3.4.1. *In Vitro* Reproduction of Circadian Rhythm and Chronic Excess of GCs

To reproduce *in vitro* the circadian rhythm of GCs and its dysfunction in CS, cells were treated with two different GCs regimens: some were given low, circadian-decreasing GCs doses (Low and Decreasing Exposure, LDE), some were exposed to persistently high GC doses (High and Constant Exposure, HCE), as shown in Figure 1A. In detail, LDE cells were first exposed (8:00 a.m. - 9:50 a.m.) to 500nM hydrocortisone (MedChemExpress, MCE, Monmouth Junction, NJ, USA) and then to decreasing concentrations by replacing the medium with a fresh medium containing 250nM hydrocortisone (9:50 a.m. - 01:50 p.m.) and 100nM (01:50 p.m. - 05:50 p.m. and 05:50 p.m. - 08:00 a.m.) of hydrocortisone [104]. To mimic CS, HCE cells were exposed to 500nM hydrocortisone for 24/24

hours. The 500nM hydrocortisone medium was replaced with fresh medium at the same time as the physiological condition medium was changed.

3.4.2. Daily experimental design

To study the effects of GCs excess *in vitro* on glucose uptake and IR, cells were starved and exposed three times/day to 10mM glucose with or without prestimulation with 1µM insulin (Sigma-Aldrich, St. Louis, Missouri, USA) to resemble daily food uptake as resumed in Figure 1B. Cells derived from each single patient were divided into six experimental groups (Exp):

1) GLU: Cells exposed to glucose;

2) INS+GLU: Cells stimulated with insulin before glucose exposure;

3) LDE+GLU: LDE cells treated with glucose;

4) HCE+GLU: HCE cells treated with glucose;

5) LDE+INS+GLU: LDE cells stimulated with insulin before glucose exposure;

6) HCE+INS+GLU: HCE cells stimulated with insulin before glucose exposure.

In detail, cells were starved overnight with Advanced DMEM/F-12 w/o glucose (Lonza) with 0.5% FBS. At 8:00 a.m., starvation medium was replaced for 30min with a new medium containing hydrocortisone 500nM in groups exposed to GCs. After washing, the cells were glucose starved for 40min with KRPH buffer (20mM HEPES, 5mM $KH2PO_4$, 1mM $MgSO_4$, 1mM $CaCl_2$, 136mM NaCl and 4.7mM KCl, pH 7.4) containing 2% BSA (Sigma-Aldrich) and hydrocortisone. Groups 2, 5 and 6 were then stimulated for 20min with 1µM of insulin. Finally, 10mM glucose were added, and the time sampling was after 20min. The same protocol starting with starvation for 2h in Advanced DMEM/F-12 w/o glucose was repeated two times during the day, and the hydrocortisone concentration in the medium of LDE and

HCE cells varied according to the experimental design. To evaluate the long-term impact on metabolism and IR, the experiment was performed for three days with repeated sampling times after glucose administration: T1, T2 and T3 at 9:50 a.m., 1:50 p.m., 5:50 p.m. of the first day; T4, T5 and T6 at 9:50 a.m., 1:50 p.m., 5:50 p.m. of the second day; T7 at 1:50 p.m. of the third day. The entire experiment was repeated 3 times.

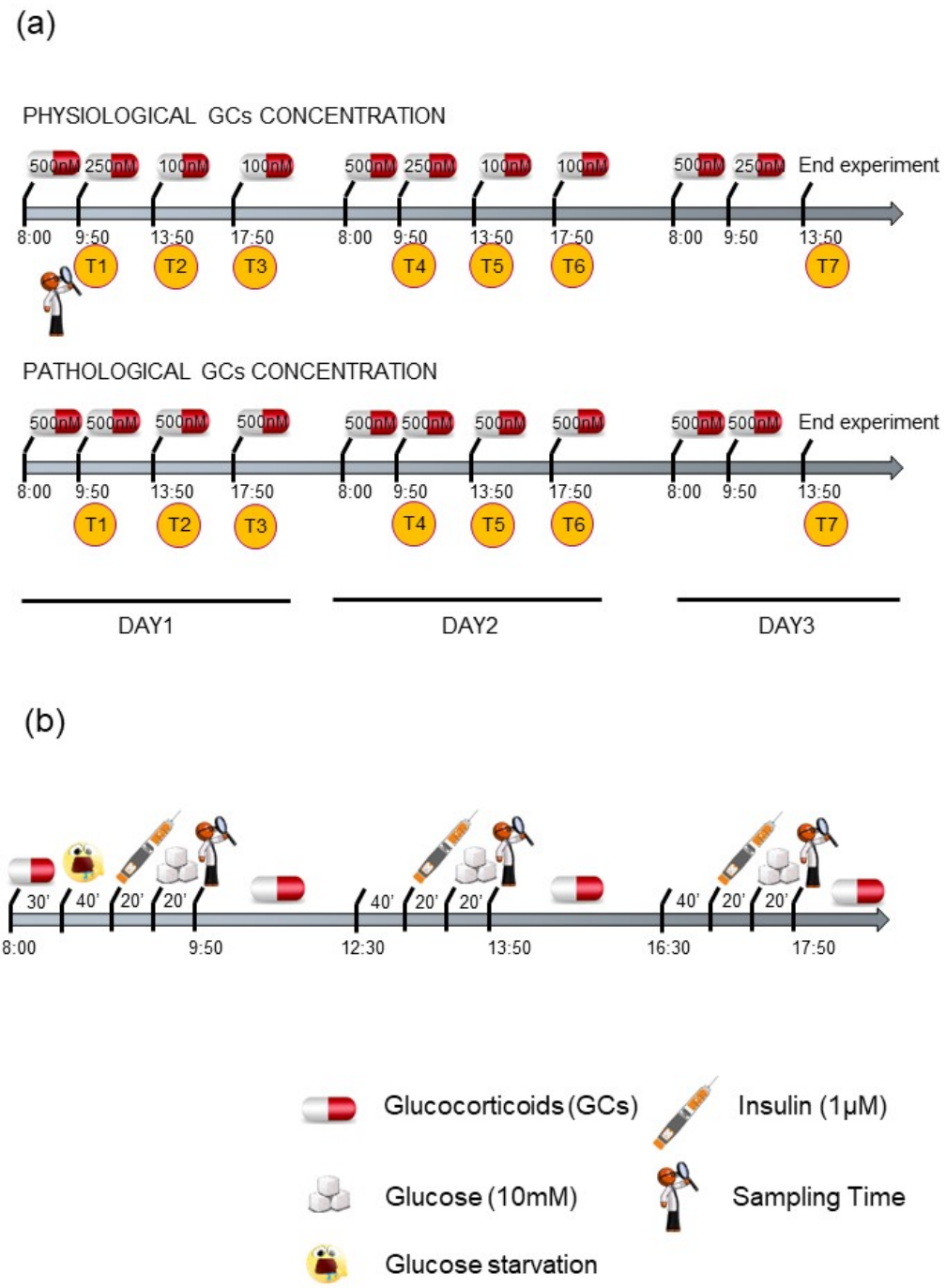

Figure 5. (a) *In vitro* reproduction of preserved versus abolished GC circadian rhythm. **(b).** Daily experimental design.

3.4.3. XTT assay

XTT assay (Sigma-Aldrich) was initially performed to assess that the repeated starvation steps and treatments would not affect cell viability. $3x10^3$ cells/well for Groups 1, 2, 4 and 6 derived from the 7 patients were plated in a 96-well plate in triplicate and treated as previously described. Another experimental group was included as a control, consisting of cells continuously cultured in starvation medium (STARVED CTRL). The XTT assay was performed at the end of each day (T3, T6 and T7 sampling times) following the manufacturer's instructions and absorbance was detected by using microplate reader (Thermo Fisher Scientific, Multiskan GO Microplate Spectrophotometer).

3.4.4. Glucose uptake assay

Glucose uptake assay was first performed to evaluate the response of MSCs to insulin; subsequently, the potential effects of both GC regimens on glucose uptake were evaluated. For the glucose uptake assay (Sigma-Aldrich), $3x10^3$ cells/well were plated in a 96-well plate and treated according to the above protocol; after insulin stimulation, 10mM of 2-deoxyglucose (2-DG) was added for 20min, and a colorimetric assay was performed following the manufacturer's instructions. The readings were detected at 420nm in a microplate reader.

3.4.5. GLUT-4 translocation in MSCs

$1.5x10^4$ cells were seeded on coverslips for groups 1,2,5 and 6 and treated as previously described. A T5 cells were fixed with 4% PFA at RT for 30' and permeabilized for 30min with 0,1% of Tryton 100X (Sigma-Aldrich). Subsequently, cells were incubated overnight at 4°C with anti-GLUT-4 antibody (1:50, Cat. No. SC-53566, Santa Cruz Biotechnology, Dallas, Texas, USA) followed by treatment for 30min with a goat anti-mouse FITC-conjugated antibody (1:1000, Cat. No. F-2761, Invitrogen). Finally,

coverslips were mounted on glass slides in Vectashield (Vectorlabs, CA, USA), and images were acquired by confocal microscopy (Zeiss LSM510/Axiovert 200M microscope with an objective lens at 20× magnification). Line scans were acquired excluding nuclear regions, and GLUT-4 fluorescence was analyzed by calculating the fluorescence ratio between the edge and the centre of the cell [105].

3.4.6. Gene expression in IR development

To investigate the mechanisms involved in IR, the expression of *LIPE*, *ATGL*, *IL-6* and *TNF-α*, was evaluated by semi-quantitative Real-time PCR (RT-PCR) analysis. For each patient, $2.5x10^5$ cells/well belonging to groups 5 and 6 were seeded in triplicates in a 6-well plate and treated following the experimental design. Pellets were collected at T2 and T7, as representing acute and chronic exposure to GCs. RNA extraction, cDNA synthesis and qRT-PCR were carried out as described below. The primer sequences are summarized in Table 2.

Gene	Forward 5'-3'	Reverse 5'-3'
GAPDH	CCCTTCATTGACCTCAACTACATG	TGGGATTTCCATTGATGACAAGC
LIPE	AGCCTTCTGGAACATCACCGAG	TCGGCAGTCAGTGGCATCTCAA
ATGL	CCCACTTCAACTCCAAGGACGA	GCAGGTTGTCTGAAATGCCACC
IL-6	ATTCTGCGCAGCTTTAAGGA	AACAACAATCTGAGGTGCCC
TNF-α	CGAGTCTGGGCAGGTCTACTTT	AAGCTGTAGGCCCCAGTGAGTT

Table 2. IR primer sequences.

RNA extraction and cDNA synthesis

Total RNA was extracted from each pellet with Total RNA Purification Plus Kit (Norgen Biotek Corporation, Thorold, Canada) by following manufactures' instructions. RNA concentration (ng/μl), the ratio 260/280 (protein contamination index) and the ratio 260/230 (phenol contamination

index) were measured by Thermo Scientific™ NanoDrop™ One/OneC Microvolume UV-Vis Spectrophotometer (Thermo Fisher Scientific). cDNA synthesis was performed by following manufacturer's instructions of All-In-One 5X RT MasterMix (Applied Biological Materials-abm, Richmond, Canada). For each sample 200ng of RNA were used.

Semi-quantitative RT-PCR

For qRT-PCR, 1µl of cDNA for each sample was analyzed in duplicate for all genes. The MIX for each sample contains 5µl of SsoFast™ EvaGreen® Supermix (Bio-Rad, Hercules, California, USA), 3.8µl of deionized water and 0.2µl of forward and reverse primers. Subsequently the amplification and analysis were performed with Real-time Mastercycler ep realplex (Eppendorf, Hamburg, Germany). The general protocol includes a first incubation at 95 °C for 2min followed by 45 cycles of 95 °C for 15sec and 60 °C for 1min, 3min at 95°C followed by 45 cycles of 20sec at 95°C (denaturation), 20sec at T melting depending on the primer used (annealing) and 20sec at 72°C (elongation). At the end of each cycle the emission of fluorescence was monitored, and mRNA expression was calculated by the $2^{-\Delta\Delta Ct}$ method [106].

3.5. TASK2

The TASK2 was investigated in 2 steps:

STEP1: Evaluation of the ability of PBMCs isolated from blood samples of healthy subjects and Cushing patients to differentiate into osteoclasts.

STEP2: Evaluation of the ability of MSCs isolated from skin biopsies of healthy subjects and Cushing patients to differentiate into osteoblasts.

3.5.1. STEP1: PBMCs isolation e differentiation into osteoclasts

5mL of blood samples for each patient were collected at the Endocrinology Clinic of Università Politecnica delle Marche in EDTA collecting tubes.

PBMCs extraction was performed by density gradient centrifugation for separation of PBMCs by using Ficoll(R)-Paque PREMIUM (Scientific Laboratory Supplies Ltd, Nottingham, England). In detail, fresh blood was diluted 1:1 with 1X PBS and carefully layered onto a 4mL of Ficoll-Paque solution and subsequently centrifuged at 400g for 30min at RT w/o brakes. After the centrifuge the upper layer containing plasma and platelets was drawed off using a sterile pipette, and PBMCs layer was collected and transferred to a sterile centrifuge tube. After 2 washes with 1X PBS PBMCs were cultured in MEM α w/o phenol red (Gibco, Thermo Fisher Scientific). To induce osteoclasts differentiation, 25ng/mL RANK-L (Human Recombinant RANK-L, STEMCELL Technologies, Vancouver, Canada) and 25ng/mL M-CSF (Human Recombinant M-CSF, STEMCELL) were added to the culture medium. Medium was replaced 2 times/week and all the experiments were performed after 14 days of differentiation. Cells cultured in medium w/o factors were used as negative control.

3.5.2. STEP1: Osteoclasts morphology and activity

To evaluate the differentiation into osteoclasts and their activity, after 14 days of culture cells were analyzed for Tartrate-resistant acid phosphatase 5b (TRAcP), Cathepsin K, acting ring formation, resorption pits and C-terminal telopeptides of Type I collagen (CTX-I) realise.

TRAcP

TRAcP is one of several bone metabolic biomarkers that are specifically secreted by osteoclasts [107,108] and has been used as biomarker of bone resorption. TRAcP is a good indicator of osteoclast number in human blood monocyte-derived osteoclasts. For TRAcP staining, $2.5x10^6$ cells were plated on coverslips in triplicate for each patient and after 14 days of culture acid phosphatase enzymatic staining was performed (Sigma-Aldrich) following manufactures instructions. Nuclei were marked with DAPI Nuclear

Counterstains (4',6-Diamidino-2-Phenylindole, Dihydrochloride, Cat. No. D1306, 1.1000, Thermo Fisher Scientific). All the images were captured using an optical microscope. The analysis was performed on 5 fields/sample. TRAcP positive cells were counted in both differentiated and not differentiated groups, and the percentage calculated on the total number of cells/field. For the analysis, not differentiated group percentage mean has been subtracted from differentiated samples. Only cells with more than 3 nuclei were considered for the analysis.

Cathepsin K

Cathepsin K is responsible for the degradation of type I collagen in osteoclast-mediated bone resorption. To analyze the expression of Cathepsin K, $2.5x10^6$ cells were plated on coverslips in triplicate for each patient and after 14 days of culture an immunocytochemistry was performed. In detail, cells were first fixed with 4% PFA and then permeabilized with 0,1% Triton X100. Subsequently, cells were incubated overnight at 4°C with anti-cathepsin K monoclonal antibody (1:100, Cat. No. SC- 48353, Santa Cruz Biotechnology). After washing in PBS 1X, cells were immunostained using the streptoavidin-biotin-peroxidase technique (LSAB universal peroxidase kit, Dako Cytomation, Milan, Italy), and were incubate with 3,3-diaminobenzidine (DAB). Coverslips were then counterstained with Meyer's haematoxylin, dehydrated, and mounted with Dako Cytomation Glycergel mounting medium. All the images were captured using an optical microscope. The analysis was performed on 5 fields/sample and Cathepsin K positive cells with more than 3 nuclei were counted. The percentage was calculated for both differentiated and not differentiated samples on the total number of cells/field. The percentage mean of not differentiated group has been subtracted from differentiated samples.

Actin ring formation

Rapid cytoskeletal reorganization is essential for osteoclast function. Bone resorption occurs within the sealing zone, which is formed by an actin ring structure. This can be identified as a solid circular belt like formation and consists of an actin filament core [109]. To assess the formation of actin ring, $2.5x10^6$ cells were plated on coverslips in triplicate for each patient and after 14 days of culture an immunofluorescence (IF) was performed. More specifically, cells were first fixed with 4% PFA for 30min at RT and then permeabilized with 0.1% Triton X100 for 10min. Subsequently, cells were incubated with Phalloidin-TRITC (1.1000, Cat. No. P1951, Phalloidin-tetramethylrhodamine B isothiocyanate, Sigma-Aldrich) for 45min at RT and protect from the light. After 3 washes, nuclei were counterstained with DAPI Nuclear Counterstains (1:1000). Fluorescence was detected using an optical microscope. The analysis was performed on 5 fields/sample and actin ring positive cells (nuclei >3) were counted in differentiated and not differentiated samples. The percentage was calculated by considering the total number of cells/field and the mean percentage of not differentiated group has been taken off from differentiated samples.

Resorption pits and CTX-I measurement

To measure osteoclasts activity, $2.5x10^6$cells/well were plated in triplicate and differentiated. After 14 days, cells were detached with 10X Trypsin and seeded onto bone slices (BioVendor, Brno, Czech Republic) and cultured in presence of RANK-L and M-CSF. After 96 h, medium was collected and analysed for CrossLaps® for Culture (CTX-I) ELISA assay (BioVendor) following manufactures instructions, while the bone sections were sonicated in 0.25 mol/L NH4OH for 30min, thereby removing all cells, washed in distilled water, stained with Coomassie brilliant blue and the images were captured with optical microscope). CTX-I fragments were detected using a microplate reader.

3.5.3. STEP2: MSCs differentiation into osteoblasts

To assess differentiation into osteoblasts, MSCs were cultured with StemPro Osteogenesis Differentiation Kit (Gibco, Thermo Fisher Scientific) for 21 days and medium was replaced 2 times/week. Cells cultured in DMEM/F-12 were used as negative control.

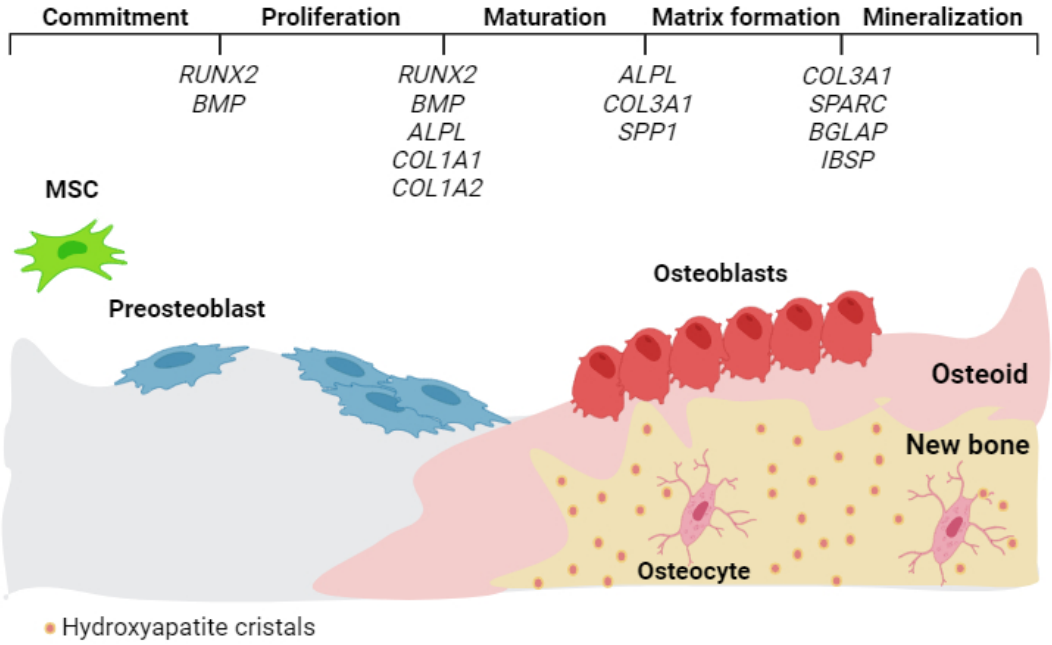

Figure 6. Schematic representation of osteoblastogenesis. MSCs differentiate into osteoblast following multiple steps: commitment to osteoblastic lineage, proliferation and maturation of preosteoblasts, matrix deposition (osteoid) by osteoblasts, and bone matrix mineralization with calcium phosphate deposition and formation of hydroxyapatite crystals (new bone). Osteoblastogenesis is regulated by a cascade activation of transcriptional factors such as *RUNX2* and Bone morphogenetic protein (*BMP*) that induce the expression of Alkaline phosphatase (*ALPL*), Collagen alpha-1 and -2 (I) chain (*COL1A1* and *COL1A2*), specific markers of osteoblasts differentiation during early stages, and followed by Collagen alpha-1(III) chain (*COL3A1*), Sphingosine-1-phosphate phosphatase 1 (*SPP1*), Osteonectin (*ON* also known as *SPARC*), Osteocalcin (*BGLAP*) and Bone sialoprotein 2 (*IBSP*) in tardive (late) stages of differentiation.

MSCs differentiation capacity was evaluated by ALP activity, bone matrix mineralization, collagen deposition, and analysis of genes and proteins related to osteoblastogenesis.

ALP activity

ALP is an early osteogenic marker of bone formation and bone calcification [110]. To evaluate ALP activity, $2x10^4$ cells were seeded in triplicate on coverslips for each patient and differentiate into osteoblast. After 7 (T7) days of differentiation ALP staining and IF were performed. ALP staining was carried out as described in 3.3. paragraph. 5 fields for each sample were acquired by optical microscope. The positive percentage area of both differentiated and not differentiated groups (negative control) was then quantified through Fiji ImageJ (available online on https://imagej.net/software/fiji/downloads) for each field. For the analysis, the percentage mean of negative controls was subtracted from differentiated samples. For IF, cells were fixed and permeabilized as described above. Cells were then incubated overnight at 4°C with Anti-Alkaline Phosphatase monoclonal antibody (1:100, Cat. No. Ab126820, abcam, Cambridge, United Kingdom), followed by 30min of incubation with a goat anti-mouse FITC-conjugated antibody (1.1000, Invitrogen). Subsequently, cells were incubated with Phalloidin-TRITC for 45min and after 3 washes, nuclei were counterstained with DAPI Nuclear Counterstains (1:1000). Fluorescence images (5 fields/sample) were acquired by optical microscope. Fluorescence quantification was analyzed through Fiji ImageJ

Mineralization

The Alizarin Red-S assay is considered the gold standard for quantification of bone matrix mineralization. $2x10^4$ cells were seeded in triplicate on coverslips for each patient and differentiate into osteoblast. After 21 (T21)

days Alizarin Red staining was caried out as described above (3.3. paragraph) and images were acquired with optical microscope. A photometric quantification of Alizarin Red-S concentration was then performed. 250µL of 10% acetic acid were added to each well and 200µL of the supernatant were then transferred to a 96-well plate for photometric measurement. Absorbance was detected at 480nm with microplate reader and Alizarin Red-S concentration was analysed.

Collagen deposition

Osteoblasts differentiation is associated with processing of type I procollagen to collagen I under the effect of ascorbic acid, and progressive deposition of a collagenous extracellular matrix (ECM). Collagen deposition was monitored through Sirius Red before (T0), and after 7 (T7) and 21 (T21) days of differentiation. Briefly, $2x10^4$ cells were seeded in 24-well in triplicate for each patient and induced to differentiate into osteoblasts. At every time sampling cells were fixed overnight in methanol at -18°C. After 3 washes with PBS 1X cells were incubated for 2h at RT with 0.1% solution of Picro-Sirius Red (Direct Red 80, Sigma-Aldrich). Cells were then washed twice with 0.1% aqueous solution of acetic acid and images were acquired with an inverted microscope (Leica microsystem, Wetzlar, Germany). A photometric quantification of Sirius Red concentration was then performed. 250µL of a 0.1 N aqueous solution of sodium hydroxide by shaking in a tilting shaker for 1h, and subsequently 200µL of the eluted stain solution were transferred to 96-well plates. The optical density (OD) was detected with microplate reader at a wavelength of 530nm.

Analysis of genes expression and proteins involved in osteoblast differentiation

Osteoblast differentiation follows different stages: (1) cell proliferation, (2) ECM secretion and matrix maturation and (3) matrix mineralization [111].

As shown in Figure 6, the first stage was determined by the expression of *RUNX2*, followed by the increase of the expression of *ALPL*, *COL1A1*, *SPARC* and *BGLAP,* that were detected by qRT-PCR and WB analysis at T0, T7 and T21. RANK-L/OPG axis was also detected through WB analysis.

Gene expression was carried out as described above in paragraph 3.4.6. The primer list was summarized in Table 3.

Gene	Forward 5'-3'	Reverse 5'-3'
GAPDH	CCCTTCATTGACCTCAACTACATG	TGGGATTTCCATTGATGACAAGC
ALPL	GCTGTAAGGACATCGCCTACCA	CCTGGCTTTCTCGTCACTCTCA
RUNX2	ACTCGTCCGCACCGACAGCC	TACCTCTCCGAGGGCTACCACC
COL1A1	GTGCTAAAGGTGCCAATGGT	CTCCTCGCTTTCCTTCCTCT
COL3A1	TGGTCTGCAAGGAATGCCTGGA	TCTTTCCCTGGGACACCATCAG
SPARC	CAAGAAGGGCCACAAGCTC	TGTTGTCCTCATCCCTCTCA
BGLAP	GACTGTGACGAGTTGGCTGA	GCCCACAGATTCCTCTTCTG

Table 3. Osteoblastogenesis primer sequences

For WB analysis, $2x10^5$ cells were seeded in 6-well plates in duplicate for each sample and induced to differentiate. At T0, T7 and T21 cells were detached and washed with cold PBS. Pellets were lysed with Ripa buffer (Tris-HCl 50Mm pH7.4, NaCl 150mM, Triton X100 1%, SDS 0,1%) supplemented with 1mM PMSF, protease inhibitor cocktail, Phostop (all by Sigma-Aldrich). Protein concentration was measured with DC Protein assay (BioRad) following manufacturing instruction. 10µg of proteins were loaded onto a Bolt 4-12% Bis-Tris Plus precast gel (Invitrogen) and transferred to 0,2µm nitrocellulose membrane (BioRad). Nonspecific binding sites were blocked with 5% skin milk in TBS buffer and nitrocellulose stripes were then incubated overnight at 4°C with primary antibodies: Anti-RUNX2 antibody (1:1000, Cat. No. HPA022040, Sigma-Aldrich); anti-Alkaline Phosphatase monoclonal antibody (1:1000, Cat No. Ab126820, abcam, Cambridge,

United Kingdom), anti-COL1A1 (Cat. No. SC- 293182), anti-RANK-L (Cat. No. SC-52950), anti-M-CSF (Cat. No. SC- 365779) (1:250, Santa Cruz Biotechnology), and GAPDH (1:10000, Cat. No. 60004-1-Ig, Proteintech, Manchester, United Kingdom). Subsequently, membranes were incubated with secondary antibodies goat anti-rabbit HRP conjugated antibody (1:10000, Cat. No. 31460, Invitrogen) or goat anti-mouse HRP conjugated antibody (1:15000, Cat. No. A90-116P, Bethyl Laboratories, Montgomery, TX, USA) for 2h at RT. Clarity Western ECL substrate (BioRad) was used for detection with Alliance Mini HD9 (Uvitec, Cambridge, UK). Densitometric analysis was performed by using Fiji-ImageJ software.

3.6. TASK3

The mitochondrial alterations, related to morphology, mitochondrial membrane potential ($\Delta\Psi$), ROS and ATP production, were evaluated in MSCs isolated from skin biopsies of healthy subjects and Cushing patients.

3.6.1. Mitochondria morphology

To evaluate the mitochondrial morphology, $3x10^4$ cells were plated in triplicate on 13-mm coverslips. After 3 washes with PBS 1X cells were fixed in 4% formaldehyde for 30min at RT, then permeabilized with 0.1% Triton X-100 in PBS for 30min at RT and blocked with PBS containing 2% BSA for 15min. Subsequently, cells were incubated with ATP5I (ATP synthase subunit e, mitochondrial) primary antibody (1:100, Cat. No. ab122241, Thermo Fisher Scientific) for 2h at RT followed by incubation with AlexaFluor488-conjugated secondary antibodies (1:1000, Cat. No. A21206, Thermo Fisher Scientific). Coverslips were mounted with ProLong Diamond Antifade Mountant (Thermo Fisher Scientific) and images were acquired with Zeiss LSM510/Axiovert 200M confocal microscope with an objective lens at 63× magnification. Acquired images were then analyzed by using Fiji-ImageJ software. 2D analysis of mitochondrial function, morphology and

network characteristics was performed by measuring form factor, aspect ratio, branches and branches junctions [112].

3.6.2. ROS production

Cellular and mitochondrial ROS production were assessed by CM-H2DCFDA (General Oxidative Stress Indicator) and MitoSOX™ Red Mitochondrial Superoxide Indicators, respectively (Invitrogen). For both experiments 7.5 x10^4 cells were plated in in triplicate for each sample in a 96-well. After 24h, cells were incubated with 5μM of CM-H2DCFDA or 5 μM of MitoSOX ™ Red diluted in HBSS/Ca/Mg for 30min at 37°C protect from the light. To normalize the fluorescence, cells were also stained with DAPI Solution (1:1000). Three washes with PBS were performed and fluorescence intensities were detected at 340/465nm for Hoechst, at 485/535nm for CM-H2DCFDA and at 535/590nm for MitoSOX by microplate ELISA plate reader (Sunrise™ Absorbance Reader; Tecan Group Ltd). CM-H2DCFDA and MitoSOX Red quantification has been reported as the ratio of CM-H2DCFDA / MitoSOX to DAPI fluorescence.

3.6.3. ΔΨ measurements

ΔΨ was measured by loading cells with tetramethyl rhodamine methyl ester (TMRM, Invitrogen). 7.5 x10^4 cells were plated in triplicate for each sample in a 96-well. After 24h, cells were incubated with 25nM of TMRM for 20min at 37°C protect from the light. Fluorescence intensities were then detected at 535/590nm by microplate ELISA plate reader. Successively, basal levels were normalized on fluorescence by adding 1μM of FCCP (carbonyl cyanide p-trifluoromethoxyphenylhydrazone), a strong uncoupler of oxidative phosphorylation and fluorescence intensities were measured again after 5min. To normalize the fluorescence, cells were also stained with DAPI Solution (1:1000). Fluorescence quantification has been reported as the ratio of TMRM to DAPI fluorescence.

3.6.4. Mitochondrial ATP levels

To study mitochondrial metabolism, mitochondrial ATP levels were detected by the use of luciferase [113]. $3x10^4$cells were seeded in triplicate onto 13mm glass coverslips and transfected for 24h with mtLuc cDNA (4μg/mL, kindly offered by Prof. P. Pinton, Signal Transduction's lab) and cell luminescence was measured in a luminometer. The system comprises a perfusion chamber above a hollow metal cylinder, which is temperature-controlled by a couple of tubes connected to a thermostatic group and is continuously perfuse with solutions via a peristaltic pump. Cells were constantly perfused with a modified Krebs-Ringer buffer (135mM NaCl, 5mM KCl, 0,4mM KH2PO4, 1mM MgSO4, 20mM HEPES and 5,5 mM of glucose; pH 7.4) supplemented with 1mM $CaCl_2$. The emission of light has been detected by using a photon counting detector (Hamamatsu Photonics, Japan). Under these conditions, the background light output was lower than 100 count per seconds (cps). The subsequent perfusion of luciferin solution (modified KRB solution supplemented with 25μM luciferin; Beetle Luciferin, Potassium Salt, Promega, Madison, Wisconsin, USA) to the cell population activates luciferase, which catalyses light production in the presence of ATP, Mg^{2+} and O_2, and hence increases the signal detected (cps), until reaches a plateau in several seconds that indicates the ATP content in mitochondria. Mitochondrial Ca^{2+} accumulation triggers ATP synthesis in mitochondria. Thus, the perfusion of cells by CMS (Ca^{2+} mobilizing solution) promotes mitochondrial ATP synthesis and this results in an increase in cps value until the recement of a second plateau. To evoke Ca^{2+} discharge from the endoplasmic reticulum and rapid Ca^{2+} accumulation inside mitochondria 100μM of Bradykinin (Sigma-Aldrich) were used as CMS. ATP production was expressed as the ratio between the plateau reached upon $Ca2^{+}$ dependent stimulation and the plateau reached in the first part.

3.7. Statistical Analysis

GraphPad Prism 6 Software was used for statistical analysis. Data are expressed as the mean ± standard deviation (SD). For parametric analysis all experimental groups were first tested for normal distribution by the Shapiro–Wilk test [114] and comparison between 2 groups was performed by unpaired Student's t-test. For multiple comparisons, the one-way ANOVA test (Tukey's multiple comparisons test) was used. Significance was set at p value < 0.05.

4. RESULTS

4.1. MSCs characterization

MSCs were isolated from skin biopsies and characterized according to Dominici's criteria [5]. As resumed in Table 4, MSCs of TASK1 and TASK2/3 were positive for CD73, CD90 and CD105, and negative for HLA-DR, CD14, CD19, CD34 and CD45, and presented a very low expression of CD9, confirming the specific immunophenotype of MSCs.

	TASK1	TASK2/3			
	MSCs	C-MSCs	ENDO-MSCs	EXO-MSCs	EXO SS-MSCs
CD73	+	+	+	+	+
CD90	+	+	+	+	+
CD105	+	+	+	+	+
CD14	-	-	-	-	-
CD19	-	-	-	-	-
CD34	-	-	-	-	-
CD45	-	-	-	-	-
HLA-DR	-	-	-	-	-
CD9	+/-	+/-	+/-	+/-	+/-

Table 4. MSCs immunoprofiling. Antigens expressed by more than 90% of the cell population were considered positive (+); Expression percentages lower than 2% were evaluated as negative (-).

As shown in Figure 7 cells were also able to differentiate towards osteogenic, chondrogenic and adipogenic lineages. After 7 days of osteogenic differentiation, MSCs showed ALP activity, and after 14 days, cells were strongly positive for Alizarin Red staining. MSCs differentiation into adipocytes occurred after 21 days, as evidenced by the presence of lipid vacuoles after Oil Red staining. Chondrogenic differentiation was achieved

after 30 days, as shown by Safranin-O staining (Figure 7a). Figure 7b represents the differentiation of C-MSCs, ENDO-MSCs, EXO-MSCs and EXO SS-MSCs towards chondrogenic and adipogenic lineages as the osteogenic was studied in depth during this work and results displayed later.

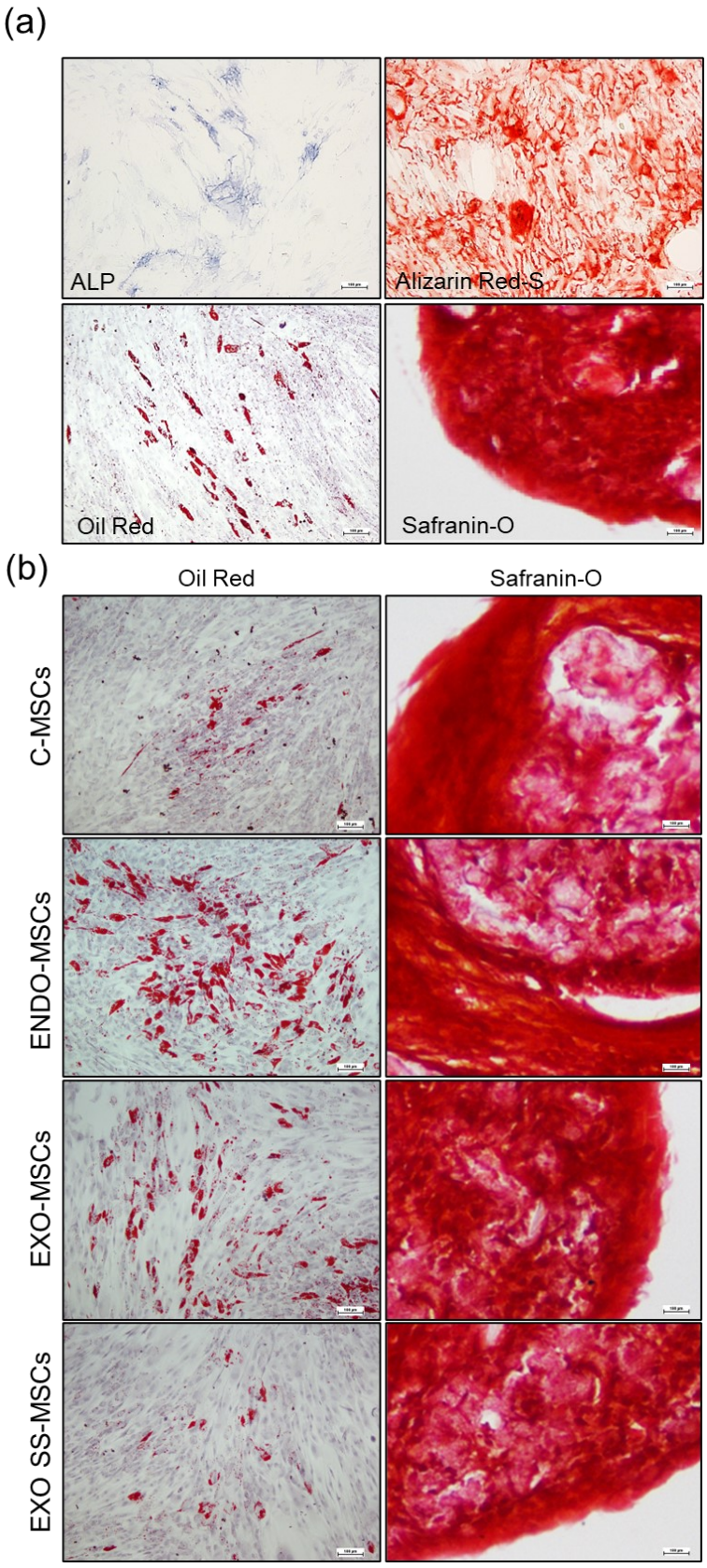
(a)
ALP
Alizarin Red-S
Oil Red
Safranin-O
(b)
Oil Red
Safranin-O
C-MSCs
ENDO-MSCs
EXO-MSCs
EXO SS-MSCs

Figure 7. MSCs multipotency. (a) Representative images of MSCs isolated from abdominal skin of healthy subject (C-MSCs) enrolled in TASK1 and induced to differentiate toward osteogenic lineage as assessed by ALP and Alizarin Red-S staining (scale bar 100μm); chondrogenic lineage as indicated by Safranin-O staining (scale bar 100μm) and adipocyte lineage as confirmed by Oil red staining (scale bar 100μm). **(b)** Representative images of MSCs isolated from back skin of C-MSCs and Cushing patients (ENDO-, EXO-, EXO SS-MSCs) differentiated toward adipocyte lineage as demonstrated by Oil red staining (scale bar 100μm) and chondrogenic lineage as indicated by Safranin-O staining (scale bar 100μm).

4.2. TASK1

4.2.1. Treatments with starvation and GCs don't affect cellular viability

To assess that the repeated starvation steps and treatments did not affect cell viability, XTT analysis was performed at the end of each day of treatments (T3, T6 and T7 sampling time). Experimental groups w/o GCs treatments (GLU and INS+GLU) and with the highest concentration of GCs (HCE+GLU and HCE+INS+GLU) were compared to STARVED CTRL (cells continuously cultured in starvation medium). The results reported in Figure 8 displayed that the viability of STARVED CTRL was initially increased compared to the other groups. Although repeated manipulations caused a proliferation block earlier than starvation alone, the different treatments did not interfere with vitality, and further analyses on glucose uptake were conducted.

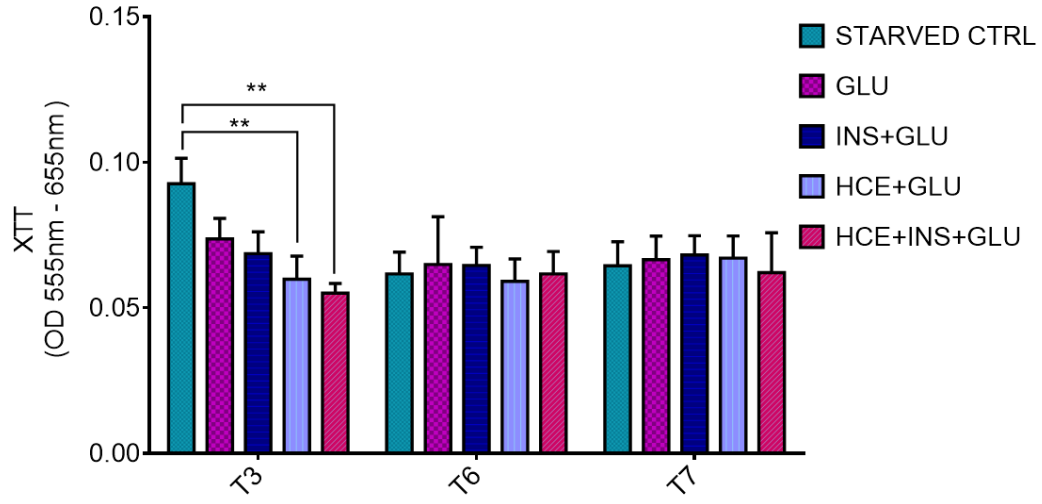

Figure 8. Cells viability at T3, T6 and T7 sampling times. Bars represent XTT absorbance of experimental groups at the end of each day of treatments (T3, T6 and T7). Data are expressed as mean ± SD of the absorbance read for MSCs derived from the abdominal skin of each single healthy subject over three independent experiments. One-way ANOVA; **$p < 0.01$.

4.2.2. Insulin stimulation improve glucose uptake via GLUT-4 translocation

Before the evaluation of the effects of GCs excess on MSCs metabolism, the response of MSCs to insulin stimulations was detected assessing glucose uptake and GLUT-4 translocation. As shown in Figure 9, stimulation with insulin significantly increased glucose uptake in MSCs at T1, T2, T4 and T5.

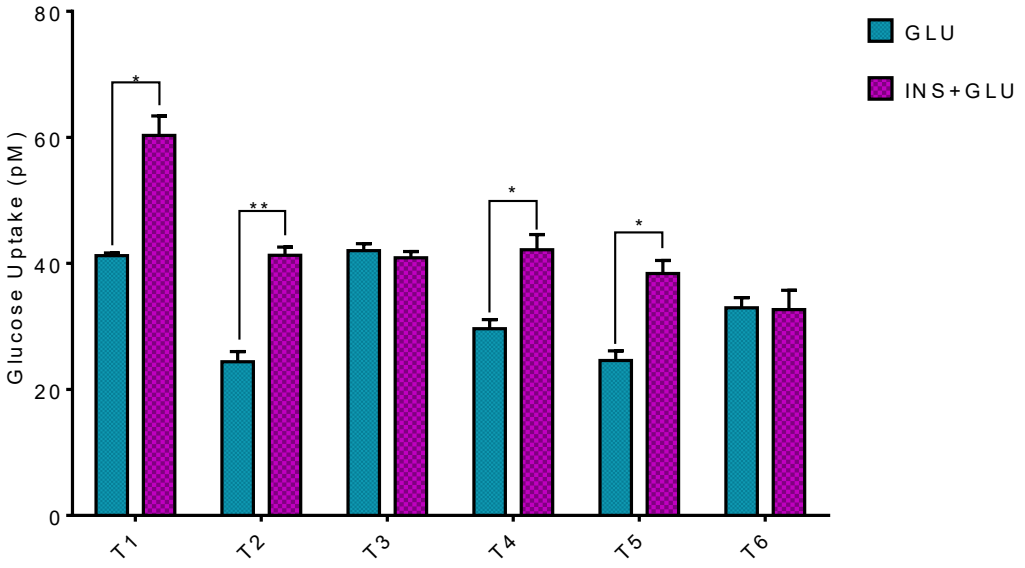

Figure 9. Responsiveness of MSCs to insulin. The bars show the glucose uptake expressed in pM at T1, T2, T3, T4, T5 and T6 in insulin-stimulated or non-stimulated MSCs. Data are expressed as mean ± SD of the analysis for MSCs derived from the abdominal skin of each single healthy subject over three independent experiments. Unpaired t-Student's test; *$p < 0.05$, **$p < 0.01$.

Furthermore, in the absence of insulin, GLUT-4 was more localized in the perinuclear area of the cells (Figures 10 a, e) and insulin stimulations enhanced GLUT-4 translocation towards the plasma membrane (Figures 10 b, f).

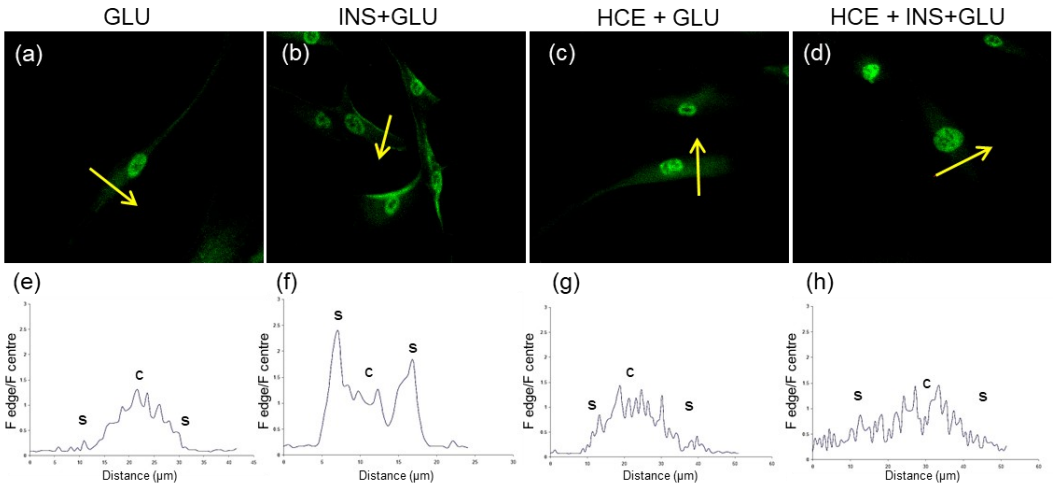

Figure 10. GLUT-4 translocation. Representative confocal images of GLUT-4 in MSCs derived from the abdominal skin of seven healthy subjects and stimulated **(b, d)** or not **(a, c)** with insulin and constantly exposed to high concentrations of GCs **(c, d)**. The graphs **(e–h)** show the fluorescence ratio between the edge and the centre of the cell; yellow arrows indicate the portion of cell subjected to analysis.

4.2.3. HCE conditions reduce GLUT-4 translocation and glucose uptake in MSCs

In LDE cells, insulin stimulations improved glucose uptake at all sampling times (Figure 11). In contrast, HCE treatments didn't affect cells in the acute period (T1, T2) but led to a significant decrease in glucose uptake when prolonged (T3, T5, T6, T7). In addition, despite insulin stimulation, GLUT-4 translocation was inhibited by HCE treatments (Figures 10 c, g and d, h).

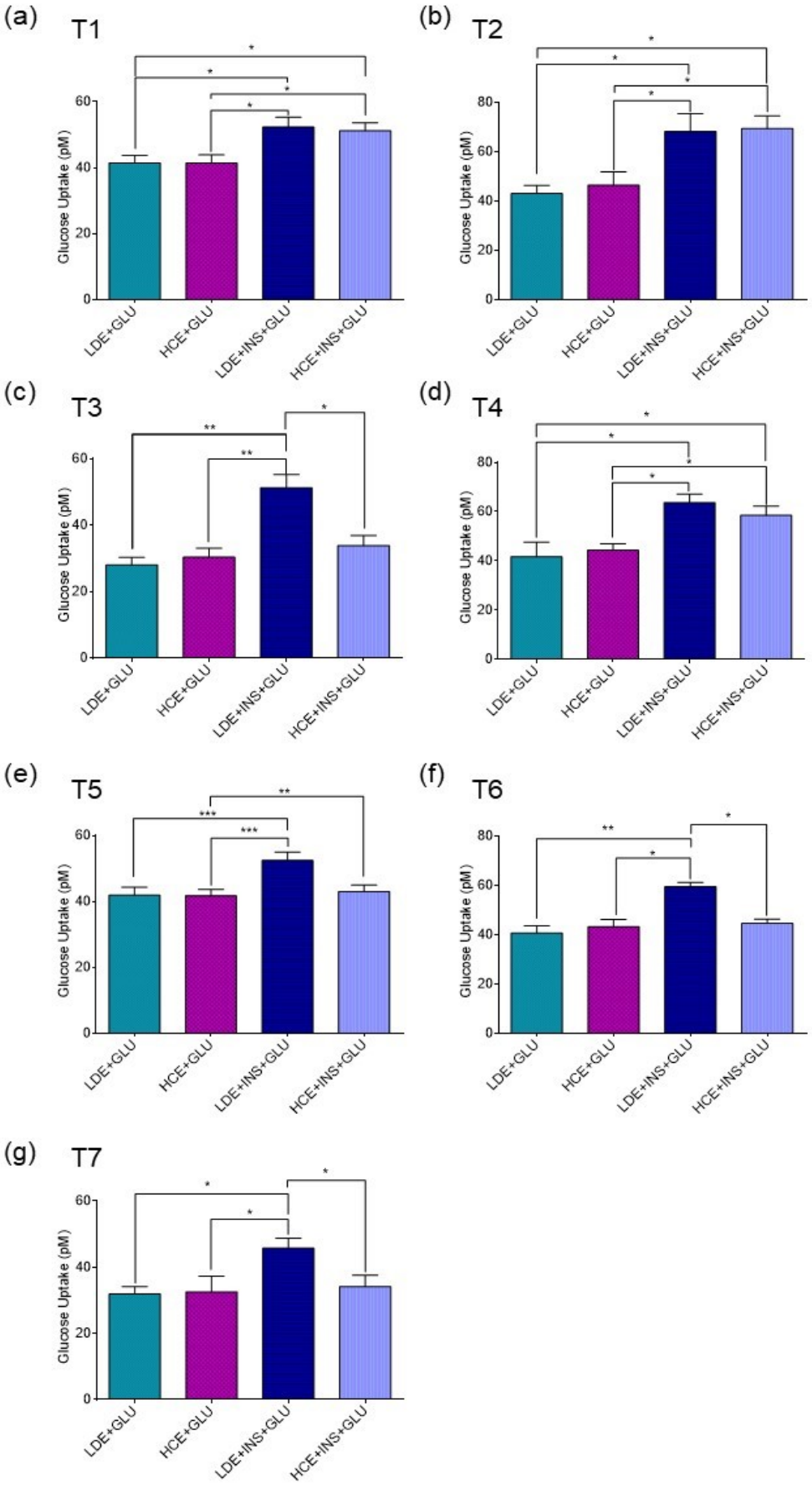
(a)
T1
Glucose Uptake (pM)
LDE+GLU
HCE+GLU
LDE+INS+GLU
HCE+INS+GLU
(b)
T2
(c)
T3
(d)
T4
(e)
T5
(f)
T6
(g)
T7

Figure 11. Glucose uptake in MSCs undergoing a LDE or a HCE to GCs. The bars represent the glucose uptake expressed in pM at T1 (9:50 a.m. first day, **a**), T2 (1:50 p.m. first day, **b**), T3 (5:50 p.m. first day, **c**), T4 (9:50 a.m. second day, **d**), T5 (1:50 p.m. second day, **e**), T6 (5:50 p.m. second day, **f**) and T7(1:50 p.m. third day, **g**) in MSCs isolated from abdominal skin of healthy subjects undergoing a LDE or a HCE to GCs and stimulated or not with insulin. Data are expressed as mean ± SD of the readings for MSCs derived from each single patient over three independent experiments. One-way ANOVA; *p < 0.05,**p < 0,01,***p < 0,001.

4.2.4. HCE conditions induce lipolysis and IR in MSCs

To better understand the mechanisms involved in IR, the expression of genes related to lipolysis (*LIPE* and *ATGL*) and early biomarkers of IR (*IL6* and *TNFA*) was investigated. *LIPE*, *ATGL* and *TNFA* were downregulated at T2, whereas at T7 their expression was significantly increased in HCE cells compared to LDE cells. At T7, HCE cells also showed a significant increase in the expression of *IL6* (Figure 12).

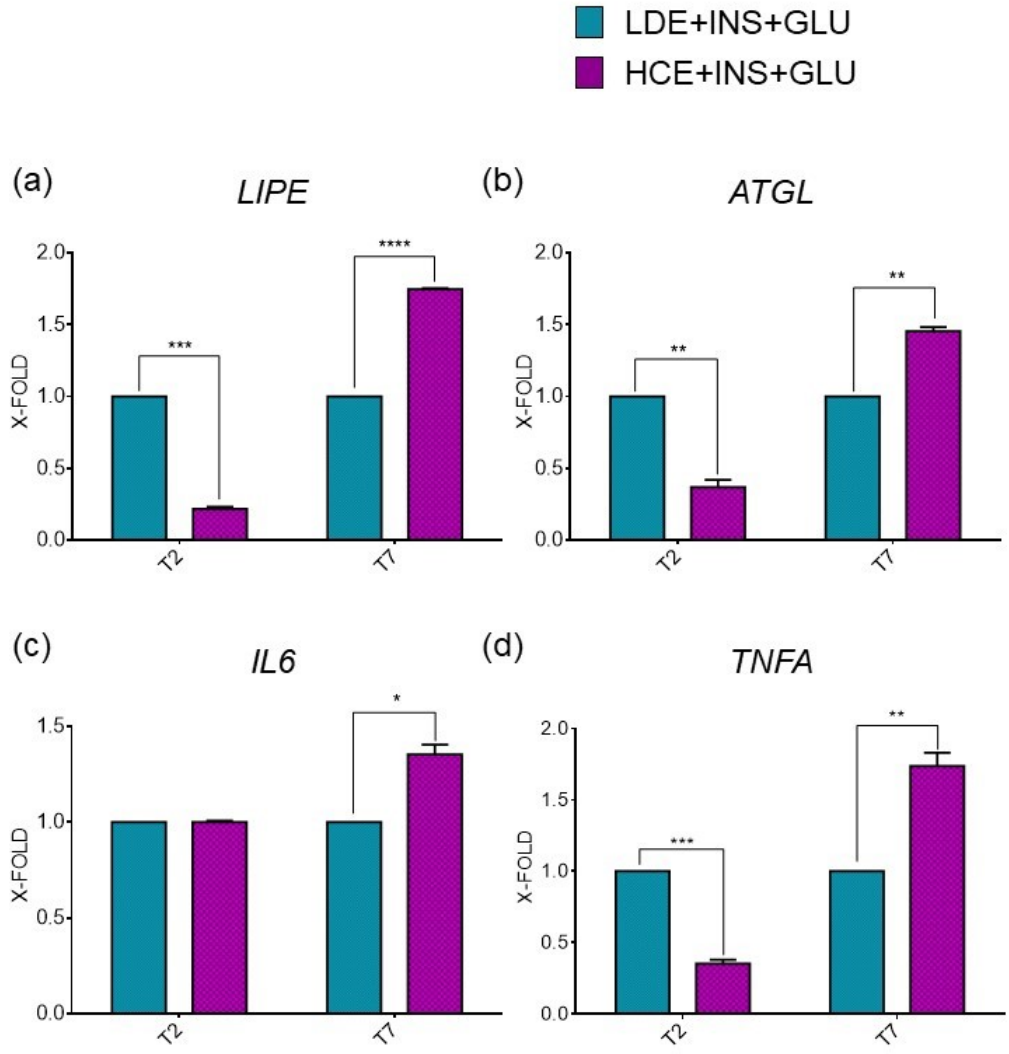

Figure 12. Gene expression in MSCs undergoing a LDE or a HCE to GCs. The bars display the expression of genes referred specifically to the development of IR: *LIPE* **(a)**, *ATGL* **(b)**, *IL6* **(c)** and *TNFA* **(d)** at T2 and T7 sampling times in MSCs isolated from abdominal skin of healthy subjects after treatments. Data are expressed as mean ± SD (over three independent experiments) of the X-FOLD (2−ΔΔCt method) of HCE+INS+GLU compared to LDE+INS+GLU arbitrarily expressed as 1, where ΔCt=Ct (gene of interest)—Ct (control gene) and Δ (ΔCt)=ΔCt (HCE+INS+GLU)—ΔCt (LDE+INS+GLU). Unpaired t-Student's test; *p < 0.05,**p < 0.01,***p < 0.001;****p < 0.0001.

4.3. TASK2

4.3.1. STEP1: Osteoclasts act differently in endogenous and exogenous CS

To investigate the capability of PBMCs to differentiate into osteoclasts, different parameters were evaluated. At first, the positivity to TRAcP, Cathepsin K and actin ring formation was analyzed. As shown in Figure 13, ENDO-PBMCs and EXO-PBMCs displayed a completely different ability to differentiate into osteoclasts compared to control PBMCs: the percentage of positive cells to osteoclastogenesis criteria was significantly higher and lower than control PBMCs in ENDO- and EXO-PBMCs respectively. No differences were noted in SS treated cells.

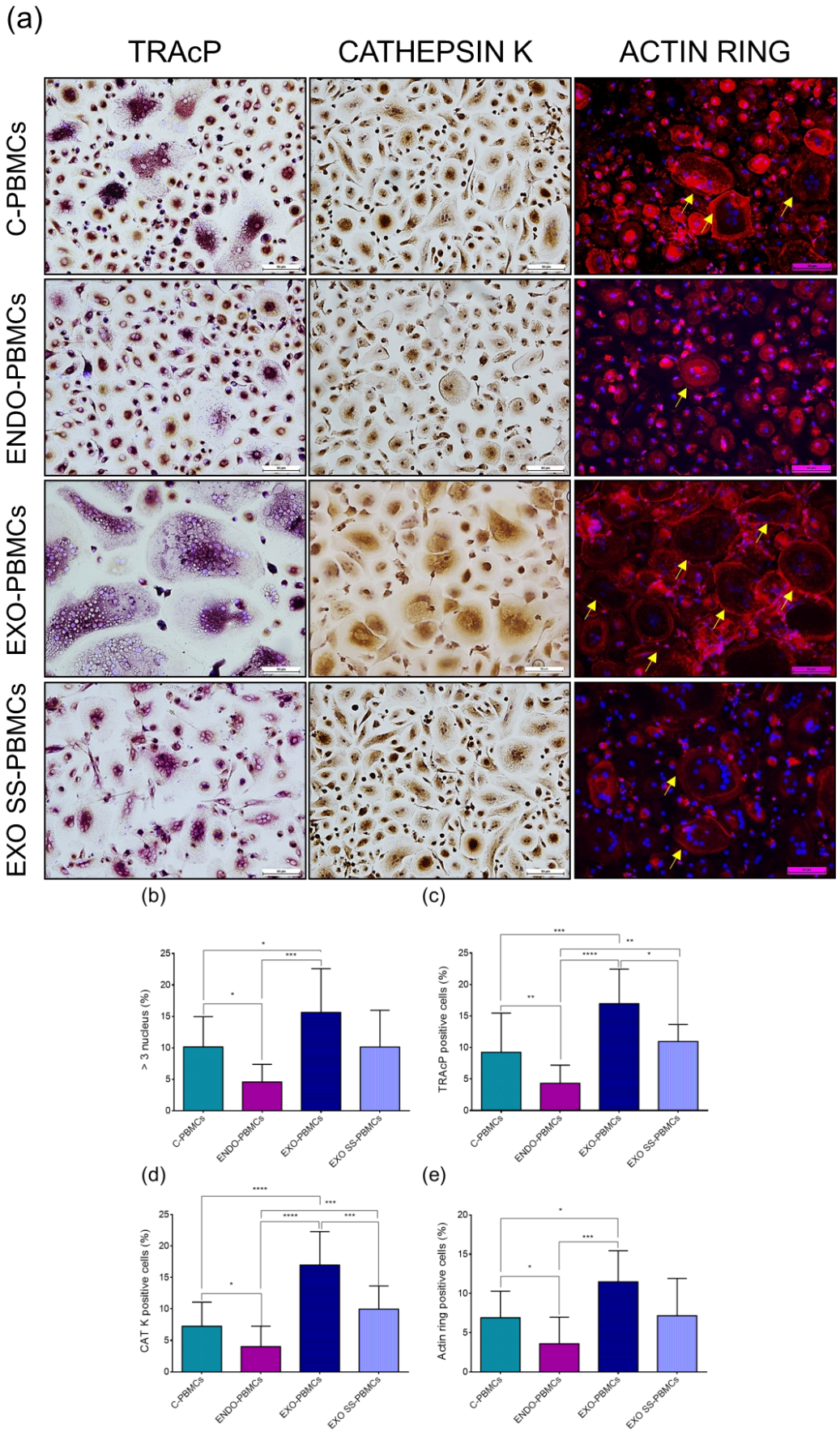
(a)
TRAcP
CATHEPSIN K
ACTIN RING
C-PBMCs
ENDO-PBMCs
EXO-PBMCs
EXO SS-PBMCs
(b)
(c)
> 3 nucleus (%)
TRAcP positive cells (%)
(d)
(e)
CAT K positive cells (%)
Actin ring positive cells (%)
C-PBMCs
ENDO-PBMCs
EXO-PBMCs
EXO SS-PBMCs

Figure 13. PBMCs differentiation capability into osteoclasts. (a) TRAcP (purple staining), Cathepsin K (DAB positivity, brown staining) and actin ring formation (indicated with yellow arrows) representative images of C-PBMCs, ENDO- PBMCs, EXO- PBMCs and EXO SS- PBMCs after 14 days of differentiations into osteoclasts (scale bar 50μm). Bars indicate the percentage of cells: with more than 3 nuclei **(b)**, positive to TRAcP **(c)**, positive to Cathepsin K **(d)** and positive to actin ring **(e)**. Data are expressed as mean ± SD of each field percentage. One-way ANOVA *p < 0.05,**p < 0.01,***p < 0.001;****p < 0.0001.

Subsequently, osteoclasts were cultured on bone slices and the realising of CTX-I and pits of resorption were analyzed. As displayed in Figure 14, the results confirmed that the area percentage of pits of resorption (b) and the amount of CTX-I (c) was definitely lower in ENDO-PBMCs but higher in EXO-PBMCs than C-PBMCs. Again, treatment with SS counterbalanced exogenous GCs effects by showing results similar to the control group.

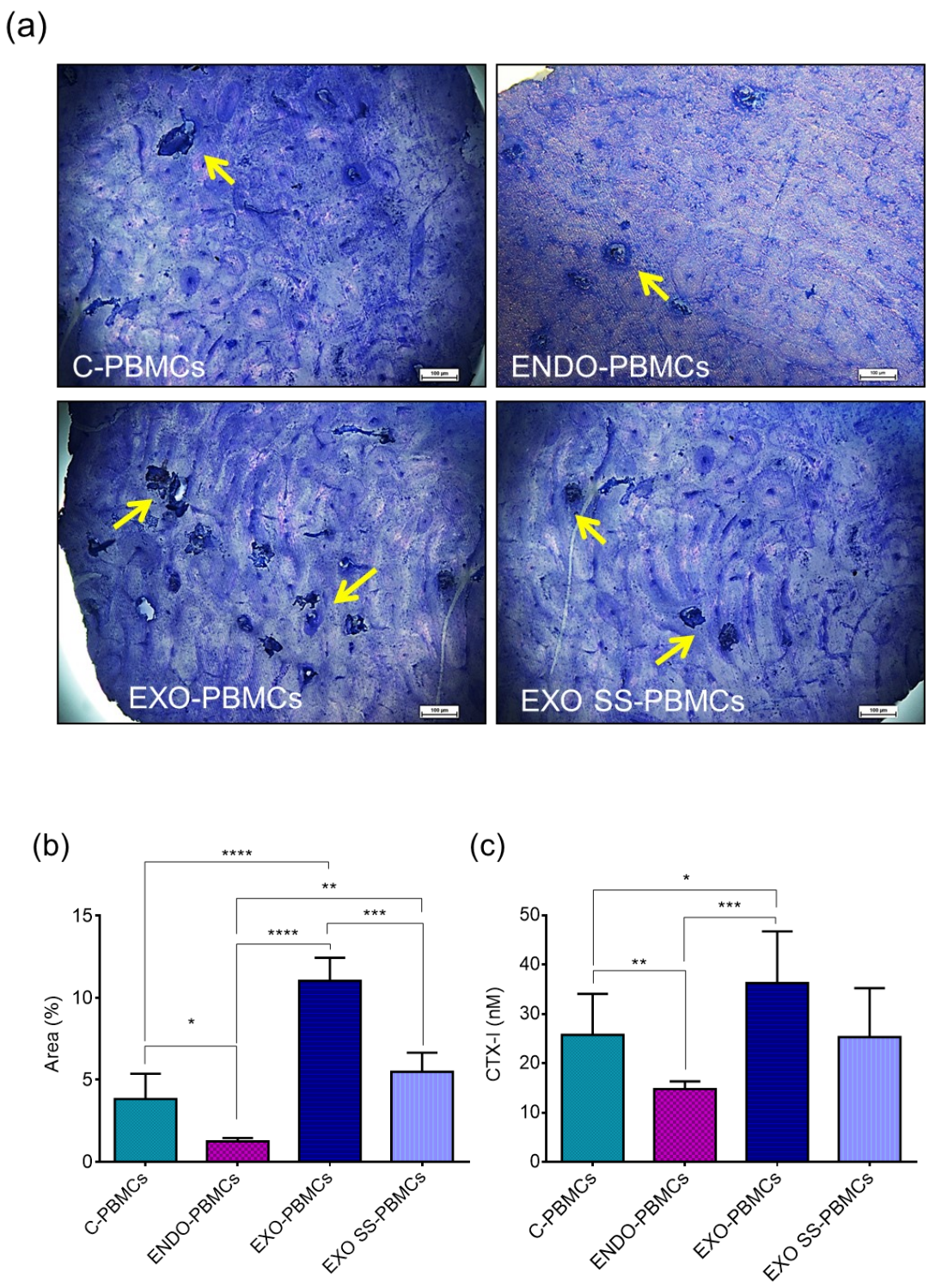

Figure 14. Osteoclasts activity. PBMCs differentiated into osteoclasts have been cultured on bone slices for 96 hours. **(a)** Coomassie Brillant Blue

staining of bone slices. Yellow arrows point resorption pits (scale bar 100μm). **(b)** Bars indicate the percentage of bone resorption area. Data are expressed as mean ± SD of each field percentage **(c)** The graph shows the CTX-I medium concentration expressed in nM. Data are expressed as mean ± SD of the analysis for CTX-I of medium collected from three independent experiments for each sample. One-way ANOVA *p < 0.05,**p < 0.01,***p < 0.001;****p < 0.0001.

4.3.2. STEP2: Differentiation into osteoblasts was impaired in both ENDO- and EXO-MSCs

Alongside the characterization of osteoclasts, the ability of MSCs to differentiate into osteoblasts was determined at first by ALP activity and mineralization analysis. At T7, the positivity to ALP staining and IF was significantly weaker in both ENDO- and EXO-MSCs differentiated cells than in control group (Figure 15). These results were also consolidated at T21, in which the amount of mineralized matrix was lower in both experimental groups than in C-MSCs. No significant differences were found during the differentiation process in EXO SS-MSCs compared to control.

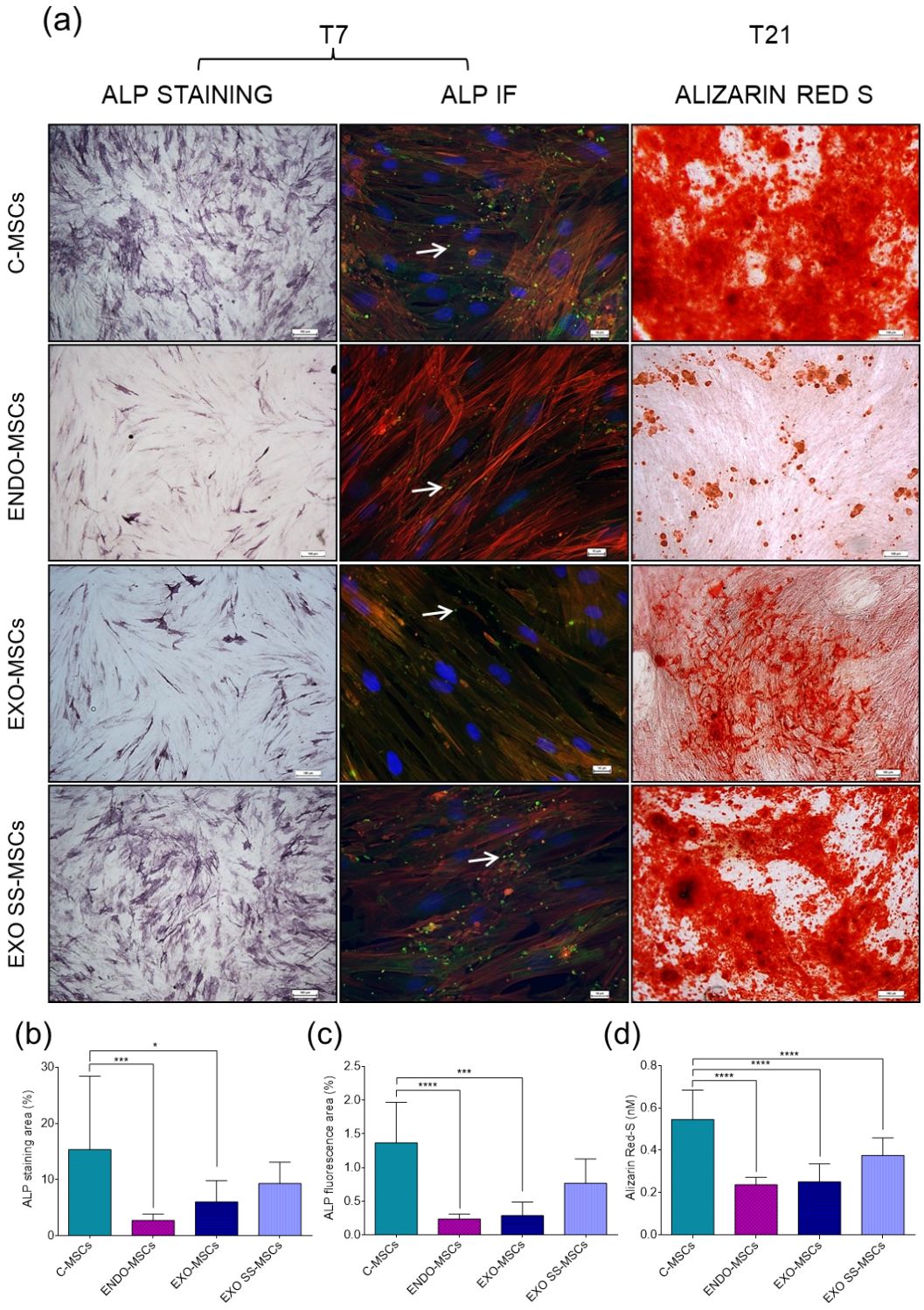

Figure 15. Ability of MSCs to differentiate into osteoblasts. (a) Representative images of ALP staining (scale bar 100µm), ALP immune-fluorescence (IF, white arrows indicate ALP vesicles, scale bar 10µm), and Alizarin Red-S (scale bar 100µm) after 7 (T7) and 21 (T21) days of

differentiation of MSCs into osteoblasts. Graphs indicate the percentage of area of positivity to ALP staining **(b)**, ALP immuno-fluorescence **(c)** and Alizarin Red-S quantification expressed in nM **(d)**. Data are expressed as mean ± SD of each field percentage for ALP and as mean ± SD of quantification analysis for Alizarin Red S. One-way ANOVA *p < 0.05,**p < 0.01,***p < 0.001;****p < 0.0001.

Collagen deposition was analysed by cellular Sirius Red staining. As represented in Figure 16, both ENDO- and EXO-MSCs secreted minor amount of collagen compared to control group and EXO SS-MSCs.

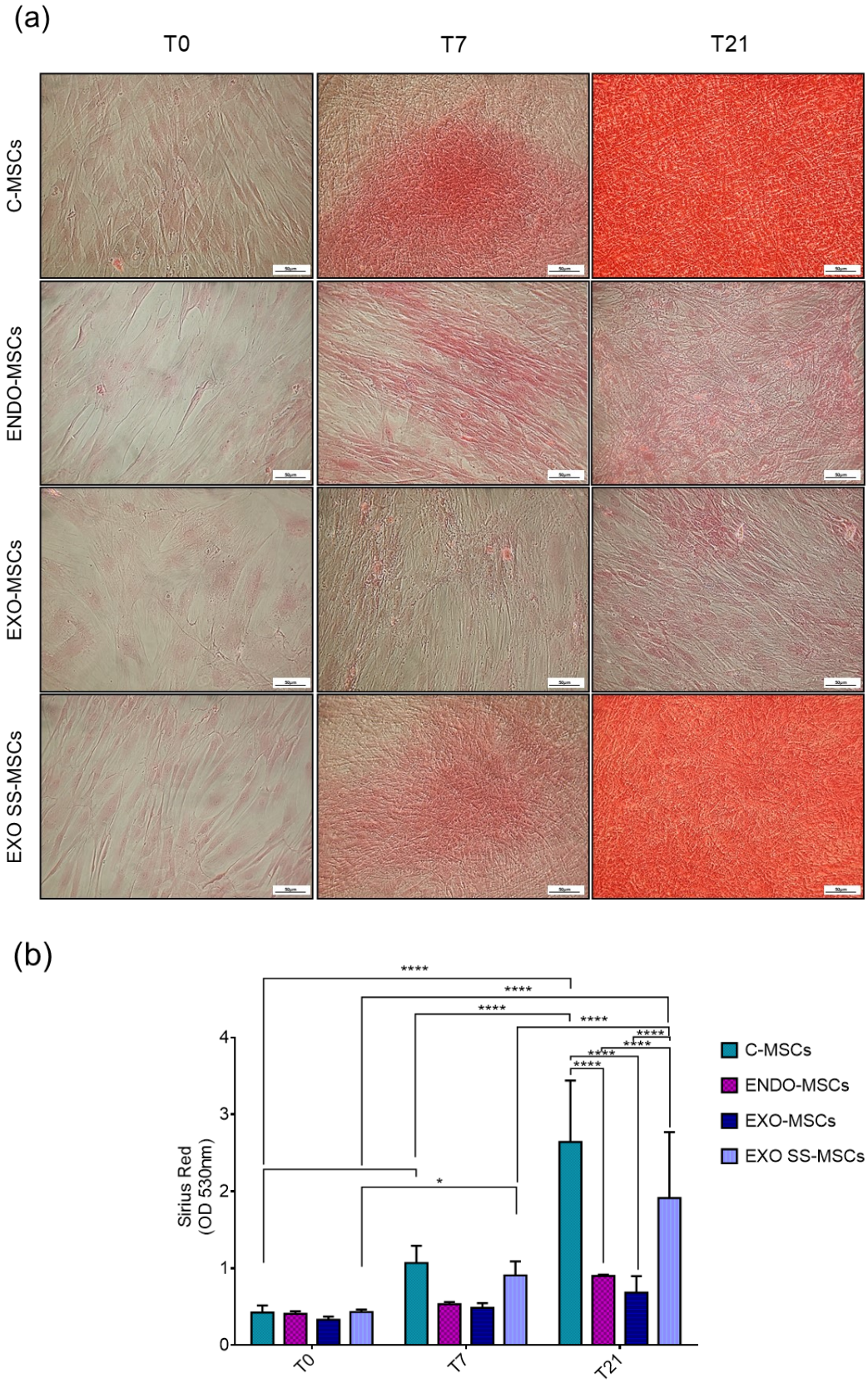

Figure 16. Collagen deposition. (a) Representative images of Sirius Red staining before (T0) and after 7 (T7) and 21 (T21) days of differentiation of

MSCs into osteoblasts (scale bar 50μm). **(b)** Sirius Red quantification. Data are expressed as mean ± SD of the OD detected in three independent experiments. Two-way ANOVA *p < 0.05,**p < 0.01,***p < 0.001;****p < 0.0001.

In addition, gene expression and protein quantification related to osteoblasts differentiation were investigated over time (T0, T7 and T21). As expected, in C-MSCs the expression of genes involved in the earlier stages of differentiation, *RUNX2* and *ALPL,* reached the highest level at T7 and then gradually decreased (T21), while the tardive stages genes, such as *SPARC* and *BGLAP*, got the peak of expression at T21. The same behaviour was observed for EXO SS-MSCs. Unlikely, both ENDO- and EXO-MSCs presented a tardive or less effective increase of these genes: high expression levels of *RUNX2* and *ALPL* were detected only at T21 while *SPARC* and *BGLAP* did not reach statistically significant level even at T21. About collagen, two different types were analyzed. At T0, *COL1A1* was strongly expressed only by C- and SS-MSCs and, during the differentiation, a decrease of its expression was observed; on the other hand, a constant increase of *COL3A1* was detected over the time in all the groups, even if more evident for C- and SS-MSCs (Figure 17).

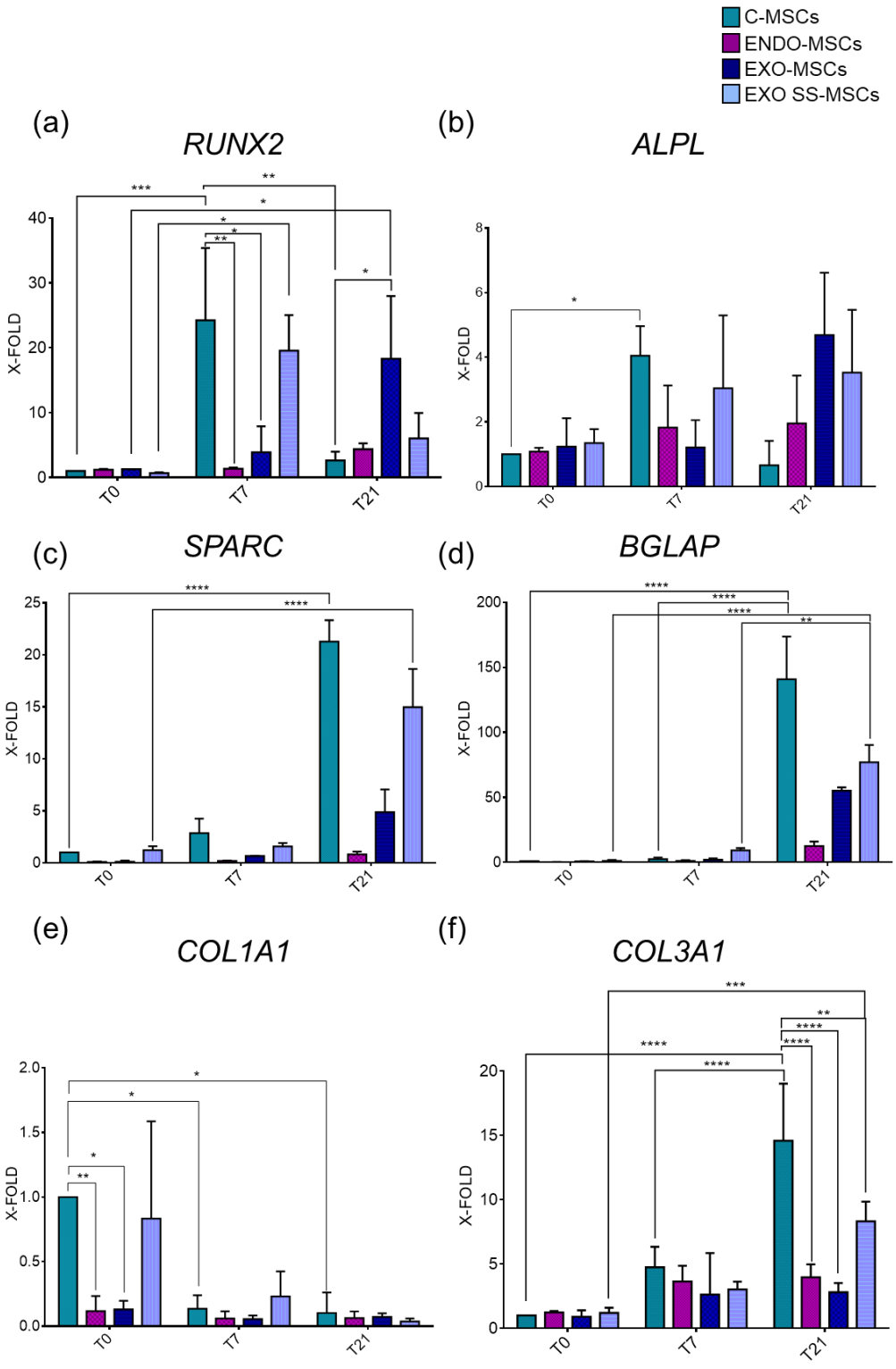

Figure 17. Osteoblastogenesis gene expression. The bars display the expression of genes referred specifically to the early (*RUNX2*, **(a)**, *ALPL* **(b)**, *COL1A1* **(e)**) and tardive (*SPARC* **(c)**, *BGLAP* **(d)**, *COL3A1* **(f)**) steps of

osteoblastogenesis, at the beginning (T0) and after 7 (T7) and 21 (T21) days of differentiation. Data are expressed as mean ± SD (over three independent experiments) of the X-FOLD ($2^{-\Delta\Delta Ct}$ method) of C-MSCs, ENDO-MSCs, EXO-MSCs and EXO SS-MSCs at different time point compared to C-MSCs at T0 arbitrarily expressed as 1. Two-way ANOVA; *p < 0.05,**p < 0.01,***p < 0.001;****p < 0.0001.

Western blot analysis, reported in Figure 18, confirmed at protein level the observed trend for ALP, RUNX2 and COL1A1. In addition, the protein levels of RANK-L and OPG were measured, and their ratio calculated. As indicated in the graph, the ratio RANK-L/OPG was clearly higher in EXO-MSCs after 21 days of differentiation than in the other groups.

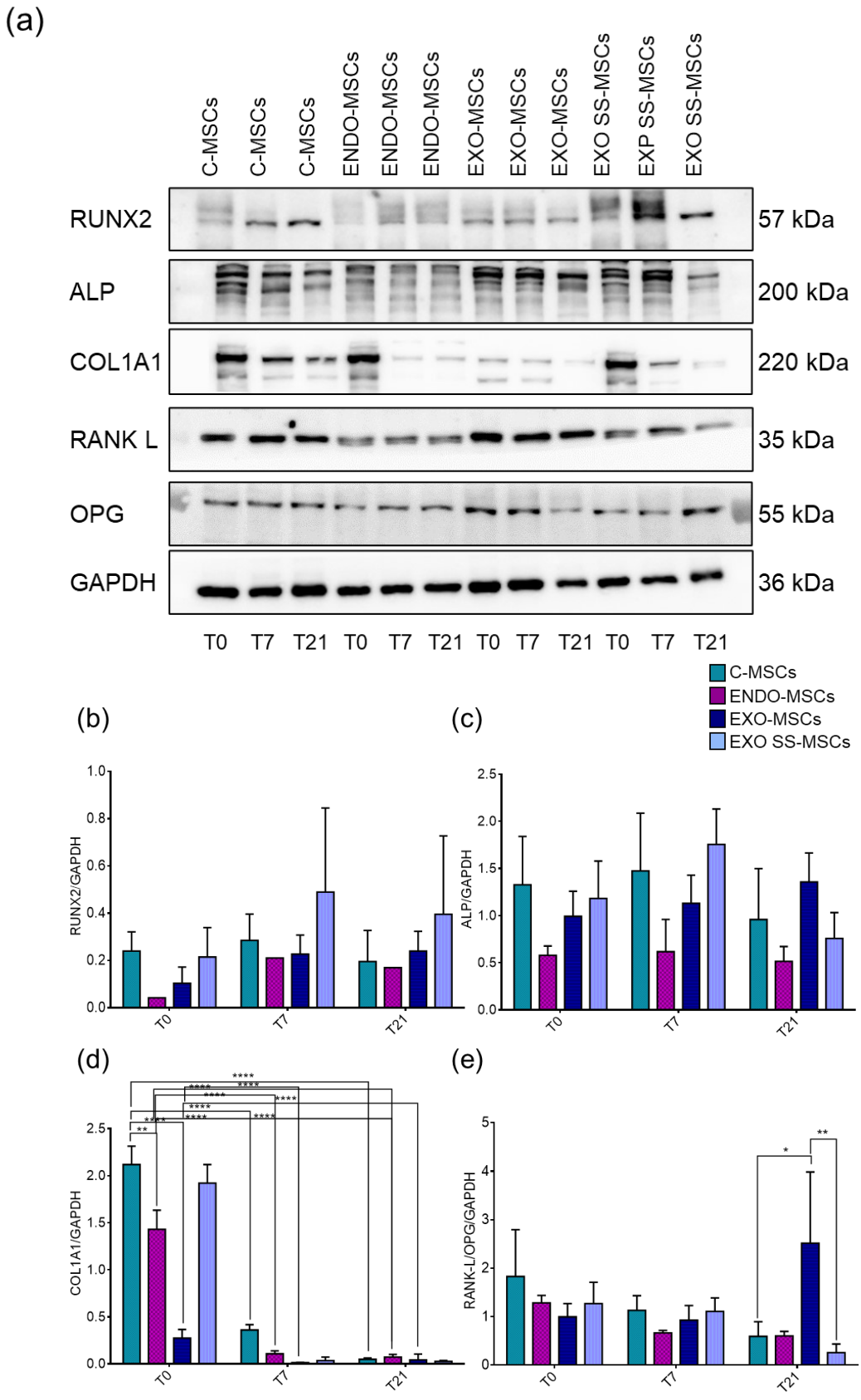
(a)
C-MSCs
C-MSCs
C-MSCs
ENDO-MSCs
ENDO-MSCs
ENDO-MSCs
EXO-MSCs
EXO-MSCs
EXO-MSCs
EXO SS-MSCs
EXP SS-MSCs
EXO SS-MSCs
RUNX2
57 kDa
ALP
200 kDa
COL1A1
220 kDa
RANK L
35 kDa
OPG
55 kDa
GAPDH
36 kDa
T0 T7 T21 T0 T7 T21 T0 T7 T21 T0 T7 T21
C-MSCs
ENDO-MSCs
EXO-MSCs
EXO SS-MSCs
(b)
RUNX2/GAPDH
(c)
ALP/GAPDH
(d)
COL1A1/GAPDH
(e)
RANK-L/OPG/GAPDH
T0
T7
T21

Figure 18. Osteoblastogenesis protein levels. **(a)** Representative images of WB analysis of RUNX2, ALP, COL1A1, RANK-L, OPG and GAPDH of C-MSCs, ENDO-MSCs, EXO-MSCs and EXO SS-MSCs at the beginning (T0) and after 7 (T7) and 21 (T21) days of differentiation. The graphs below represent the densiometric analysis referred to GAPDH of each protein **(b-e)**. Two-way ANOVA; *$p < 0.05$,**$p < 0.01$,***$p < 0.001$;****$p < 0.0001$.

4.4. TASK3

4.4.1. CS induce the fragmentation of mitochondrial network in MSCs

Mitochondrial network was investigated by confocal microscopy-based approach (Figure 19a), and parameters related to mitochondria morphology (Aspect Ratio and Form Factor) and interconnections (Branches and Branch Junctions) were analysed. The results, reported in Figure 19b-e, displayed that both ENDO- and EXO-MSCs presented small and roundish mitochondria (significantly lower Form Factor and Aspect Ratio) and a less interconnected mitochondrial network, characterized by a small number of branches and branch junctions, compared to C-MSCs and SS treated cells.

(a)

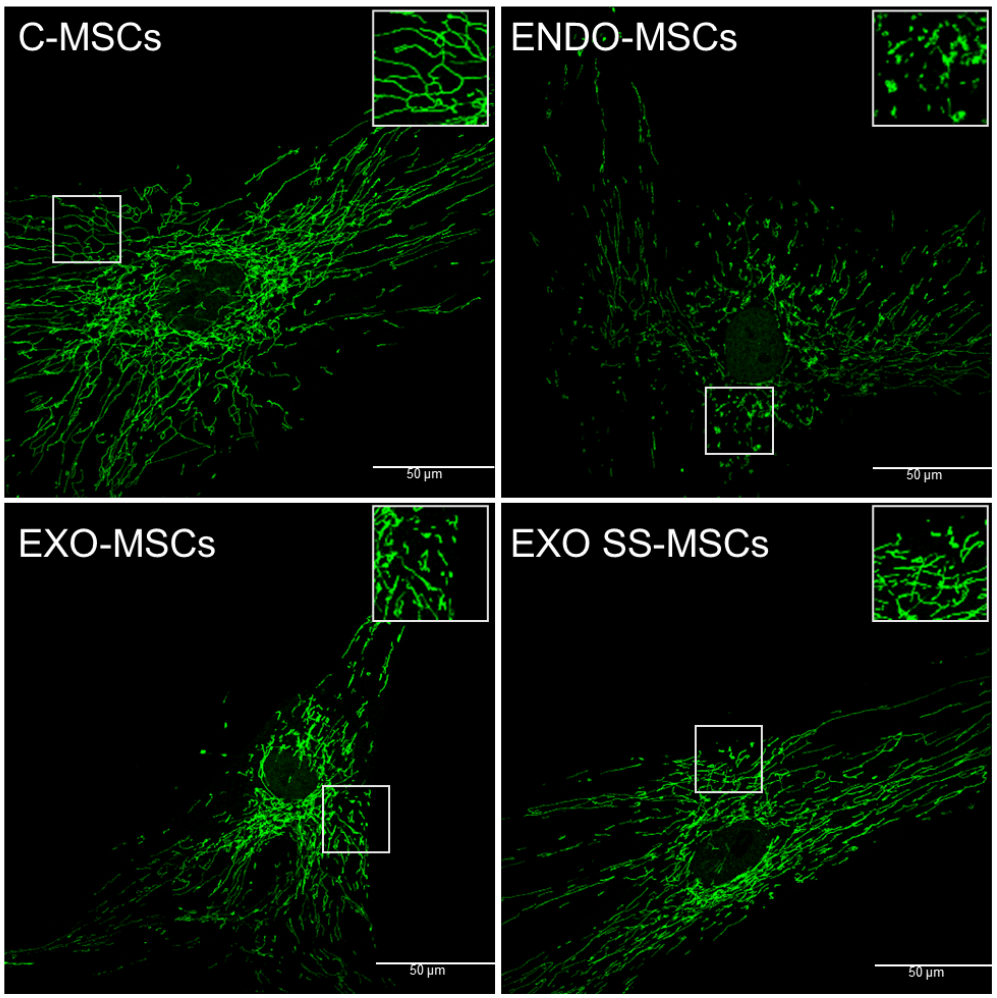
C-MSCs
ENDO-MSCs
EXO-MSCs
EXO SS-MSCs
50 µm

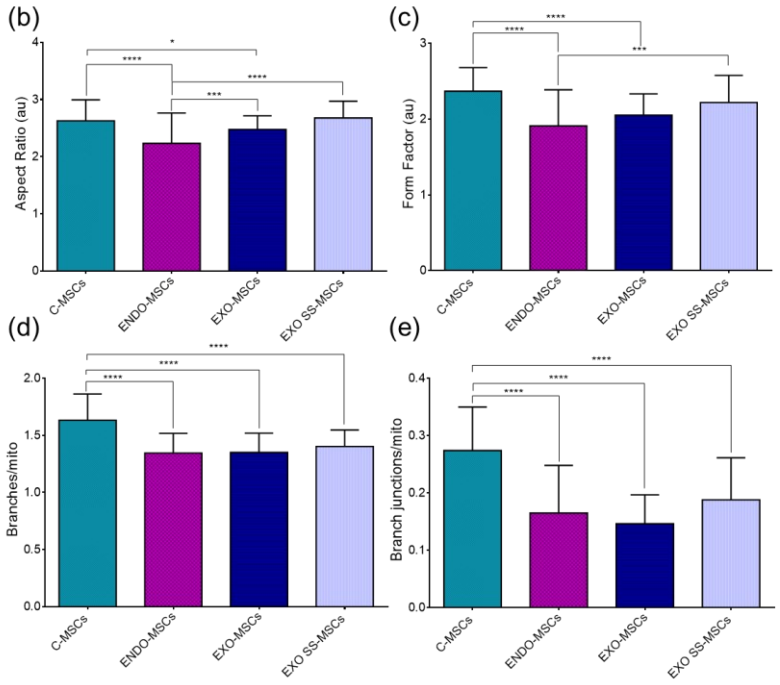
(b)
Aspect Ratio (au)
(c)
Form Factor (au)
(d)
Branches/mito
(e)
Branch junctions/mito
C-MSCs
ENDO-MSCs
EXO-MSCs
EXO SS-MSCs

Figure 19. Mitochondrial morphology. (a) Representative confocal images of mitochondrial structure of C-MSCs, ENDO-MSCs, EXO-MSCs and EXO SS-MSCs (scale bar 50µm). In the upper inset an enlargement of a mitochondria portion. **(b, c)** Analysis of mitochondria morphology (Aspect Ratio and Form Factor) and mitochondrial network **(d, e)** (Branches and Branch Junctions) of C-MSCs ENDO-MSCs, EXO-MSCs and EXO SS-MSCs. Data are expressed as mean ± SD of the analysis of 30 cells for each experimental group. One-way ANOVA; *p < 0.05, ***p < 0,001, ****p<0,0001.

4.4.2. ENDO- and EXO-MSCs produce elevated amounts of ROS

To investigate mitochondrial alterations in CS, the production of cellular (Figure 20a) and mitochondrial (Figure 20b) ROS was evaluated in MSCs by fluorescence analysis. Cellular and mitochondrial ROS production was greater in both ENDO- and EXO-MSCs than in C-MSCs. No differences were detected in SS treatments referred to control group.

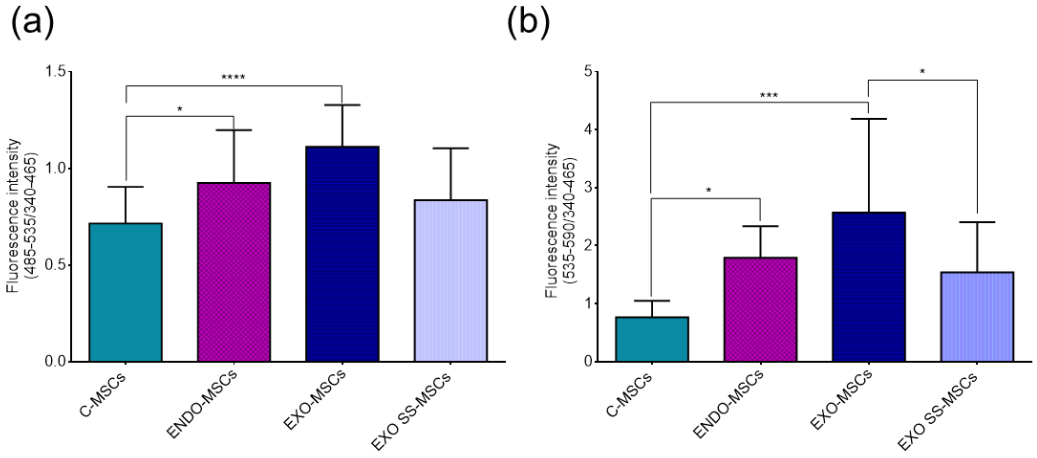

Figure 20. Cellular and mitochondrial ROS production. (a) Cellular ROS production of C-MSCs, ENDO-MSCs, EXO-MSCs and EXO SS-MSCs

detected by CM-H2DCFDA assay. Bars indicate the fluorescence intensity ratio between CM-H2DCFDA (485-535nm) and DAPI (340-465nm). **(b)** Mitochondrial ROS production of C-MSCs, ENDO-MSCs, EXO-MSCs and EXO SS-MSCs detected by MitoSOX Red assay. Bars point the fluorescence intensity ratio between MitoSOX Red (535-590nm) and DAPI (340-465nm). Data are expressed as the mean ± SD of three independent experiments. One-way ANOVA; *p < 0.05, ***p < 0,001, ****p<0,0001.

4.4.3. ΔΨ damage in ENDO- and EXO MSCs

Healthy mitochondrial membranes maintain a difference in electrical potential between the interior and exterior of the organelle, referred to as a ΔΨ. ΔΨ was measured with TMRM and a significant reduction of TMRM signal was delectated in both ENDO- and EXO-MSCs, indicating a loss of ΔΨ in Cushing groups (Figure 21), compared to C-MSCs and SS-MSCs.

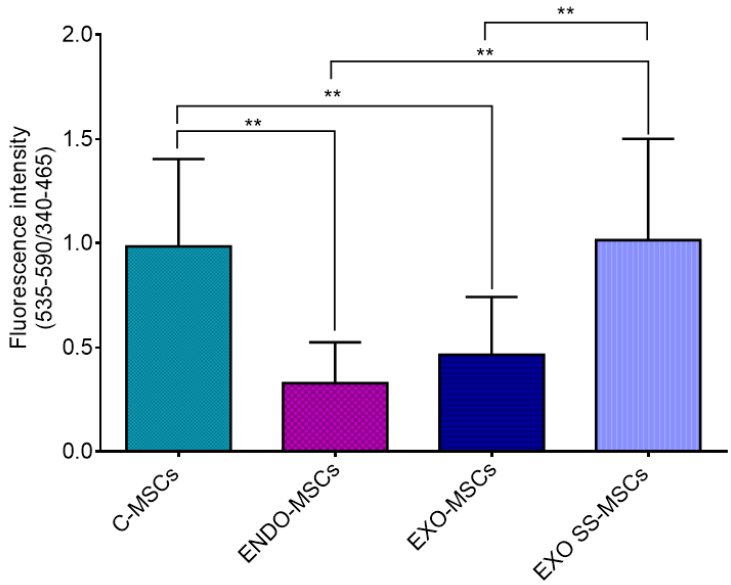

Figure 21. Mitochondrial membrane potential. ΔΨ of C-MSCs, ENDO-MSCs, EXO-MSCs and EXO SS-MSCs detected by TMRM assay. Bars report the fluorescence intensity ratio between TMRM (535-590nm) and DAPI (340-465nm). Data are expressed as the mean ± SD of three

independent experiments. One-way ANOVA; *p < 0.05, ***p < 0,001, ****p<0,0001.

4.4.4. ATP production deficiency in Cushing MSCs

ATP is required for major reaction and processes, and it plays a key role in inflammation and disease conditions. The efficiency of ATP production by mitochondria was evaluated by using a luciferase probe and stimulated with Bradykinin. Both ENDO- and EXO MSCs showed reduced mitochondrial ATP production compared to control group and EXO SS-MSCs, designating a critical dysfunction in cellular metabolism of Cushing patients (Figure 22).

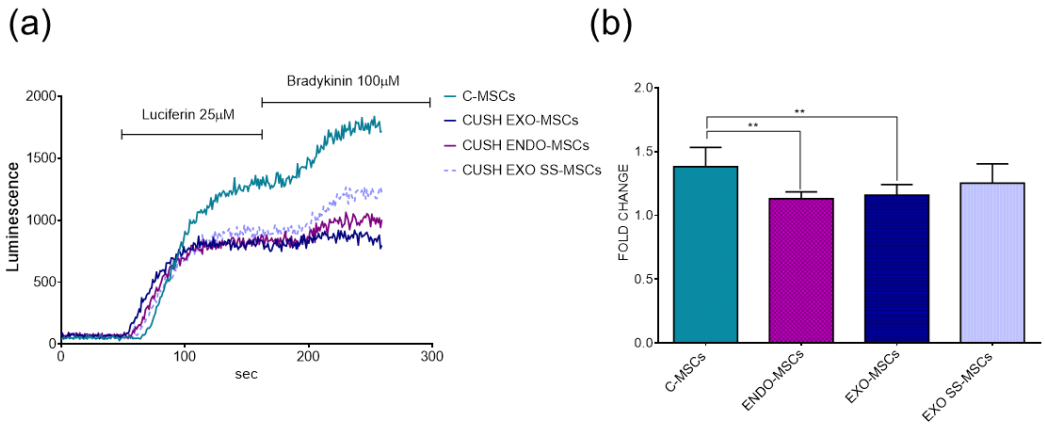

Figure 22. Mitochondrial ATP production. (a) ATP kinetic in mitochondrial compartments. The graph shows the luminescence background levels (from 0 to 60 sec), basal ATP levels (from 60 to 210 sec) and Bradykinin stimulated ATP production (from 210 to 300 sec) in living cells by using luciferin. **(b)** Mitochondrial ATP production. The bars indicate the fold change between the average of Bradykinin stimulated ATP production luminescence and basal ATP levels luminescence. Data are expressed as the mean ± SD of three independent experiments. One-way ANOVA; **p < 0,01.

5. DISCUSSION

As precursors of specialized cells compromised in CS, MSCs deserve particular interest. Their involvement has already been hypothesized [95,115] and in a previous study it has been showed that MSCs isolated from the skin biopsies of CS patients displayed dysregulated inflammatory markers and altered expression of genes related to wound healing, demonstrating not only how they could be a useful cellular model to study these events but also their potential contribution to the development of CS manifestations. With these premises, the aim of this thesis was to evaluate the involvement of MSCs in the onset and development of CS comorbidities.

5.1. TASK1

Despite the clinical aspects are well established in CS, the molecular mechanisms leading to the onset of IR are not yet fully understood. This task was developed to test a new *in vitro* method for the evaluation of the effects of chronic excess of GCs on the glucose uptake and lipids metabolism in MSCs. First, MSCs were isolated from abdominal skin of healthy subjects and characterized[5]. To reproduce daily variations of GCs levels and the food intake, cells were treated following a multi-step protocol (Figure 1). To date it is known that insulin stimulation promotes glucose uptake in adipocytes and skeletal muscle cells by GLUT-4 translocation [116–120], but the same mechanisms have not yet been demonstrated in MSCs. Therefore, before testing the potential effect of GCs, the response to insulin stimulations and GLUT-4 translocation in MSCs were analysed. These studies proved that the exposure to insulin increased the glucose uptake in MSCs via GLUT-4 translocation with mechanisms that are similar to those described for adipocytes and muscle cells [119,120]. In contrast to the cytoplasmatic localization of GLUT-4 in adipocytes cells, in MSCs it was found in perinuclear and nuclear compartments as it has already been shown in mouse embryonic stem cells [121]. As in adipocytes, the protein translocated on the

cell surface, favouring glucose uptake after insulin stimulation. Established the insulin sensitivity of MSCs, cells were exposed to different concentrations of GCs resembling the physiological (LDE) or the pathological (HCE) condition during the day. In LDE condition, insulin stimulation always led to an increased glucose uptake in MSCs, confirming that the daily reproduction of physiological levels of GCs did not alter the insulin sensitivity. Otherwise, HCE treatments impaired insulin response with a decreased glucose uptake. These observations were strengthened by confocal data that confirmed HCE conditions blocked the insulin-induced GLUT-4 translocation on cell surface. Notably, the reduction in glucose uptake was not detected in the short period (T1, T2), but observed from T3 sampling time. These results suggested that the development of IR was not immediate, but it developed over time in line with previous findings in healthy volunteers who were administered hydrocortisone at two different time points, in the evening and in the morning. Endogenous cortisol production was suppressed in volunteers by metyrapone, and nutrient intake was controlled by a continuous glucose infusion. The subjects that received hydrocortisone in the evening showed a more pronounced delayed hyperglycaemic effects than those had hydrocortisone in the morning [122]. IR development after chronic exposure to high levels of GCs has already been demonstrated in differentiated cells such as adipocytes, hepatocytes, muscle, and endothelial cells [123–125] but this has never been observed before in human stem cells. These results are in line with Gathercole et al. [126], who reported an increase of glucose uptake in a human immortalized subcutaneous adipocyte line (Chub-S7) after acute exposure to dexamethasone (up to 48 hours, in a dose- and time-dependent manner for the latter), thus proposing that the development of GC-induced obesity was promoted by enhanced adipocyte differentiation. However, it must be noted that although Chub-S7 are not fully differentiated adipocytes, they can not be considered MSCs. The link between IR and lipolysis is bidirectional: insulin

leads to an inhibition of lipolysis [127], but at the same time high levels of FFA promote the impairment of insulin sensitivity [128–130]. This possible mechanism has been evaluated and the expression of genes related to lipolysis and IR (*LIPE*, *ATGL*, *IL6* and *TNFA*) were analysed in two different time points (T2 and T7). The expression of *LIPE* and *ATGL* was initially reduced in cells under HCE conditions (T2), followed by a significant increase at T7. In literature there are conflicting data regarding the expression of *LIPE* and *ATGL*. In fact, an upregulation of them in subcutaneous adipose tissue has been demonstrated, with a higher synthesis of FFA that are released into blood to reach the liver where lipogenesis takes place [131]. In addition, high levels of FFA alter the IRS-1 phosphorylation thus causing IR at the peripheral level [132,133]. On the other hand, other studies showed a downregulation of lipase in adipose tissue, resulting in greater accumulation of triglycerides and development of obesity [134]. These results therefore demonstrated that in MSCs acute exposure to GCs leads to an initial inhibition of lipases and the development of IR is not yet consolidated as insulin still enters the cell. Conversely, chronic exposure to high levels of GCs caused a markedly significant increase in *ATGL* and *LIPE* expression, with a consequent probable synthesis of FFA and consolidation of IR. As a further confirmation, a significant overexpression of *TNFA* and *IL6*, both involved in the early stages of development of IR and type 2 diabetes mellitus [135]. The effects of pro- and anti-inflammatory cytokines such as TNF-α, IL-6 and C-reactive protein (CRP) have been highlighted in insulin signalling pathways in Pancreatic β cells and in activated macrophages where they are involved in the development of insulin resistance by inhibiting phosphorylation of IRS1 and AKT substrate 160 [136]. In summary, the development of IR in MSCs following chronic exposure to GCs is not immediate, but it develops over time, and it is consolidated by the increase of lipases and interleukins. In this line, MSCs may play a pivotal role in the development of peripheral IR in CS -with consequences on alteration of

carbohydrate and lipids metabolism- and may represent a new model to study CS *in vitro*.

5.2. TASK2

The prevalence of osteoporosis due to GCs excess has been reported to be 50–59% [137,138]in Cushing patients, which present high risk of fractures after minimal or no antecedent injury. Osteoporosis is in general caused by an imbalance between osteoblasts and osteoclasts activity but the comprehension of the underlying molecular mechanisms in CS needs further evaluations. To clarify the role of both cell types in CS osteoporosis, differentiation of MSCs and PBMCs into osteoblasts and osteoclasts respectively was evaluated. First, PBMCs and MSCs were isolated from blood samples and skin biopsies of healthy subjects (C-PBMCs/C-MSCs) and Cushing patients. Cushing patients were divided into subgroups: endogenous (ENDO-PBMCs/ENDO-MSCs), exogenous (EXO-PBMCs/EXO-MSCs) and steroid sparing treated (EXO SS-PBMCs/EXO SS-MSCs). PBMCs were induced to differentiate into osteoclasts and, after 14 days, parameters related to differentiation were evaluated. At the same time, MSCs were first characterized according to Dominici's criteria, confirming their stemness statement [5]. Subsequently, MSCs were induced to differentiate into osteoblasts and their differentiation was monitored at the beginning (T0) and after 7 (T7) and 21 (T21) days of differentiation. The results showed that ENDO-PBMCs had a poor differentiation capacity, characterized by a weak positivity to TRAcP. TRAcP is glycosylated monomeric metalloprotein enzyme responsible of osteoclasts migration to bone resorption sites. Once there, TRAcP improves osteoclasts differentiation, activation, and proliferation. At the same time, it was demonstrated that in TRAcP knockout mice model, bone formation occurred in a haphazard manner and the microarchitecture was highly irregular [139]. A cytoskeleton reorganization with the formation of actin ring is also essential for osteoclast function. It should be noted that bone resorption occurs only when the closure zone is formed and enzymes like Cathepsin K

are released [140]. However, the deficit in osteoclast differentiation of ENDO-PBMCs resulted in an irregular structure of cytoskeleton and a faint positivity to Cathepsin K; this led to a poor bone resorption capacity, confirmed by the lower quantity of CTX-I produced. On the other hand, EXO-PBMCs demonstrated a greater ability to differentiate into osteoclasts than C- and ENDO-PBMCs, characterized by higher number of osteoclasts, increased positivity to TRAcP and Cathepsin K, improved actin ring formation, enhanced bone resorption with higher amount of CTX-I. Conversely, results on osteoblasts differentiation demonstrated that both ENDO- and EXO-MSCs differentiated more slowly than the control group. In detail, ALP activity, mineralization and collagen deposition were lower in both ENDO- and EXO-MSCs than in the control group. Interestingly, the analysis of genes related to osteoblasts differentiation showed that genes involved in the earlier stages, such as *RUNX2* and *ALPL*, showed maximum expression at T7 and decreased at T21 in C-MSCs, to be replaced by the expression of later genes, such us *SPARC* and *BGLAP*, which reach maximum expression at T21. At the same time, although the amount of deposited collagen increased over the time in C-MSCs, the expression of *COL1A1*, involved in the earlier process of proliferation, collapsed during differentiation, and was replaced by a gradual increase of *COL3A1*, which is responsible for the ECM maturation and mineralization [141]. Concurrently, ENDO- and EXO-MSCs showed a tardive increase in *RUNX2* and *ALPL*, that were overexpressed at T21. These results are in line with previous studies demonstrating that GCs affected the expression of PPAR-γ2, KLF15, C/EBPα and aP2. This gene dysregulation led to the preferential differentiation of pluripotent precursor cells into adipocytes over osteoblasts, with a reduction of osteoblastogenesis and consequent bone loss [142,143]. Furthermore, in line with the lower collagen deposition, it has been already demonstrated that GCs increased the synthesis of interstitial collagenase, responsible of Collagen I degradation by post-transcriptional mechanisms

[144]. The analysis of RANK-L/OPG ratio revealed that, despite the poor differentiation capacity of ENDO- and EXO-MSCs, at T21 the ratio was definitely higher in EXO-MSCs than in ENDO-MSCs. Different studies demonstrated that RANK-L/OPG signalling pathway is also affected by GCs. In osteoblasts and osteocytes, GCs increase the production of RANKL, and decrease OPG mRNA transcription [145–147]. The increase of RANK-L/OPG ratio results in enhanced bone resorption by promoting differentiation and maturation of osteoclasts as it could be observed in EXO-PBMCs but not in ENDO-PBMC. The reason of this apparent contradiction may lay on the time of the disease onset. More precisely, dating the onset of endogenous CS is not easy, and the time between the appearance of the first symptoms and the diagnosis could be quite long. On the contrary, exogenous CS onset is quite straightforward to identify. Therefore, it is probable that endogenous Cushing patients enrolled in this study were under long-term effects of GCs. The long-term effects of GCs on osteoclast function are less clear and several studies suggest that GCs can disrupt the osteoclast cytoskeleton leading to depressed osteoclast activity [148–150]. In addition, the effects of glucocorticoid sparing drugs were assessed. Steroid sparing therapies are additional non-glucocorticoid drugs, administered with the aim of partially reducing the adverse effects of GCs. In line with this role, EXO SS-PBMCs presented a differentiation capacity similar to control group, indicating that the use of steroid sparing drugs is useful to prevent collateral effects of GCs excess. In conclusion, the detrimental effects of GCs on MSCs promote osteoporosis through complex, and partially different, mechanisms in exogenous and endogenous CS. The imbalance between osteoblasts and osteoclasts is rooted in the exposure time to GCs. While osteoblastogenesis is negatively affected already from the early stages of the disease and persists overtime, as it has been demonstrated in both EXO- and ENDO-MSCs, osteoclastogenesis and bone resorption activity of the osteoclasts seem to pilot osteoporosis mainly during the first phases of the disorder as revealed

in EXO-MSCs, but not in ENDO-MSCs, where prolonged GCs exposure damage osteoclasts activity. As a result, the deficiency of MSCs to differentiate in presence of elevated concentration of GCs affects the impaired bone homeostasis and the disruption of bone microarchitecture, promoting osteoporosis in CS. The study of mechanisms that underline the molecular pathways weaken in Cushing MSCs may be cardinal to find new more targeted therapy.

5.3. TASK 3

A great percentage of Cushing patients develops dysfunctions in glucose metabolism resulting in an increased risk of metabolic syndrome and cardiovascular damage. Glucose metabolism is regulated by different and articulate biochemical mechanisms that include the ability of insulin to regulate glucose concentrations in the blood by enhancing its uptake in peripheral tissues, suppressing lipolysis, and decreasing gluconeogenesis. High levels of GCs stimulate lipolysis and increase FFA, which inhibit IRS-1 phosphorylation and induce IR and type 2 diabetes issues, prominent features of CS [151–154]. Glucose and FFA are metabolized inside mitochondria through citric acid cycle and beta oxidation respectively. Glucose and FFA chemical bonds release their energy that is captured by NAD and Flavin adenine dinucleotide (FAD) which are then reduced to NADH and FADH2 and donate these high energy electrons to the electron transport chain (ECT), located in the inner mitochondria membrane (IMM). The electrons move along this chain ad free energy is used to produce ATP. This process is called oxidative phosphorylation (OXPHOS) and more than 90% of total cellular ATP is generate in mitochondria. Being at the centre of energy metabolism, it's obvious to associate mitochondria to metabolic syndrome. A sufficient ATP concentration is not only determined by expression levels of enzymatic complexes involved in OXPHOS, but also by mitochondria morphology and function [155]. It has been demonstrated that mitochondrial dysfunctions may lead to IR in pancreas, skeletal muscle, fat, and liver [89–91] and the excess of GCs affects mitochondrial metabolism in various tissues and in time-dependent manner [156–158]. It was reported that three days of DEX injections increased cytochrome c oxidase activity in rat skeletal muscles [156]. At the same time, one-day administration of high doses of GCs stimulated mitochondrial oxidation in cortical neurons, but long-term treatments significantly reduced it [157]. Furthermore, a study conducted by Jezkova et al. in 2019 on SCAT of Cushing's patients proved

a dysregulation of genes encoding subunits of oxidative phosphorylation system, pyruvate dehydrogenase, and citrate synthase in mitochondria [94]. However, to date, nothing is known about the relationship between mitochondria and CS in MSCs. Assuming the hypothesis that chronic excess of GCs in CS patients may lead to mitochondrial dysfunction contributing to the development of IR, mitochondrial morphology and function were evaluated in MSCs of patients with CS. Mitochondrial function and response to stimuli are defined by their complex structure and dynamics characterized by mitochondrial fusion/fission [159], and specific mitochondrial responses are determined by a combination of interacting factors, including biochemical and metabolic cell state. In physiological conditions the frequencies of fusion and fission events are balanced but high fusion leads to elongated, tubular, interconnected mitochondrial networks, whereas high fission results in fragmented, discontinuous mitochondria. Here, ENDO- and EXO-MSCs showed a mitochondrial fragmentated phenotype. The completely lack of mitochondrial fusion could induce severe cellular defects, including poor growth, heterogeneity of mitochondrial membrane potential, and decreased respiration. At the same time mitochondrial fission is essential for mitochondrial quality control, as this process allows to remove damaged mitochondria. Mitochondrial fragmentation is also linked to an increase of ROS production that leads to oxidative stress and cellular damage and contributes to metabolic disease progression [160–162]. In line with this, elevate ROS concentrations have been found in MSCs from CS patients, both at cellular and mitochondrial levels. Mitochondria generate ROS as a byproduct of the ETC during OXPHOS, which is deeply regulated by several factors, including $\Delta\Psi$, that results compromised in both ENDO- and EXO-MSCs. Some studies proved that excessive mitochondrial fragmentation caused disruption of the IMM and cristae structure, that in turn induced alterations in ETC complexes [163–165]. The consequent electron and proton leak leads to decreased ATP production and increased ROS

production, as it has been observed in Cushing samples. At the same time, it has been demonstrated that the accumulation of FFA causes the activation of NADPH oxidase enzyme and generation of excessive ROS [166]. Increased oxidative stress damages ETC components and other mitochondrial constituents leading to mitochondrial fragmentation [167]. In fact, ROS activate Dynamin-related protein 1 (DRP1), a protein responsible for mitochondrial fission, and further drive mitochondrial fission and ROS production, creating a positive feedback loop [168,169]. As a consequence, the accumulation of damaged mitochondria could contribute to oxidative stress and inflammation in CS. Excessive ROS production also affects intracellular signalling by inhibiting tricarboxylic cycle enzyme aconitase, and thus favours citrate accumulation which is diverted to fat synthesis. Moreover, elevated levels of hydrogen peroxide (H_2O_2) in mitochondria also inhibit β fatty acid oxidation and cause an increase of FFA storage and in turn the development of IR [170].

MSCs from CS patients treated with SS showed results closer to those observed in C-MSCs for all the analysed parameters, confirming that the association of steroid sparing to GCs treatment avoids the onset of Cushing comorbidities.

Again, it is proven that MSCs displayed the same molecular alterations found in differentiated cells and that could play a role in the onset of the complex and multifactorial aetiology of CS comorbidities, including involvement of mitochondria. These preliminary results open the door to further studies on mitochondria ECT and respiration, as well as on antioxidant system, and their relationship with IR signalling pathways to better clarify mitochondrial dysfunction in CS.

6. CONCLUSION AND FUTURE PERSPECTIVES

In conclusion, the results of TASKS 1-2-3 converge in identifying the involvement of MSCs in the occurrence of CS comorbidities.

TASK 1 and 3 demonstrated how an excess of GCs leads to IR in MSCs and how these cells provide a valuable model for studying *in vitro* the effects of GCs excess in the molecular mechanisms underlying IR. Furthermore, the involvement of mitochondria in IR hypothesized for differentiated cells seems to be plausible for MSCs as well.

Regarding osteoporosis, it has been shown how the two cell populations involved are both affected by excess GCs. While osteoblasts derived from EXO and ENDO-MSCs are less efficient than osteoblasts from C-MSCs and share a similar behaviour, osteoclasts from EXO-MSCs are found to be more numerous and active than those derived from ENDO-MSCs; this difference could reside in the longer duration of excess GCs in the endogenous CS.

This thesis lays the groundwork for a more in-depth study aimed at fully understanding the molecular mechanisms already acting on MSCs that lead to the onset of CS comorbidities; if a decisive role of MSCs is confirmed, they could be used for early evaluation of the efficacy of currently used drugs as well as become the target for new, more durable therapeutic approaches.

REFERENCES

1. Shenghui H, Nakada D, Morrison SJ. Mechanisms of Stem Cell Self-Renewal. Annu Rev Cell Dev Biol. 2009;25:377–406.

2. Ambrosio C, Zomer H, Vidane A, Gonçalves N. Mesenchymal and induced pluripotent stem cells: general insights and clinical perspectives. Stem Cells Cloning. 2015;125.

3. Caplan AI. Mesenchymal stem cells. Journal of Orthopaedic Research. 1991;9:641–50.

4. Brighton CT, Hunt RM. Early histological and ultrastructural changes in medullary fracture callus. J Bone Joint Surg. 1991;73:832–47.

5. Dominici M, Le Blanc K, Mueller I, Slaper-Cortenbach I, Marini FC, Krause DS, et al. Minimal criteria for defining multipotent mesenchymal stromal cells. The International Society for Cellular Therapy position statement. Cytotherapy. 2006;8:315–7.

6. Pittenger MF, Mackay AM, Beck SC, Jaiswal RK, Douglas R, Mosca JD, et al. Multilineage Potential of Adult Human Mesenchymal Stem Cells. Science (1979). 1999;284:143–7.

7. Nombela-Arrieta C, Ritz J, Silberstein LE. The elusive nature and function of mesenchymal stem cells. Nat Rev Mol Cell Biol. 2011;12:126–31.

8. Schraufstatter IU. Mesenchymal stem cells and their microenvironment. Frontiers in Bioscience. 2011;16:2271.

9. Chao KC, Chao KF, Fu YS, Liu SH. Islet-Like Clusters Derived from Mesenchymal Stem Cells in Wharton's Jelly of the Human Umbilical Cord for Transplantation to Control Type 1 Diabetes. PLoS One. 2008;3:e1451.

10. Sasaki M, Abe R, Fujita Y, Ando S, Inokuma D, Shimizu H. Mesenchymal Stem Cells Are Recruited into Wounded Skin and Contribute

to Wound Repair by Transdifferentiation into Multiple Skin Cell Type. The Journal of Immunology. 2008;180:2581–7.

11. Jiang Y, Jahagirdar BN, Reinhardt RL, Schwartz RE, Keene CD, Ortiz-Gonzalez XR, et al. Pluripotency of mesenchymal stem cells derived from adult marrow. Nature. 2002;418:41–9.

12. Lazzarini R, Guarnieri S, Fulgenzi G, Mariggiò MA, Graciotti L, Martiniani M, et al. Mesenchymal Stem Cells from Nucleus Pulposus and Neural Differentiation Potential: a Continuous Challenge. Journal of Molecular Neuroscience. 2019;67:111–24.

13. Franco Lambert AP, Fraga Zandonai A, Bonatto D, Cantarelli Machado D, Pêgas Henriques JA. Differentiation of human adipose-derived adult stem cells into neuronal tissue: Does it work? Differentiation. 2009;77:221–8.

14. Banerjee K, Chattopadhyay A, Banerjee S. Understanding the association of stem cells in fetal development and carcinogenesis during pregnancy. Advances in Cancer Biology - Metastasis. 2022;4:100042.

15. Ren G, Zhao X, Zhang L, Zhang J, L'Huillier A, Ling W, et al. Inflammatory Cytokine-Induced Intercellular Adhesion Molecule-1 and Vascular Cell Adhesion Molecule-1 in Mesenchymal Stem Cells Are Critical for Immunosuppression. The Journal of Immunology. 2010;184:2321–8.

16. Spaggiari GM, Abdelrazik H, Becchetti F, Moretta L. MSCs inhibit monocyte-derived DC maturation and function by selectively interfering with the generation of immature DCs: central role of MSC-derived prostaglandin E2. Blood. 2009;113:6576–83.

17. Kim J, Hematti P. Mesenchymal stem cell–educated macrophages: A novel type of alternatively activated macrophages. Exp Hematol. 2009;37:1445–53.

18. Kay LJ, Yeo WW, Peachell PT. Prostaglandin E $_2$ activates EP $_2$ receptors to inhibit human lung mast cell degranulation. Br J Pharmacol. 2006;147:707–13.

19. Raffaghello L, Bianchi G, Bertolotto M, Montecucco F, Busca A, Dallegri F, et al. Human Mesenchymal Stem Cells Inhibit Neutrophil Apoptosis: A Model for Neutrophil Preservation in the Bone Marrow Niche. Stem Cells. 2008;26:151–62.

20. Glennie S, Soeiro I, Dyson PJ, Lam EW-F, Dazzi F. Bone marrow mesenchymal stem cells induce division arrest anergy of activated T cells. Blood. 2005;105:2821–7.

21. Augello A, Tasso R, Negrini S, Amateis A, Indiveri F, Cancedda R, et al. Bone marrow mesenchymal progenitor cells inhibit lymphocyte proliferation by activation of the programmed death 1 pathway. Eur J Immunol. 2005;35:1482–90.

22. Campanati A, Orciani M, Lazzarini R, Ganzetti G, Consales V, Sorgentoni G, et al. <scp>TNF</scp> -α inhibitors reduce the pathological Th $_1$ –Th $_{17}$ /Th $_2$ imbalance in cutaneous mesenchymal stem cells of psoriasis patients. Exp Dermatol. 2017;26:319–24.

23. Diotallevi F, Di Vincenzo M, Martina E, Radi G, Lariccia V, Offidani A, et al. Mesenchymal Stem Cells and Psoriasis: Systematic Review. Int J Mol Sci. 2022;23:15080.

24. Orciani M, Campanati A, Caffarini M, Ganzetti G, Consales V, Lucarini G, et al. T helper (Th)1, Th17 and Th2 imbalance in mesenchymal stem cells of adult patients with atopic dermatitis: at the origin of the problem. British Journal of Dermatology. 2017;176:1569–76.

25. Doherty DF, Roets L, Krasnodembskaya AD. The Role of Lung Resident Mesenchymal Stromal Cells in the Pathogenesis and Repair of Chronic Lung Disease. Stem Cells. 2023;41:431–43.

26. Bonifazi M, Di Vincenzo M, Caffarini M, Mei F, Salati M, Zuccatosta L, et al. How the Pathological Microenvironment Affects the Behavior of Mesenchymal Stem Cells in the Idiopathic Pulmonary Fibrosis. Int J Mol Sci. 2020;21:8140.

27. Lazzarini R, Caffarini M, Delli Carpini G, Ciavattini A, Di Primio R, Orciani M. From 2646 to 15: differentially regulated microRNAs between progenitors from normal myometrium and leiomyoma. Am J Obstet Gynecol. 2020;222:596.e1-596.e9.

28. Lightman SL, Birnie MT, Conway-Campbell BL. Dynamics of ACTH and Cortisol Secretion and Implications for Disease. Endocr Rev. 2020;41.

29. Häggström M, Richfield D. Diagram of the pathways of human steroidogenesis. WikiJournal of Medicine. 2014;1.

30. Görges R, Knappe G, Gerl H, Ventz M, Stahl F. Diagnosis of Cushing's syndrome: Re-evaluation of midnight plasma cortisol vs urinary free cortisol and low-dose dexamethasone suppression test in a large patient group. J Endocrinol Invest. 1999;22:241–9.

31. Elenkov IJ. Glucocorticoids and the Th1/Th2 balance. Ann N Y Acad Sci. 2004;1024:138–46.

32. CHYUN YS, KREAM BE, RAISZ LG. Cortisol Decreases Bone Formation by Inhibiting Periosteal Cell Proliferation*. Endocrinology. 1984;114:477–80.

33. Kuo T, McQueen A, Chen T-C, Wang J-C. Regulation of Glucose Homeostasis by Glucocorticoids. Adv Exp Med Biol. 2015;872:99–126.

34. Exton JH. Regulation of Gluconeogenesis by Glucocorticoids. 1979. p. 535–46.

35. Kraus-Friedmann N. Hormonal regulation of hepatic gluconeogenesis. Physiol Rev. 1984;64:170–259.

36. Di Dalmazi G, Pagotto U, Pasquali R, Vicennati V. Glucocorticoids and Type 2 Diabetes: From Physiology to Pathology. J Nutr Metab. 2012;2012:1–9.

37. Kuo T, Harris CA, Wang J-C. Metabolic functions of glucocorticoid receptor in skeletal muscle. Mol Cell Endocrinol. 2013;380:79–88.

38. Coderre L, Srivastava AK, Chiasson JL. Role of glucocorticoid in the regulation of glycogen metabolism in skeletal muscle. Am J Physiol. 1991;260:E927-32.

39. Wang J-C, Gray NE, Kuo T, Harris CA. Regulation of triglyceride metabolism by glucocorticoid receptor. Cell Biosci. 2012;2:19.

40. Jaworski K, Sarkadi-Nagy E, Duncan RE, Ahmadian M, Sul HS. Regulation of Triglyceride Metabolism.IV. Hormonal regulation of lipolysis in adipose tissue. American Journal of Physiology-Gastrointestinal and Liver Physiology. 2007;293:G1–4.

41. Gathercole LL, Morgan SA, Bujalska IJ, Hauton D, Stewart PM, Tomlinson JW. Regulation of Lipogenesis by Glucocorticoids and Insulin in Human Adipose Tissue. PLoS One. 2011;6:e26223.

42. Lee S, Krüger BT, Ignatius A, Tuckermann J. Distinct Glucocorticoid Receptor Actions in Bone Homeostasis and Bone Diseases. Front Endocrinol (Lausanne). 2022;12.

43. Arnaldi G, Scandali VM, Trementino L, Cardinaletti M, Appolloni G, Boscaro M. Pathophysiology of Dyslipidemia in Cushing's Syndrome. Neuroendocrinology. 2010;92:86–90.

44. Czech MP. Mechanisms of insulin resistance related to white, beige, and brown adipocytes. Mol Metab. 2020;34:27–42.

45. Hazlehurst JM, Gathercole LL, Nasiri M, Armstrong MJ, Borrows S, Yu J, et al. Glucocorticoids Fail to Cause Insulin Resistance in Human Subcutaneous Adipose Tissue In Vivo. J Clin Endocrinol Metab. 2013;98:1631–40.

46. Lee M-J, Pramyothin P, Karastergiou K, Fried SK. Deconstructing the roles of glucocorticoids in adipose tissue biology and the development of central obesity. Biochimica et Biophysica Acta (BBA) - Molecular Basis of Disease. 2014;1842:473–81.

47. Dalle H, Garcia M, Antoine B, Boehm V, Do TTH, Buyse M, et al. Adipocyte Glucocorticoid Receptor Deficiency Promotes Adipose Tissue Expandability and Improves the Metabolic Profile Under Corticosterone Exposure. Diabetes. 2019;68:305–17.

48. Chimin P, Farias T da SM, Torres-Leal FL, Bolsoni-Lopes A, Campaña AB, Andreotti S, et al. Chronic glucocorticoid treatment enhances lipogenic activity in visceral adipocytes of male Wistar rats. Acta Physiologica. 2014;211:409–20.

49. Campbell JE, Peckett AJ, D'souza AM, Hawke TJ, Riddell MC. Adipogenic and lipolytic effects of chronic glucocorticoid exposure. American Journal of Physiology-Cell Physiology. 2011;300:C198–209.

50. Peng K, Pan Y, Li J, Khan Z, Fan M, Yin H, et al. 11β-Hydroxysteroid Dehydrogenase Type 1(11β-HSD1) mediates insulin resistance through JNK activation in adipocytes. Sci Rep. 2016;6:37160.

51. Morgan SA, McCabe EL, Gathercole LL, Hassan-Smith ZK, Larner DP, Bujalska IJ, et al. 11β-HSD1 is the major regulator of the tissue-specific

effects of circulating glucocorticoid excess. Proceedings of the National Academy of Sciences. 2014;111.

52. Do TTH, Marie G, Héloïse D, Dorothée G, Marthe M, Bruno F, et al. Glucocorticoid-induced insulin resistance is related to macrophage visceral adipose tissue infiltration. J Steroid Biochem Mol Biol. 2019;185:150–62.

53. Sakoda H, Ogihara T, Anai M, Funaki M, Inukai K, Katagiri H, et al. Dexamethasone-induced insulin resistance in 3T3-L1 adipocytes is due to inhibition of glucose transport rather than insulin signal transduction. Diabetes. 2000;49:1700–8.

54. Park Y-K, Wang L, Giampietro A, Lai B, Lee J-E, Ge K. Distinct Roles of Transcription Factors KLF4, Krox20, and Peroxisome Proliferator-Activated Receptor γ in Adipogenesis. Mol Cell Biol. 2017;37.

55. Park Y-K, Ge K. Glucocorticoid Receptor Accelerates, but Is Dispensable for, Adipogenesis. Mol Cell Biol. 2017;37.

56. Ayala-Sumuano J-T, Velez-delValle C, Beltrán-Langarica A, Marsch-Moreno M, Hernandez-Mosqueira C, Kuri-Harcuch W. Glucocorticoid Paradoxically Recruits Adipose Progenitors and Impairs Lipid Homeostasis and Glucose Transport in Mature Adipocytes. Sci Rep. 2013;3:2573.

57. Bönisch C, Irmler M, Brachthäuser L, Neff F, Bamberger MT, Marschall S, et al. Dexamethasone treatment alters insulin, leptin, and adiponectin levels in male mice as observed in DIO but does not lead to alterations of metabolic phenotypes in the offspring. Mammalian Genome. 2016;27:17–28.

58. de Kloet AD, Herman JP. Fat-brain connections: Adipocyte glucocorticoid control of stress and metabolism. Front Neuroendocrinol. 2018;48:50–7.

59. Jia G, Aroor AR, Sowers JR. The role of mineralocorticoid receptor signaling in the cross-talk between adipose tissue and the vascular wall. Cardiovasc Res. 2017;113:1055–63.

60. Patel R, Magomedova L, Tsai R, Angers S, Orellana A, Cummins CL. Separating the Anti-Inflammatory and Diabetogenic Effects of Glucocorticoids Through LXRβ Antagonism. Endocrinology. 2017;158:1034–47.

61. Besse-Patin A, Jeromson S, Levesque-Damphousse P, Secco B, Laplante M, Estall JL. PGC1A regulates the IRS1:IRS2 ratio during fasting to influence hepatic metabolism downstream of insulin. Proceedings of the National Academy of Sciences. 2019;116:4285–90.

62. Gremlich S, Roduit R, Thorens B. Dexamethasone Induces Posttranslational Degradation of GLUT2 and Inhibition of Insulin Secretion in Isolated Pancreatic β Cells. Journal of Biological Chemistry. 1997;272:3216–22.

63. Ullrich S, Berchtold S, Ranta F, Seebohm G, Henke G, Lupescu A, et al. Serum- and Glucocorticoid-Inducible Kinase 1 (SGK1) Mediates Glucocorticoid-Induced Inhibition of Insulin Secretion. Diabetes. 2005;54:1090–9.

64. Weinstein RS. Glucocorticoid-Induced Osteoporosis and Osteonecrosis. Endocrinol Metab Clin North Am. 2012;41:595–611.

65. Van Staa TP, Leufkens HGM, Abenhaim L, Zhang B, Cooper C. Use of Oral Corticosteroids and Risk of Fractures. Journal of Bone and Mineral Research. 2000;15:993–1000.

66. Robling AG, Bonewald LF. The Osteocyte: New Insights. Annu Rev Physiol. 2020;82:485–506.

67. Dance A. Fun facts about bones: More than just scaffolding. Knowable Magazine. 2022;

68. Shirazi S, Ravindran S, Cooper LF. Topography-mediated immunomodulation in osseointegration; Ally or Enemy. Biomaterials. 2022;291:121903.

69. Raisz LG. Pathogenesis of osteoporosis: concepts, conflicts, and prospects. J Clin Invest. 2005;115:3318–25.

70. Ahmad M, Hachemi Y, Paxian K, Mengele F, Koenen M, Tuckermann J. A Jack of All Trades: Impact of Glucocorticoids on Cellular Cross-Talk in Osteoimmunology. Front Immunol. 2019;10.

71. Chotiyarnwong P, McCloskey E V. Pathogenesis of glucocorticoid-induced osteoporosis and options for treatment. Nat Rev Endocrinol. 2020;16:437–47.

72. Houdek MT, Wyles CC, Packard BD, Terzic A, Behfar A, Sierra RJ. Decreased Osteogenic Activity of Mesenchymal Stem Cells in Patients With Corticosteroid-Induced Osteonecrosis of the Femoral Head. J Arthroplasty. 2016;31:893–8.

73. O'Brien CA, Jia D, Plotkin LI, Bellido T, Powers CC, Stewart SA, et al. Glucocorticoids Act Directly on Osteoblasts and Osteocytes to Induce Their Apoptosis and Reduce Bone Formation and Strength. Endocrinology. 2004;145:1835–41.

74. Rauch A, Seitz S, Baschant U, Schilling AF, Illing A, Stride B, et al. Glucocorticoids Suppress Bone Formation by Attenuating Osteoblast Differentiation via the Monomeric Glucocorticoid Receptor. Cell Metab. 2010;11:517–31.

75. Piemontese M, Xiong J, Fujiwara Y, Thostenson JD, O'Brien CA. Cortical bone loss caused by glucocorticoid excess requires RANKL

production by osteocytes and is associated with reduced OPG expression in mice. American Journal of Physiology-Endocrinology and Metabolism. 2016;311:E587–93.

76. Swanson C, Lorentzon M, Conaway HH, Lerner UH. Glucocorticoid Regulation of Osteoclast Differentiation and Expression of Receptor Activator of Nuclear Factor-κB (NF-κB) Ligand, Osteoprotegerin, and Receptor Activator of NF-κB in Mouse Calvarial Bones. Endocrinology. 2006;147:3613–22.

77. Hofbauer LC, Gori F, Riggs BL, Lacey DL, Dunstan CR, Spelsberg TC, et al. Stimulation of Osteoprotegerin Ligand and Inhibition of Osteoprotegerin Production by Glucocorticoids in Human Osteoblastic Lineage Cells: Potential Paracrine Mechanisms of Glucocorticoid-Induced Osteoporosis1. Endocrinology. 1999;140:4382–9.

78. Jia D, O'Brien CA, Stewart SA, Manolagas SC, Weinstein RS. Glucocorticoids Act Directly on Osteoclasts to Increase Their Life Span and Reduce Bone Density. Endocrinology. 2006;147:5592–9.

79. Hirayama T, Sabokbar A, Athanasou N. Effect of corticosteroids on human osteoclast formation and activity. Journal of Endocrinology. 2002;175:155–63.

80. Weinstein RS, Chen J-R, Powers CC, Stewart SA, Landes RD, Bellido T, et al. Promotion of osteoclast survival and antagonism of bisphosphonate-induced osteoclast apoptosis by glucocorticoids. Journal of Clinical Investigation. 2002;109:1041–8.

81. Kim H-J. Glucocorticoids suppress bone formation via the osteoclast. Journal of Clinical Investigation. 2006;116:2152–60.

82. Hong JM, Teitelbaum SL, Kim T-H, Ross FP, Kim S-Y, Kim H-J. Calpain-6, a target molecule of glucocorticoids, regulates osteoclastic bone

resorption via cytoskeletal organization and microtubule acetylation. Journal of Bone and Mineral Research. 2011;26:657–65.

83. Conaway HH, Henning P, Lie A, Tuckermann J, Lerner UH. Activation of dimeric glucocorticoid receptors in osteoclast progenitors potentiates RANKL induced mature osteoclast bone resorbing activity. Bone. 2016;93:43–54.

84. Sivagurunathan S, Muir MM, Brennan TC, Seale JP, Mason RS. Influence of Glucocorticoids on Human Osteoclast Generation and Activity. Journal of Bone and Mineral Research. 2004;20:390–8.

85. Andersson SGE, Karlberg O, Canbäck B, Kurland CG. On the origin of mitochondria: a genomics perspective. Philos Trans R Soc Lond B Biol Sci. 2003;358:165–77; discussion 177-9.

86. Duchen MR. Mitochondria in health and disease: perspectives on a new mitochondrial biology. Mol Aspects Med. 2004;25:365–451.

87. Indo HP, Yen H-C, Nakanishi I, Matsumoto K, Tamura M, Nagano Y, et al. A mitochondrial superoxide theory for oxidative stress diseases and aging. J Clin Biochem Nutr. 2015;56:1–7.

88. Cadenas E, Davies KJA. Mitochondrial free radical generation, oxidative stress, and aging11This article is dedicated to the memory of our dear friend, colleague, and mentor Lars Ernster (1920–1998), in gratitude for all he gave to us. Free Radic Biol Med. 2000;29:222–30.

89. Ashrafian H, Frenneaux MP, Opie LH. Metabolic Mechanisms in Heart Failure. Circulation. 2007;116:434–48.

90. Nisoli E, Clementi E, Carruba MO, Moncada S. Defective Mitochondrial Biogenesis. Circ Res. 2007;100:795–806.

91. Wiederkehr A, Wollheim CB. Minireview: Implication of Mitochondria in Insulin Secretion and Action. Endocrinology. 2006;147:2643–9.

92. Besseiche A, Riveline J-P, Delavallée L, Foufelle F, Gautier J-F, Blondeau B. Oxidative and energetic stresses mediate beta-cell dysfunction induced by PGC-1α. Diabetes Metab. 2018;44:45–54.

93. Luan G, Li G, Ma X, Jin Y, Hu N, Li J, et al. Dexamethasone-Induced Mitochondrial Dysfunction and Insulin Resistance-Study in 3T3-L1 Adipocytes and Mitochondria Isolated from Mouse Liver. Molecules. 2019;24:1982.

94. Ježková J, Ďurovcová V, Wenchich L, Hansíková H, Zeman J, Hána V, et al. The relationship of mitochondrial dysfunction and the development of insulin resistance in Cushing's syndrome . Diabetes Metab Syndr Obes. 2019;Volume 12:1459–71.

95. Caffarini M, Armeni T, Pellegrino P, Cianfruglia L, Martino M, Offidani A, et al. Cushing Syndrome: The Role of MSCs in Wound Healing, Immunosuppression, Comorbidities, and Antioxidant Imbalance. Front Cell Dev Biol. 2019;7.

96. Friedenstein AJ, Gorskaja JF, Kulagina NN. Fibroblast precursors in normal and irradiated mouse hematopoietic organs. Exp Hematol. 1976;4:267–74.

97. Song M, Zhao D, Wei S, Liu C, Liu Y, Wang B, et al. The effect of electromagnetic fields on the proliferation and the osteogenic or adipogenic differentiation of mesenchymal stem cells modulated by dexamethasone. Bioelectromagnetics. 2014;35:479–90.

98. Li H, Qian W, Weng X, Wu Z, Li H, Zhuang Q, et al. Glucocorticoid Receptor and Sequential P53 Activation by Dexamethasone Mediates Apoptosis and Cell Cycle Arrest of Osteoblastic MC3T3-E1 Cells. PLoS One. 2012;7:e37030.

99. Pereira RC, Delany AM, Canalis E. Effects of cortisol and bone morphogenetic protein-2 on stromal cell differentiation: correlation with CCAAT-enhancer binding protein expression. Bone. 2002;30:685–91.

100. Cárcamo-Orive I, Gaztelumendi A, Delgado J, Tejados N, Dorronsoro A, Fernández-Rueda J, et al. Regulation of human bone marrow stromal cell proliferation and differentiation capacity by glucocorticoid receptor and AP-1 crosstalk. Journal of Bone and Mineral Research. 2010;25:2115–25.

101. Orciani M, Gorbi S, Benedetti M, Di Benedetto G, Mattioli-Belmonte M, Regoli F, et al. Oxidative stress defense in human-skin-derived mesenchymal stem cells versus human keratinocytes: Different mechanisms of protection and cell selection. Free Radic Biol Med. 2010;49:830–8.

102. Orciani M, Campanati A, Salvolini E, Lucarini G, Di Benedetto G, Offidani A, et al. The mesenchymal stem cell profile in psoriasis. British Journal of Dermatology. 2011;165:585–92.

103. Zhao L, Hantash BM. Isolation and Cultivation of Human Scalp Interfollicular Epidermal Stem Cells. 2013. p. 11–9.

104. Debono M, Ghobadi C, Rostami-Hodjegan A, Huatan H, Campbell MJ, Newell-Price J, et al. Modified-Release Hydrocortisone to Provide Circadian Cortisol Profiles. J Clin Endocrinol Metab. 2009;94:1548–54.

105. Yaradanakul A, Feng S, Shen C, Lariccia V, Lin M, Yang J, et al. Dual control of cardiac Na^{+}–Ca^{2+} exchange by PIP_2: electrophysiological analysis of direct and indirect mechanisms. J Physiol. 2007;582:991–1010.

106. Bonifazi M, Di Vincenzo M, Caffarini M, Mei F, Salati M, Zuccatosta L, et al. How the Pathological Microenvironment Affects the Behavior of Mesenchymal Stem Cells in the Idiopathic Pulmonary Fibrosis. Int J Mol Sci. 2020;21:8140.

107. Halleen JM, Tiitinen SL, Ylipahkala H, Fagerlund KM, Väänänen HK. Tartrate-resistant acid phosphatase 5b (TRACP 5b) as a marker of bone resorption. Clin Lab. 2006;52:499–509.

108. Halleen JM, Alatalo SL, Suominen H, Cheng S, Janckila AJ, Väänänen HK. Tartrate-Resistant Acid Phosphatase 5b: A Novel Serum Marker of Bone Resorption. Journal of Bone and Mineral Research. 2000;15:1337–45.

109. Marchisio PC, Cirillo D, Naldini L, Primavera M V, Teti A, Zambonin-Zallone A. Cell-substratum interaction of cultured avian osteoclasts is mediated by specific adhesion structures. J Cell Biol. 1984;99:1696–705.

110. Sharma U, Pal D, Prasad R. Alkaline Phosphatase: An Overview. Indian Journal of Clinical Biochemistry. 2014;29:269–78.

111. Amarasekara DS, Kim S, Rho J. Regulation of Osteoblast Differentiation by Cytokine Networks. Int J Mol Sci. 2021;22:2851.

112. Chaudhry A, Shi R, Luciani DS. A pipeline for multidimensional confocal analysis of mitochondrial morphology, function, and dynamics in pancreatic β-cells. American Journal of Physiology-Endocrinology and Metabolism. 2020;318:E87–101.

113. Morciano G, Sarti AC, Marchi S, Missiroli S, Falzoni S, Raffaghello L, et al. Use of luciferase probes to measure ATP in living cells and animals. Nat Protoc. 2017;12:1542–62.

114. Ghasemi A, Zahediasl S. Normality Tests for Statistical Analysis: A Guide for Non-Statisticians. Int J Endocrinol Metab. 2012;10:486–9.

115. Feldman BJ. Glucocorticoids Influence on Mesenchymal Stem Cells and Implications for Metabolic Disease. Pediatr Res. 2009;65:249–51.

116. Deshmukh AS. Insulin-stimulated glucose uptake in healthy and insulin-resistant skeletal muscle. Horm Mol Biol Clin Investig. 2016;26:13–24.

117. Honka M-J, Latva-Rasku A, Bucci M, Virtanen KA, Hannukainen JC, Kalliokoski KK, et al. Insulin-stimulated glucose uptake in skeletal muscle, adipose tissue and liver: a positron emission tomography study. Eur J Endocrinol. 2018;178:523–31.

118. Satoh T. Molecular Mechanisms for the Regulation of Insulin-Stimulated Glucose Uptake by Small Guanosine Triphosphatases in Skeletal Muscle and Adipocytes. Int J Mol Sci. 2014;15:18677–92.

119. Bogan JS. Regulation of Glucose Transporter Translocation in Health and Diabetes. Annu Rev Biochem. 2012;81:507–32.

120. Kandror K V., Pilch PF. The Sugar Is sIRVed: Sorting Glut4 and Its Fellow Travelers. Traffic. 2011;12:665–71.

121. Tonack S, Fischer B, Navarrete Santos A. Expression of the insulin-responsive glucose transporter isoform 4 in blastocysts of C57/BL6 mice. Anat Embryol (Berl). 2004;208.

122. Plat L, Leproult R, L'Hermite-Baleriaux M, Fery F, Mockel J, Polonsky KS, et al. Metabolic Effects of Short-Term Elevations of Plasma Cortisol Are More Pronounced in the Evening Than in the Morning [1]. J Clin Endocrinol Metab. 1999;84:3082–92.

123. Beaupere C, Liboz A, Fève B, Blondeau B, Guillemain G. Molecular Mechanisms of Glucocorticoid-Induced Insulin Resistance. Int J Mol Sci. 2021;22:623.

124. Ayala-Sumuano J-T, Velez-delValle C, Beltrán-Langarica A, Marsch-Moreno M, Hernandez-Mosqueira C, Kuri-Harcuch W. Glucocorticoid Paradoxically Recruits Adipose Progenitors and Impairs Lipid Homeostasis and Glucose Transport in Mature Adipocytes. Sci Rep. 2013;3:2573.

125. Weinstein SP, Paquin T, Pritsker A, Haber RS. Glucocorticoid-Induced Insulin Resistance: Dexamethasone Inhibits the Activation of Glucose

Transport in Rat Skeletal Muscle by Both Insulin- and Non-Insulin-Related Stimuli. Diabetes. 1995;44:441–5.

126. Gathercole LL, Bujalska IJ, Stewart PM, Tomlinson JW. Glucocorticoid Modulation of Insulin Signaling in Human Subcutaneous Adipose Tissue. J Clin Endocrinol Metab. 2007;92:4332–9.

127. Yaradanakul A, Feng S, Shen C, Lariccia V, Lin M, Yang J, et al. Dual control of cardiac Na^{+}–Ca^{2+} exchange by PIP_2: electrophysiological analysis of direct and indirect mechanisms. J Physiol. 2007;582:991–1010.

128. Weinstein SP, Paquin T, Pritsker A, Haber RS. Glucocorticoid-Induced Insulin Resistance: Dexamethasone Inhibits the Activation of Glucose Transport in Rat Skeletal Muscle by Both Insulin- and Non-Insulin-Related Stimuli. Diabetes. 1995;44:441–5.

129. Ertunc ME, Sikkeland J, Fenaroli F, Griffiths G, Daniels MP, Cao H, et al. Secretion of fatty acid binding protein aP2 from adipocytes through a nonclassical pathway in response to adipocyte lipase activity. J Lipid Res. 2015;56:423–34.

130. Boden G, Chen X, Rosner J, Barton M. Effects of a 48-h Fat Infusion on Insulin Secretion and Glucose Utilization. Diabetes. 1995;44:1239–42.

131. Geer EB, Islam J, Buettner C. Mechanisms of Glucocorticoid-Induced Insulin Resistance. Endocrinol Metab Clin North Am. 2014;43:75–102.

132. Yu C, Chen Y, Cline GW, Zhang D, Zong H, Wang Y, et al. Mechanism by Which Fatty Acids Inhibit Insulin Activation of Insulin Receptor Substrate-1 (IRS-1)-associated Phosphatidylinositol 3-Kinase Activity in Muscle. Journal of Biological Chemistry. 2002;277:50230–6.

133. Macfarlane DP, Forbes S, Walker BR. Glucocorticoids and fatty acid metabolism in humans: fuelling fat redistribution in the metabolic syndrome. Journal of Endocrinology. 2008;197:189–204.

134. Jocken JWE, Langin D, Smit E, Saris WHM, Valle C, Hul GB, et al. Adipose Triglyceride Lipase and Hormone-Sensitive Lipase Protein Expression Is Decreased in the Obese Insulin-Resistant State. J Clin Endocrinol Metab. 2007;92:2292–9.

135. Mirza S, Hossain M, Mathews C, Martinez P, Pino P, Gay JL, et al. Type 2-diabetes is associated with elevated levels of TNF-alpha, IL-6 and adiponectin and low levels of leptin in a population of Mexican Americans: A cross-sectional study. Cytokine. 2012;57:136–42.

136. Bashir H, Ahmad Bhat S, Majid S, Hamid R, Koul RK, Rehman MU, et al. Role of inflammatory mediators (TNF-α, IL-6, CRP), biochemical and hematological parameters in type 2 diabetes mellitus patients of Kashmir, India. Med J Islam Repub Iran. 2020;34:5.

137. Vestergaard P, Lindholm J, Jorgensen J, Hagen C, Hoeck H, Laurberg P, et al. Increased risk of osteoporotic fractures in patients with Cushing's syndrome. Eur J Endocrinol. 2002;51–6.

138. Manelli F, Giustina A. Glucocorticoid-induced Osteoporosis. Trends in Endocrinology & Metabolism. 2000;11:79–85.

139. Sheu T-J, Schwarz EM, Martinez DA, O'Keefe RJ, Rosier RN, Zuscik MJ, et al. A Phage Display Technique Identifies a Novel Regulator of Cell Differentiation. Journal of Biological Chemistry. 2003;278:438–43.

140. Marchisio PC, Cirillo D, Naldini L, Primavera M V, Teti A, Zambonin-Zallone A. Cell-substratum interaction of cultured avian osteoclasts is mediated by specific adhesion structures. J Cell Biol. 1984;99:1696–705.

141. Sojan JM, Licini C, Marcheggiani F, Carnevali O, Tiano L, Mattioli-Belmonte M, et al. Bacillus subtilis Modulated the Expression of Osteogenic Markers in a Human Osteoblast Cell Line. Cells. 2023;12:364.

142. Ohlsson C, Nilsson KH, Henning P, Wu J, Gustafsson KL, Poutanen M, et al. WNT16 overexpression partly protects against glucocorticoid-induced bone loss. American Journal of Physiology-Endocrinology and Metabolism. 2018;314:E597–604.

143. Hildebrandt S, Baschant U, Thiele S, Tuckermann J, Hofbauer LC, Rauner M. Glucocorticoids suppress Wnt16 expression in osteoblasts in vitro and in vivo. Sci Rep. 2018;8:8711.

144. Delany AM, Jeffrey JJ, Rydziel S, Canalis E. Cortisol Increases Interstitial Collagenase Expression in Osteoblasts by Post-transcriptional Mechanisms. Journal of Biological Chemistry. 1995;270:26607–12.

145. Piemontese M, Xiong J, Fujiwara Y, Thostenson JD, O'Brien CA. Cortical bone loss caused by glucocorticoid excess requires RANKL production by osteocytes and is associated with reduced OPG expression in mice. American Journal of Physiology-Endocrinology and Metabolism. 2016;311:E587–93.

146. Hofbauer LC, Gori F, Riggs BL, Lacey DL, Dunstan CR, Spelsberg TC, et al. Stimulation of Osteoprotegerin Ligand and Inhibition of Osteoprotegerin Production by Glucocorticoids in Human Osteoblastic Lineage Cells: Potential Paracrine Mechanisms of Glucocorticoid-Induced Osteoporosis1. Endocrinology. 1999;140:4382–9.

147. Swanson C, Lorentzon M, Conaway HH, Lerner UH. Glucocorticoid Regulation of Osteoclast Differentiation and Expression of Receptor Activator of Nuclear Factor-κB (NF-κB) Ligand, Osteoprotegerin, and Receptor Activator of NF-κB in Mouse Calvarial Bones. Endocrinology. 2006;147:3613–22.

148. Jia D, O'Brien CA, Stewart SA, Manolagas SC, Weinstein RS. Glucocorticoids Act Directly on Osteoclasts to Increase Their Life Span and Reduce Bone Density. Endocrinology. 2006;147:5592–9.

149. Teitelbaum SL. Glucocorticoids and the osteoclast. Clin Exp Rheumatol. 2015;33:S37-9.

150. Kim H-J. Glucocorticoids suppress bone formation via the osteoclast. Journal of Clinical Investigation. 2006;116:2152–60.

151. Pivonello R, Faggiano A, Lombardi G, Colao A. The Metabolic Syndrome and Cardiovascular Risk in Cushing's Syndrome. Endocrinol Metab Clin North Am. 2005;34:327–39.

152. Krsek M, Silha J V., Jezková J, Hána V, Marek J, Weiss V, et al. Adipokine levels in Cushing's syndrome; elevated resistin levels in female patients with Cushing's syndrome. Clin Endocrinol (Oxf). 2004;60:350–7.

153. Van Raalte DH, Ouwens DM, Diamant M. Novel insights into glucocorticoid-mediated diabetogenic effects: towards expansion of therapeutic options? Eur J Clin Invest. 2009;39:81–93.

154. Fleseriu M, Biller BMK, Findling JW, Molitch ME, Schteingart DE, Gross C, et al. Mifepristone, a Glucocorticoid Receptor Antagonist, Produces Clinical and Metabolic Benefits in Patients with Cushing's Syndrome. J Clin Endocrinol Metab. 2012;97:2039–49.

155. Duchen MR. Mitochondria in health and disease: perspectives on a new mitochondrial biology. Mol Aspects Med. 2004;25:365–451.

156. Weber K, Brück P, Mikes Z, Küpper J-H, Klingenspor M, Wiesner RJ. Glucocorticoid Hormone Stimulates Mitochondrial Biogenesis Specifically in Skeletal Muscle. Endocrinology. 2002;143:177–84.

157. Du J, Wang Y, Hunter R, Wei Y, Blumenthal R, Falke C, et al. Dynamic regulation of mitochondrial function by glucocorticoids. Proceedings of the National Academy of Sciences. 2009;106:3543–8.

158. Du J, McEwen B, Manji HK. Glucocorticoid receptors modulate mitochondrial function. Commun Integr Biol. 2009;2:350–2.

159. Eisner V, Picard M, Hajnóczky G. Mitochondrial dynamics in adaptive and maladaptive cellular stress responses. Nat Cell Biol. 2018;20:755–65.

160. Suliman HB, Piantadosi CA. Mitochondrial Quality Control as a Therapeutic Target. Pharmacol Rev. 2016;68:20–48.

161. Yoon Y. Morphological control of mitochondrial bioenergetics. Frontiers in Bioscience. 2015;20:4306.

162. Yoon Y, Galloway CA, Jhun BS, Yu T. Mitochondrial Dynamics in Diabetes. Antioxid Redox Signal. 2011;14:439–57.

163. Lee H, Smith SB, Yoon Y. The short variant of the mitochondrial dynamin OPA1 maintains mitochondrial energetics and cristae structure. Journal of Biological Chemistry. 2017;292:7115–30.

164. Sessions DT, Kim K-B, Kashatus JA, Churchill N, Park K-S, Mayo MW, et al. Opa1 and Drp1 reciprocally regulate cristae morphology, ETC function, and NAD+ regeneration in KRas-mutant lung adenocarcinoma. Cell Rep. 2022;41:111818.

165. Frezza C, Cipolat S, Martins de Brito O, Micaroni M, Beznoussenko G V., Rudka T, et al. OPA1 Controls Apoptotic Cristae Remodeling Independently from Mitochondrial Fusion. Cell. 2006;126:177–89.

166. Furukawa S, Fujita T, Shimabukuro M, Iwaki M, Yamada Y, Nakajima Y, et al. Increased oxidative stress in obesity and its impact on metabolic syndrome. Journal of Clinical Investigation. 2004;114:1752–61.

167. Kowaltowski AJ, Vercesi AE. Mitochondrial damage induced by conditions of oxidative stress. Free Radic Biol Med. 1999;26:463–71.

168. Zorov DB, Juhaszova M, Sollott SJ. Mitochondrial Reactive Oxygen Species (ROS) and ROS-Induced ROS Release. Physiol Rev. 2014;94:909–50.

169. Hu J, Zhang Y, Jiang X, Zhang H, Gao Z, Li Y, et al. ROS-mediated activation and mitochondrial translocation of CaMKII contributes to Drp1-dependent mitochondrial fission and apoptosis in triple-negative breast cancer cells by isorhamnetin and chloroquine. Journal of Experimental & Clinical Cancer Research. 2019;38:225.

170. James AM, Collins Y, Logan A, Murphy MP. Mitochondrial oxidative stress and the metabolic syndrome. Trends in Endocrinology & Metabolism. 2012;23:429–34.

INDEX OF FIGURES

osteoblastic lineage, proliferation and maturation of preosteoblasts, matrix deposition (osteoid) by osteoblasts, and bone matrix mineralization with calcium phosphate deposition and formation of hydroxyapatite crystals (new bone). Osteoblastogenesis is regulated by a cascade activation of transcriptional factors such as *RUNX2* and Bone morphogenetic protein (*BMP*) that induce the expression of Alkaline phosphatase (*ALPL*), Collagen alpha-1 and -2 (I) chain (*COL1A1* and *COL1A2*), specific markers of osteoblasts differentiation during early stages, and followed by Collagen alpha-1(III) chain (*COL3A1*), Sphingosine-1-phosphate phosphatase 1 (*SPP1*), Osteonectin (*ON* also known as *SPARC*), Osteocalcin (*BGLAP*) and Bone sialoprotein 2 (*IBSP*) in tardive (late) stages of differentiation.

Figure 7. MSCs multipotency. (a) Representative images of MSCs isolated from abdominal skin of healthy subject (C-MSCs) enrolled in TASK1 and induced to differentiate toward osteogenic lineage as assessed by ALP and Alizarin Red-S staining (scale bar 100μm); chondrogenic lineage as indicated by Safranin-O staining (scale bar 100μm) and adipocyte lineage as confirmed by Oil red staining (scale bar 100μm). **(b)** Representative images of MSCs isolated from back skin of C-MSCs and Cushing patients (ENDO-, EXO-, EXO SS-MSCs) differentiated toward adipocyte lineage as demonstrated by Oil red staining (scale bar 100μm) and chondrogenic lineage as indicated by Safranin-O staining (scale bar 100μm).

Figure 8. Cells viability at T3, T6 and T7 sampling times. Bars represent XTT absorbance of experimental groups at the end of each day of treatments (T3, T6 and T7). Data are expressed as mean ± SD of the absorbance read for MSCs derived from the abdominal skin of each single healthy subject over three independent experiments. One-way ANOVA; $^{**}p < 0.01$.

Figure 9. Responsiveness of MSCs to insulin. The bars show the glucose uptake expressed in pM at T1, T2, T3, T4, T5 and T6 in insulin-stimulated or non-stimulated MSCs. Data are expressed as mean ± SD of the analysis

for MSCs derived from the abdominal skin of each single healthy subject over three independent experiments. Unpaired t-Student's test; *p < 0.05, **p < 0.01.

Figure 10. GLUT-4 translocation. Representative confocal images of GLUT-4 in MSCs derived from the abdominal skin of seven healthy subjects and stimulated **(b, d)** or not **(a, c)** with insulin and constantly exposed to high concentrations of GCs **(c, d)**. The graphs **(e–h)** show the fluorescence ratio between the edge and the centre of the cell; yellow arrows indicate the portion of cell subjected to analysis.

Figure 11. Glucose uptake in MSCs undergoing a LDE or a HCE to GCs. The bars represent the glucose uptake expressed in pM at T1 (9:50 a.m. first day, **a**), T2 (1:50 p.m. first day, **b**), T3 (5:50 p.m. first day, **c**), T4 (9:50 a.m. second day, **d**), T5 (1:50 p.m. second day, **e**), T6 (5:50 p.m. second day, **f**) and T7(1:50 p.m. third day, **g**) in MSCs isolated from abdominal skin of healthy subjects undergoing a LDE or a HCE to GCs and stimulated or not with insulin. Data are expressed as mean ± SD of the readings for MSCs derived from each single patient over three independent experiments. One-way ANOVA; *p < 0.05,**p < 0,01,***p < 0,001.

Figure 12. Gene expression in MSCs undergoing a LDE or a HCE to GCs. The bars display the expression of genes referred specifically to the development of IR: *LIPE* **(a)**, *ATGL* **(b)**, *IL6* **(c)** and *TNFA* **(d)** at T2 and T7 sampling times in MSCs isolated from abdominal skin of healthy subjects after treatments. Data are expressed as mean ± SD (over three independent experiments) of the X-FOLD ($2^{-\Delta\Delta Ct}$ method) of HCE+INS+GLU compared to LDE+INS+GLU arbitrarily expressed as 1, where ΔCt=Ct (gene of interest)—Ct (control gene) and Δ (ΔCt)=ΔCt (HCE+INS+GLU)—ΔCt (LDE+INS+GLU). Unpaired t-Student's test; *p < 0.05,**p < 0.01,***p < 0.001;****p < 0.0001.

Figure 13. PBMCs differentiation capability into osteoclasts. (a) TRAcP (purple staining), Cathepsin K (DAB positivity, brown staining) and actin ring formation (indicated with yellow arrows) representative images of C-PBMCs, ENDO- PBMCs, EXO- PBMCs and EXO SS- PBMCs after 14 days of differentiations into osteoclasts (scale bar 50μm). Bars indicate the percentage of cells: with more than 3 nuclei **(b)**, positive to TRAcP **(c)**, positive to Cathepsin K **(d)** and positive to actin ring **(e)**. Data are expressed as mean ± SD of each field percentage. One-way ANOVA *p < 0.05,**p < 0.01,***p < 0.001;****p < 0.0001.

Figure 14. Osteoclasts activity. PBMCs differentiated into osteoclasts have been cultured on bone slices for 96 hours. **(a)** Coomassie Brillant Blue staining of bone slices. Yellow arrows point resorption pits (scale bar 100μm). **(b)** Bars indicate the percentage of bone resorption area. Data are expressed as mean ± SD of each field percentage **(c)** The graph shows the CTX-I medium concentration expressed in nM. Data are expressed as mean ± SD of the analysis for CTX-I of medium collected from three independent experiments for each sample. One-way ANOVA *p < 0.05,**p < 0.01,***p < 0.001;****p < 0.0001.

Figure 15. Ability of MSCs to differentiate into osteoblasts. (a) Representative images of ALP staining (scale bar 100μm), ALP immune-fluorescence (IF, white arrows indicate ALP vesicles, scale bar 10μm), and Alizarin Red-S (scale bar 100μm) after 7 (T7) and 21 (T21) days of differentiation of MSCs into osteoblasts. Graphs indicate the percentage of area of positivity to ALP staining **(b)**, ALP immuno-fluorescence **(c)** and Alizarin Red-S quantification expressed in nM **(d)**. Data are expressed as mean ± SD of each field percentage for ALP and as mean ± SD of quantification analysis for Alizarin Red S. One-way ANOVA *p < 0.05,**p < 0.01,***p < 0.001;****p < 0.0001.

Figure 16. Collagen deposition. (a) Representative images of Sirius Red staining before (T0) and after 7 (T7) and 21 (T21) days of differentiation of MSCs into osteoblasts (scale bar 50μm). **(b)** Sirius Red quantification. Data are expressed as mean ± SD of the OD detected in three independent experiments. Two-way ANOVA *p < 0.05,**p < 0.01,***p < 0.001;****p < 0.0001.

Figure 17. Osteoblastogenesis gene expression. The bars display the expression of genes referred specifically to the early (*RUNX2*, **(a)**, *ALPL* **(b)**, *COL1A1* **(e)**) and tardive (*SPARC* **(c)**, *BGLAP* **(d)**, *COL3A1* **(f)**) steps of osteoblastogenesis, at the beginning (T0) and after 7 (T7) and 21 (T21) days of differentiation. Data are expressed as mean ± SD (over three independent experiments) of the X-FOLD ($2^{-\Delta\Delta Ct}$ method) of C-MSCs, ENDO-MSCs, EXO-MSCs and EXO SS-MSCs at different time point compared to C-MSCs at T0 arbitrarily expressed as 1. Two-way ANOVA; *p < 0.05,**p < 0.01,***p < 0.001;****p < 0.0001.

Figure 18. Osteoblastogenesis protein levels. **(a)** Representative images of WB analysis of RUNX2, ALP, COL1A1, RANK-L, OPG and GAPDH of C-MSCs, ENDO-MSCs, EXO-MSCs and EXO SS-MSCs at the beginning (T0) and after 7 (T7) and 21 (T21) days of differentiation. The graphs below represent the densiometric analysis referred to GAPDH of each protein **(b-e)**. Two-way ANOVA; *p < 0.05,**p < 0.01,***p < 0.001;****p < 0.0001.

Figure 19. Mitochondrial morphology. (a) Representative confocal images of mitochondrial structure of C-MSCs, ENDO-MSCs, EXO-MSCs and EXO SS-MSCs (scale bar 50μm). In the upper inset an enlargement of a mitochondria portion. **(b, c)** Analysis of mitochondria morphology (Aspect Ratio and Form Factor) and mitochondrial network **(d, e)** (Branches and Branch Junctions) of C-MSCs ENDO-MSCs, EXO-MSCs and EXO SS-MSCs. Data are expressed as mean ± SD of the analysis of 30 cells for each

experimental group. One-way ANOVA; *p < 0.05, ***p < 0,001, ****p<0,0001.

Figure 20. Cellular and mitochondrial ROS production. (a) Cellular ROS production of C-MSCs, ENDO-MSCs, EXO-MSCs and EXO SS-MSCs detected by CM-H2DCFDA assay. Bars indicate the fluorescence intensity ratio between CM-H2DCFDA (485-535nm) and DAPI (340-465nm). **(b)** Mitochondrial ROS production of C-MSCs, ENDO-MSCs, EXO-MSCs and EXO SS-MSCs detected by MitoSOX Red assay. Bars point the fluorescence intensity ratio between MitoSOX Red (535-590nm) and DAPI (340-465nm). Data are expressed as the mean ± SD of three independent experiments. One-way ANOVA; *p < 0.05, ***p < 0,001, ****p<0,0001.

Figure 21. Mitochondrial membrane potential. ΔΨ of C-MSCs, ENDO-MSCs, EXO-MSCs and EXO SS-MSCs detected by TMRM assay. Bars report the fluorescence intensity ratio between TMRM (535-590nm) and DAPI (340-465nm). Data are expressed as the mean ± SD of three independent experiments. One-way ANOVA; *p < 0.05, ***p < 0,001, ****p<0,0001.

Figure 22. Mitochondrial ATP production. (a) ATP kinetic in mitochondrial compartments. The graph shows the luminescence background levels (from 0 to 60 sec), basal ATP levels (from 60 to 210 sec) and Bradykinin stimulated ATP production (from 210 to 300 sec) in living cells by using luciferin. **(b)** Mitochondrial ATP production. The bars indicate the fold change between the average of Bradykinin stimulated ATP production luminescence and basal ATP levels luminescence. Data are expressed as the mean ± SD of three independent experiments. One-way ANOVA; **p < 0,01.